ABSTRACT

Title of Dissertation:	FIRST PRINCIPLES COMPUTATIONAL STUDY OF FAST IONIC CONDUCTORS
	Xingfeng He, Doctor of Philosophy, 2018
Dissertation directed by:	Assistant Professor Yifei Mo, Department of Materials Science and Engineering

Fast ionic conductors have great potential to enable novel technologies in energy storage and conversion. However, it is not yet understood why only a few materials can deliver exceptionally higher ionic conductivity than typical solids or how on can design fast ion conductors following simple principles. In this dissertation, I applied first principles computational method to understanding the fast ionic diffusion within fast ionic conductors and I demonstrated a conceptually simple framework for guiding the design of super-ionic conductor materials.

I studied $Na_{0.5}Bi_{0.5}TiO_3$ (NBT) as the model material for oxygen ionic conductor. The structure-property relationship of the NBT materials is established. Based on the newly gained materials understanding, our first principles computation predicted that Na and K were promising dopants to increase oxygen ionic conductivity. The newly designed NBT materials with A-site Na and K substituted A

sites exhibited a many-fold increase in the ionic conductivity at 900K comparing to that in the experimental compound.

We demonstrated that the concerted migration mechanism with low energy barrier is the universal mechanism of fast ionic diffusion in a broad range of ionic conducting materials. Our theory provides a conceptually simple framework for guiding the design of super-ionic conductor materials, that is, inserting mobile ions into high-energy sites to activate concerted ion conduction with lower migration barriers. We demonstrated this strategy by designing a number of novel fast Li-ion conducting materials to activate concerted migration with reduced diffusion barrier.

We identified the common features of crystal structural framework for lithium SICs. Based on the determined attributes, we performed a high-throughput screening of all lithium-containing oxide and sulfide compounds. The screening revealed several crystal structures that are potential to be fast ion conductors. Through aliovalent doping, we modified the Li content of these structures which resulting in different Li sublattice within the structure and we found a number of lithium super-ionic conductors that are predicted to have Li+ conductivities greater than 0.1 mS/cm at 300K.

FIRST PRINCIPLES COMPUTATIONAL STUDY OF FAST IONIC CONDUCTORS

by

Xingfeng He

Dissertation submitted to the Faculty of the Graduate School of the
University of Maryland, College Park, in partial fulfillment
of the requirements for the degree of
Doctoral of Philosophy
2018

Advisory Committee:
- Professor Yifei Mo, Chair, Advisor
- Professor Eric D. Wachasman
- Professor Mark D. Fuge
- Professor Liangbing Hu
- Professor Chunsheng Wang, Dean’s representative

Dedication

To Pingyu

Acknowledgements

First and foremost, I would like to thank my thesis advisor, Professor Yifei Mo, for his great guidance and comprehensive support through my graduate study. I am lucky and honored to be his first Ph.D. student. In the last five years, the most important thing I learned from Prof. Mo is to do insightful research we and others believe and care. Beyond his rigorous research style, I was also deeply impressed by his insightful vision and dedicated support on students. I appreciate the stress, the laugh, the arguments, the excitement and the unforgettable time I experienced. These shaped me and will continue to be a part of me. Thank you, Prof. Mo.

I would like to thank my committee, Prof. Eric Wachsman, Prof. Chunsheng Wang, Prof. Mark Fuge and Prof. Liangbing Hu. I learned a lot from interactions with them. I am honored to have them as my committee.

I also thank my collaborators, Prof. Hailong Chen from Georgia Institute of Technology, Dr. Fudong Han from Prof. Wang's group, Dr. Xiaogang Han and Dr. Kun Fu from Prof. Hu's group, Dr. Yunhui Gong from Prof. Wachsman's group.

I would like to thank my labmates: Dr. Yizhou Zhu, Qiang Bai, Alex Epstein, Addie Nolan, Yunsheng Liu and Shafiqul Islam. I appreciate your help on my research.

I would like to than my undergraduate advisors, Prof. Jiaping Wang, Prof. Yang Wu and Prof. Shoushan Fan. Thank you for introducing me to the world of materials science.

I also thank my roommates over the last five years: Xing Niu, Yingqi Zhang, Dr. Jinfeng Rao, Dr. Ang Gao, Dr. Zhihao Li, Hong Zhou, Nairui Zhou. We shared a lot of happy memories at Westchester, Lakeside North and University Square.

I also thank my undergraduate friends Dr. Bin Dai, Dr. Wenhan Zhang, Dr. Panyu Hou, Dr. Yiquan Zou and Dr. Haoxiang Yang. Our daily chat on Wechat is one of the most interesting things in my PhD study.

I also thank my friends at UMD, Pingshan Luan, Dr. Jiayu Wan, Dr. Chen Gong, Jing Nie, Sheng Yang, Feng Gu, Lingxi Kong, Dr. Zhi Yang, Dr. Jiaqi Dai, Zhengyang Wang, Yang Zhang and Xiaoxiao Ge. I also thank my friends I met in the DC area, Dr. Jin Yan, Dr. Shawn Zeng, Dr. Tao Gao, Dr. Hong Lin, Dr. Fei Xin, Dr. Kun Gu, Weixun Qu, Zezhou Cai, Rui He, Yuanxin Liao, Yunru Feng and Huiling Li. You made my life at Maryland more colorful.

I would like to thank my friends at Kedao, Yanyang Wu, Dr. Guang Chen, Dr. Xiang Li, Jiachen Zhang. Our work on environmental protection is a great memory.

I would like to thank my colleagues and friends when I did intern at California. Dr. Yifan Zhang, Dr. Yun Liu, Dr. Shunan Zhang, Yu Kang, Dr. Paul Drzaic, Dr. TK Koh, Siqi Ma, Sheng Wang, Yitian Bie and Dr. Long Xin.

I would also like to thank my and my wife’s friends at UVA, Dr. Xiang Wan, Dr. Fang Guo, Dr. Zhe Zhu, Dr. Jiekun Yang, Nan Zhi, Zhiqi Wang and Yu Wang. Thank you for your help to my wife and me.

Finally, I would like to thank my family, my grandparents, my parents, my parents-in-law, my brother, my brother-in-law, my sisters-in-law and my two super lovely nieces, for their unconditional love in my entire life. My deepest gratitude goes to my wife. This book is dedicated to you.

Table of Contents

List of Abbreviations

Super-ionic conductors (SICs)

$Na_{0.5}Bi_{0.5}TiO_3$ (NBT)

$Li_{1.33}Ti_{1.67}Al_{0.33}(PO_4)_3$ (LATP)

$Li_{10}GeP_2S_{12}$ (LGPS)

$Li_7La_3Zr_2O_{12}$ (LLZO)

Sodium (Na) Super Ionic CONductor (NASICON)

Lithium Super Ionic CONductor (LISICON)

Total Mean Squared Displacement (*TMSD*)

Relative Standard Deviation (RSD)

Inorganic Crystal Structure Database (ICSD)

Solid oxide fuel cell (SOFC)

All Solid-state Battery (ASB)

Room Temperature (RT)

body-centered cubic (bcc)

Density Functional Theory (DFT)

Vienna *Ab initio* Simulation Package (VASP)

Perdew-Burke-Ernzerhof (PBE)

Generalized-Gradient Approximation (GGA)

Nudged Elastic Band (NEB)

Ab initio molecular dynamics (AIMD)

Chapter 1: Introduction[1]

1.1. Fast ionic conductors

Fast ionic conductors are solid-state compounds with highly mobile ions, which exhibit exceptionally high values of ionic conductivity. Their ionic conductivities are several orders of magnitude higher than typical solids and are comparable to their ionic conductivities within liquid or molten state. The fast ionic diffusion within solid materials is first reported by Faraday in the materials of β-PbF_2 in the first half of the 19th century.[1] In the following ~200 years, there has been significant research efforts into discovering new fast ionic conductors and understanding why these compounds can achieve several orders of magnitude faster ionic diffusion than other solid materials.[2,3] However, given the complexity of the fast ionic conductor systems, a general fundamental understanding is still lacking.

Besides the scientific interest, fast ionic conductors are indispensable components in electrochemical energy storage and conversion devices such as batteries, fuel cells, and electrochemical membranes[4-9], which are critical in the societal shift to renewable energy. Thanks to recently found new fast ionic conductors which have great potential applications in energy field and the advanced simulation

---

[1] Some text of introduction is adapted from papers:
X. He and Y. Mo. "Accelerated materials design of $Na_{0.5}Bi_{0.5}TiO_3$ oxygen ionic conductors based on first principles calculations." *Physical Chemistry Chemical Physics*, (2015), 17: 18035–18044.
X. He, Y. Zhu and Y. Mo. "Origin of Fast Ion Diffusion in Super-Ionic Conductors." *Nature Communications*, (2017), 8: 15893

techniques enabled by the availability of high performance computers, there has been some significant progress in the study of ionic conductors. In this thesis, we studied two types of fast ionic conductors: oxygen ionic conductors and lithium ionic conductors.

1.1.1. Oxygen ionic conductors

Fast oxygen ionic conductor materials have important technological applications in electrochemical devices such as solid oxide fuel cells (SOFCs), oxygen separation membranes and sensors. For example, increasing the oxygen ionic conductivity is critical for increasing the power density and lowering the operational temperature of SOFCs.[10] Over the past decades, significant research efforts have been dedicated to the development of fast oxygen ion conductor materials.[11]

Recently, sodium bismuth titanate, $Na_{0.5}Bi_{0.5}TiO_3$ (NBT), a known piezoelectric material, was reported as a new family of oxygen ionic conductor by Li *et al.*[12] In the prior experimental study[12], the NBT material with Mg doping, $Na_{0.5}Bi_{0.49}Ti_{0.98}Mg_{0.02}O_{2.965}$, has achieved an oxygen conductivity of 8 mS/cm at 600 °C,[12] which is comparable to other well-known oxygen ion conductor materials, such as $La_{0.9}Sr_{01}Ga_{0.9}Mg_{0.1}O_{2.9}$ [13] and $Ce_{0.9}Gd_{0.1}O_{1.95}$ [14]. The fast oxygen ion diffusion of the NBT is attributed to the high polarizability of Bi^{3+} cations and is mediated by oxygen vacancies,[12] which are introduced by changing the NBT compositions through Bi deficiency and/or Mg doping[12,15]. As a newly reported oxygen conductor, this NBT material may potentially achieve an even higher oxygen-ion conductivity.

Further improvement of the NBT ionic conductor materials requires the understanding of oxygen diffusion mechanisms in the perovskite crystal structures of the NBT material. The Mg doping has been the only doping methods demonstrated for the NBT material,[12] and the doping of other elements is still to be explored. In particular, the doping at the Na/Bi sites instead of the Ti-site substitutions have not been investigated. Given that the off-stoichiometry of the Na and Bi sites of the perovskites have shown to greatly impact the oxygen diffusion,[12,15] it is of great interests to understand how the atomic configurations of Na and Bi cations and their substitutions affect the atomistic mechanisms of O diffusion. It has been shown in other perovskite materials such as $Gd_{0.5}Ba_{0.5}MO_{3-\delta}$ (M=Mn, Co)[16-18] and $PrBaCo_2O_{5+x}$[19] that the cation ordering increases oxygen ionic conductivity. Therefore, gaining the materials insights in the NBT materials are critical for the design and development of this new family of oxygen ion conductors.

1.1.2. Lithium ionic conductors

Lithium super-ionic conductors (SICs), including $Li_{10}GeP_2S_{12}$ (LGPS)[20], $Li_7P_3S_{11}$[21], lithium garnet (e.g., $Li_7La_3Zr_2O_{12}$[22,23]), and Li^+-conducting NASICON (e.g., $Li_{1.3}Al_{0.3}Ti_{1.7}(PO_4)_3$[24]), achieve high Li ionic conductivity, ~1–10 mS cm^{-1} at room temperature (RT), and low activation energy, ~0.2–0.3 eV. These materials are promising solid electrolytes for the development of next-generation all-solid-state Li-ion batteries, which provide improved safety, higher energy density, and better thermal stability than current organic electrolyte-based Li-ion batteries[9,20,25,26]. Despite significant research efforts, only a few materials out of tens of thousands of known inorganic materials have been identified as SICs. It is of great scientific interests to understand why these SICs can achieve several orders of magnitude faster ionic diffusion than other solid materials and to enable a rationally guided materials design strategy for fast ion conductors.

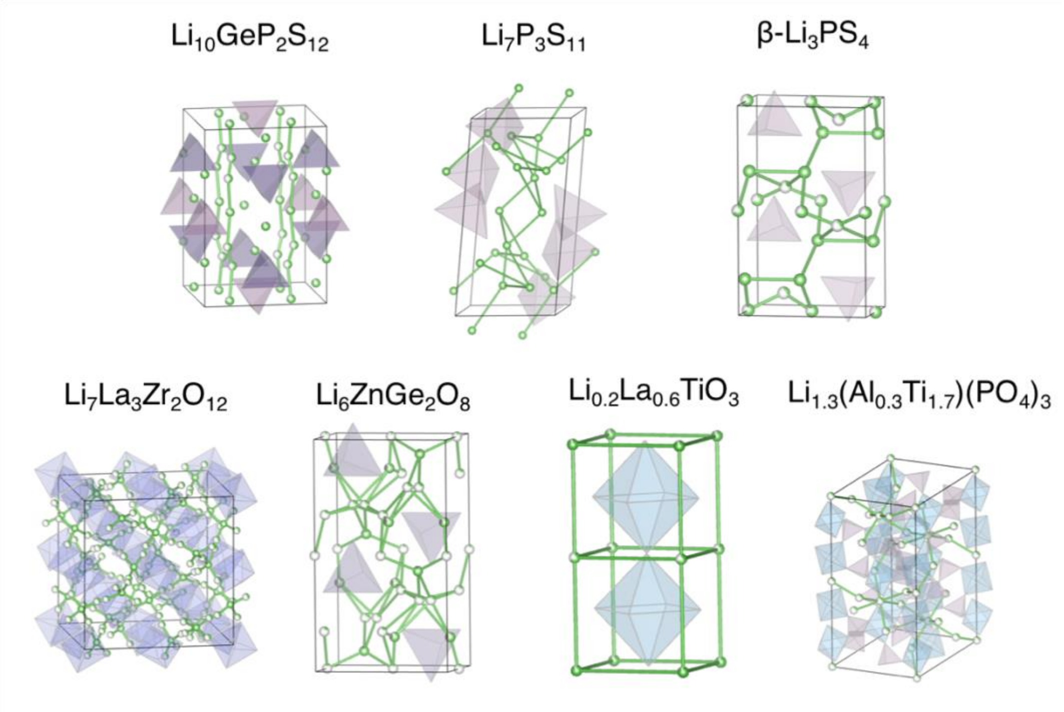

Fig. 1.1. Crystal structures of lithium super-ionic conductors, $Li_{10}GeP_2S_{12}$, Li7P3S11, β-Li_3PS_4, $Li_7La_3Zr_2O_{12}$, $Li_6ZnGe_2O_8$, $Li_{0.2}La_{0.6}TiO_3$, $Li_{1.3}Al_{0.3}Ti_{1.7}(PO_4)_3$. Li sites (partially filled green spheres), Li^+ diffusion channels (green bars), and polyanion groups (polyhedra).

1.1.3. Current understanding on ionic diffusion mechanism

Current understanding of ionic diffusion in solids is based on the classical diffusion model, which describes ionic transport as the hopping of individual ions from one lattice site to another through inter-connected diffusion channels in the crystal structural framework[2]. (Fig. 1.2) The crystal structural framework determines the energy landscape of the ion migration. During ion diffusion, a mobile ion migrates through the energy landscape, and the highest energy of the energy landscape along the diffusion path determines the energy barrier E_a of ionic diffusion. A low activation energy E_a and a high concentration n_c of mobile ion carriers (e.g. vacancies or interstitials) are required to achieve high ionic conductivity σ, which is proportional to $n_c \cdot \exp(-E_a/k_B T)$ at temperature T.

On the basis of this classical diffusion model, current research efforts in the design and discovery of fast ion conductors target materials with crystal structural frameworks that yield an energy landscape of low barriers. For example, the structural framework with body-centered cubic (bcc) anion packing yields the flattest energy landscape with the lowest Li^+ migration barrier, e.g. ~0.2 eV in lithium-abiding sulfides, whereas non-bcc structural frameworks such as in face-centered cubic or hexagonal close-packed exhibit significantly higher energy barriers[26]. Unfortunately, bcc anion packing is a rare structural feature in Li-abiding oxides and sulfides and among known Li SICs is only found in LGPS and $Li_7P_3S_{11}$. Other well-known SICs, such as lithium garnet and NASICON, do not exhibit bcc anion packing but still achieve high Li^+ ionic conductivity of ~1 mS cm^{-1} at RT.

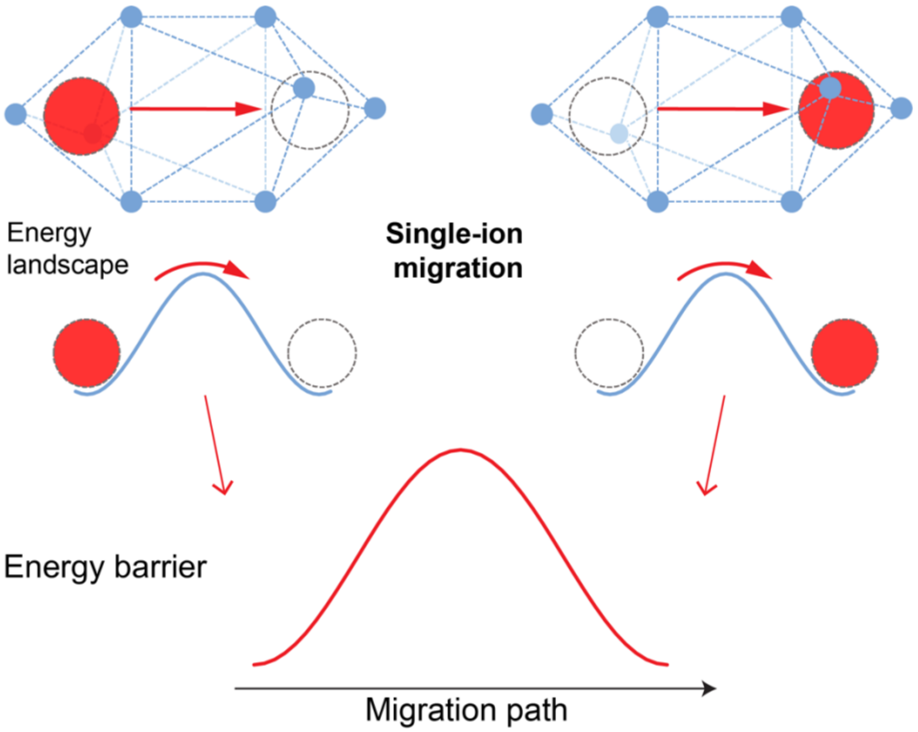

Fig. 1.2. Schematic illustration of single-ion migration in classical diffusion model in typical solids.

Super-ionic conduction is known to be activated at high mobile ion concentration n_c and specific mobile ion sublattice configuration achieved through materials doping. For example, Li garnet achieves the highest RT Li conductivity, σ_{RT} = ~0.1 to 1 mS cm^{-1} (E_a = ~0.3 eV), at 6.4–7.0 Li per formula unit in the doped, cubic-phase $Li_7La_3Zr_2O_{12}$ compositions[23,27,28], whereas $Li_5La_3Ta_2O_{12}$ composition of the same crystal structural framework only exhibits σ_{RT} = ~10^{-3} mS cm^{-1} (E_a = ~0.5

eV)[29]. Li^+-conducting NASICON $Li_{1+x}Al_xTi_{2-x}(PO_4)_3$ achieves high ionic conductivity σ_{RT} = ~1 mS cm^{-1} (E_a = ~0.3 eV) at $x = 0.2–0.3$ [24], whereas $LiTi_2(PO_4)_3$ composition has only σ_{RT} = ~10^{-3} mS cm^{-1} (E_a = ~0.45 eV)[24,30]. Therefore, the super-ionic conduction in these materials is only activated at certain doped compositions with particular Li^+ sublattice ordering. However, the classical diffusion model, which predicts similar migration barriers for the same crystal framework, fails to capture such super-ionic conduction in these materials. For example, the classical model cannot explain why Li^+ migrations suddenly exhibit significantly lower activation energy barriers in the same crystal structural framework with similar energy landscape, as seen in doped Li garnet and NASICON. The answer to this question may help guide the design of SIC materials, especially those with distinctive crystal structural frameworks that deviate from the optimal bcc anion packing.

1.2. First principles computational methods in understanding diffusion process

Computational modeling can simulate the diffusion process at the length scale of nanometer and time scale of sub-nanosecond, which is not easily accessible in experiments. We can utilize the computational methods to conduct the fundamental study of the diffusion process. Compared to classical simulation methods which have limited choices of reliable potentials to describe the interionic interactions, first principles computations based on density functional theory can study and predict new materials with ab initio level of accuracy and chemical versatility.

1.2.1. Nudged elastic band calculations

It is important in understanding diffusion process to calculate the lowest energy path for the migration of one or several ions from one stable configuration to another. The nudged elastic band (NEB) method is widely used to identify the lowest energy path and calculate the potential energy profile along the path. The transition state with maximum potential energy along the path is the saddle point, which is used to calculate the activation energy barrier of the migration. [31]

1.2.2. Ab initio molecular dynamics simulations

Ab initio molecular dynamics (AIMD) simulation, as a powerful modeling technique, has been recently applied to a wide range of research topics in chemistry and materials science [32-35]. AIMD simulations are carried out using the potential energy surface and atomistic forces calculated from *ab initio* methods such as density functional theory (DFT), and model the dynamics of atomistic systems with *ab initio* level of accuracy and chemical versatility, which are lacking in classical molecular dynamics (MD) simulations based on the interatomic potentials (a.k.a. force fields). Therefore, AIMD simulation is the method of choice for studying the dynamics of atoms with complex chemistry changes and the materials that cannot be described by available interatomic potentials. AIMD simulations have been successfully demonstrated in studying diffusional properties [36-40], reaction processes [41,42], vibrational frequency [43-45], amorphous materials [46-48], phase transition [49], etc.

Mo *et al.*[36] pioneered the application of AIMD simulations for studying ionic diffusion in lithium ionic conductor materials, such as $Li_{10}GeP_2S_{12}$. Since then, AIMD simulation has been widely adopted as a standard technique for studying fast ionic conductor materials with a wide range of mobile species (e.g., Li^+, Na^+, Mg^{2+}, O^{2-}) [37,38,50-54]. AIMD simulations model the real-time dynamics of atoms with a femtosecond-scale time resolution, which is difficult to directly obtain from experimental characterizations or from other computational methods. AIMD simulation technique has achieved great successes in identifying diffusion mechanism at the atomistic scale and in quantifying the diffusional properties.

Major advantages of AIMD simulation are that the diffusion events, i.e., atom/ion hops, in the materials are directly observed from the dynamics and trajectory of atoms and that specific diffusion mechanism is not presumed as calculation input. For example, recent AIMD simulations identified that the diffusion mechanism in lithium super-ionic conductors, such as thio-LISICON [40,55] and lithium garnet [40,56,57], is a concerted migration of multiple ions rather than isolated ion hopping. AIMD simulations played unique roles in uncovering and identifying these concerted migration mechanisms, whereas isolated ion hopping is often assumed for NEB calculations. In addition, AIMD simulations sample the statistical contributions of all diffusional events and obtain the diffusional properties such as diffusivity and ionic conductivity from the collective contributions of all different diffusion modes. In addition, performing AIMD simulations at different temperatures obtains the

Arrhenius relation of diffusivity and ionic conductivity including the pre-factor and overall activation energy, similar to experimental measurements.

1.3. Dissertation overview

This dissertation consists of six chapters.

Chapter 1 gives an introduction about fast ionic conductors, their applications, and first principles computation methods for studying ionic conduction used in this thesis.

Chapter 2 presents our established procedure of using AIMD simulations to quantify diffusivity and ionic conductivity from the AIMD simulations with minimal errors and quantified statistical uncertainties.

Chapter 3 presents a systematical first principles computational study on an oxygen ionic conductor, $Na_{0.5}Bi_{0.5}TiO_3$ to understand the diffusion mechanism and to design the materials with higher ionic conductivity.

Chapter 4 presents our fundamental understanding on the fast ionic diffusion mechanisms in super-ionic conductors. We demonstrate that the concerted migration mechanism with low energy barrier is the general phenomenom in a broad range of ionic conducting materials. We propose and demonstrate new strategies to design new fast ion-conducting materials.

Chapter 5 presents our quantitative analysis on the crystal structural frameworks of fast Li ionic conductors. We performed a high-throughput screening of all lithium-containing oxide and sulfide compounds from inorganic crystal structure database (ICSD) to discover new crystal structural framework for fast ionic conductors.

Finally, we conclude in Chapter 6 with major conclusions of this dissertation and potential future research topics.

Chapter 2: Diffusional properties from ab initio molecular dynamics simulations[2]

2.1. Introduction

Despite *ab initio* accuracy and chemical versatility, *ab initio* calculations require high computational expenses, which limit the accessible length scale and timescale of AIMD simulations. The small system size and short physical time scale are the major shortcomings of AIMD simulations compared to classical MD simulations [58,59]. Even on the state-of-the-art supercomputing facilities, typical AIMD simulations are limited to a system size of a few hundred atoms and a total physical time duration of tens to thousands of picoseconds. As a result, a limited number of diffusion events, i.e., ion hops, are observed during an AIMD simulation. The limited sampling of diffusion events may lead to significant statistical variances in calculated diffusional properties or even to erroneous values if only a few ion hops were sampled.

As AIMD simulation has become a widely used technique in studying diffusion mechanisms and in quantifying diffusional properties of materials, the procedures for applying AIMD simulations to extract diffusional properties need to be systematically established.

---

[2] This chapter has been published in
X. He, Y. Zhu, A. Epstein and Y. Mo. "Statistical Variances of Diffusional Properties from Ab Initio Molecular Dynamics Simulations." NPJ Computational Materials, (2018), 4: 18.

First, the fitting procedure of AIMD simulation results requires a number of steps and parameters (2.2.1–2.2.3). Currently, every study and research group choose their own tested parameters, which may significantly impact obtained diffusional properties as we show in this chapter (2.2.4–2.2.6), but the choice of these parameters have not been discussed.

Second, most previous studies correlated the error bar and statistical uncertainty of diffusivity to the goodness of linear fitting to the Einstein relation. However, as we show in this chapter (section 2.2.7), the goodness of linear fitting to the Einstein relation does not necessarily capture the true statistical variance of fitted diffusivity. Instead, the statistical variance and uncertainty of fitted diffusivity should be a direct consequence of the limited observation of diffusion events (i.e., ion hops) during the MD simulation. In the literature, several studies estimated the errors in the fitted diffusivity from single-particle tracking [60-63], classical MD simulations [64] and kinetic Monte Carlo simulations [65]. However, these studies, which are developed and tested for systems and measurements with a significantly larger number of diffusion events than typical AIMD simulations, are not ideal for analyzing errors from AIMD simulations, where the total number of diffusion events are small.

Third, a significant number of diffusion events should be captured to quantify the diffusion with statistical validity. However, in many studies, the AIMD simulations only capture and sample ion diffusion from a few ion hops with a total mean-squared displacement of a few Angstrom^2. The diffusion properties from such poor sampling of ion hops may have low statistical confidence. The limitation of AIMD simulations should be quantified and charted out.

In summary, the following three problems of using AIMD simulations to study diffusional properties need to be addressed:

1) How to properly extract diffusional properties from the dynamics of atoms with minimal errors?

2) How to quantify the statistical variances of diffusional properties extracted from AIMD simulations?

3) What are the accessible ranges of materials properties and physical conditions for typical AIMD simulations in studying diffusion?

The aim of this chapter is to resolve the aforementioned problems and to establish a systematic procedure for quantifying diffusional properties and their statistical variances from AIMD simulations. In 2.2.1–2.2.4, we examine and establish the proper procedure to extract diffusivity D from the atomic trajectory of AIMD simulations. In 2.2.5, we illustrate the origin and the functional dependence of the statistical variance of the diffusivity D. In 2.2.6, we estimate the proper temperature range for AIMD simulations to obtain D with reasonable accuracy. In 2.2.7, we estimate the errors of activation energy and ionic conductivity from the Arrhenius relation for typical super-ionic conductor materials.

2.2. Results and discussion

2.2.1. Quantifying diffusivity, ionic conductivity and activation energy from AIMD simulations

The diffusional properties are calculated from the trajectory of ions (or atoms) $\boldsymbol{r}_i(t)$ from AIMD simulations. The displacement $\Delta\boldsymbol{r}_i$ of ion *i* from time t_1 to t_2 can be calculated as

$$\Delta\boldsymbol{r}_i(\Delta t) = \boldsymbol{r}_i(t_2) - \boldsymbol{r}_i(t_1), \text{ where } \Delta t = t_2 - t_1. \tag{2.1}$$

The total squared displacement sums up the squared displacement of all mobile ions, $\sum_{i=1}^{N}(|\Delta\boldsymbol{r}_i(\Delta t)|^2)$, and describes the movement of all *N* mobile ions over a time interval Δt. During AIMD simulations over a total time duration t_{tot}, there are many ($N_{\Delta t}$) time intervals with the same duration Δt ($\Delta t < t_{\text{tot}}$) but with different starting time *t*. Since the displacement of ions over Δt reflects the mobility of ions, the total mean squared displacement (*TMSD*) for all diffusional ions over time interval Δt is calculated as

$$TMSD(\Delta t) = \sum_{i=1}^{N}(|\Delta\boldsymbol{r}_i(\Delta t)|^2) = \sum_{i=1}^{N}\frac{1}{N_{\Delta t}}\sum_{t=0}^{t_{tot}-\Delta t}|\boldsymbol{r}_i(\,t+\Delta t) - \boldsymbol{r}_i(t)|^2 \tag{2.2}$$

by averaging over a total of $N_{\Delta t}$ time intervals with the same duration Δt. This averaging over different $N_{\Delta t}$ time intervals provides essential ensemble sampling to obtain more accurate diffusional properties. To estimate the diffusivity of the mobile-ion species, the mean-squared displacement (*MSD*) over time interval Δt is calculated as the *TMSD* per mobile ion:

$$MSD(\Delta t) = \frac{1}{N} TMSD(\Delta t). \tag{2.3}$$

N is the number of ions that are assumed to be the mobile carriers contributing to diffusion.

In general, the dependence of *MSD* over time interval Δt follows a linear relationship if a large amount of diffusional displacement is captured during the MD simulation. The diffusivity of these ions is calculated as the slope of the *MSD* over time interval Δt according to the Einstein relation:

$$D = \frac{MSD(\Delta t)}{2d\Delta t} + D_{\text{offset}}\,, \tag{2.4}$$

where $d = 3$ is the dimension of the system, and the offset D_{offset} of this linear dependence is discussed in later sections. This calculated diffusivity D is the tracer diffusivity of the mobile-ion species and is an intrinsic property of the material at the given condition.

From the diffusivity D, the ionic conductivity is calculated based on the Nernst-Einstein relation:

$$\sigma = \frac{Nq^2}{VkT} D, \tag{2.5}$$

where V is the total volume of the model system, q is the charge of the mobile-ion species, T is the temperature, and k is the Boltzmann constant. By combining Eq. (2.3–2.5), the ionic conductivity is directly determined by $TMSD(\Delta t)/\Delta t$:

$$\sigma = \frac{q^2}{VkT} \frac{TMSD(\Delta t)}{2d\Delta t}\,. \tag{2.6}$$

The ionic conductivity and *TMSD* calculated in Eq. (2.6) are independent of the specific choice of the diffusion carrier, such as vacancy or interstitial. In comparison, the diffusivity *D* can be calculated for specific carriers, e.g. Li^+ or vacancy, by normalizing the specific number of carriers in Eq. (2.3). The choice and counting of mobile carriers do not affect the calculated ionic conductivity from Eq. (2.6). Therefore, the use of conductivity and *TMSD* is more straightforward in describing the overall diffusion that occurred during the AIMD simulations.

In addition, the Nernst-Einstein relation (Eq. (2.5)) assumes dilute, non-interacting mobile ions in the materials systems. However, recent AIMD simulation studies have shown the strong correlation of the ionic diffusion in fast ionic conductors [40,55-57,66-68]. The Haven ratio is often used to describe the correlation factor, and can be quantified by the ratio of the jump diffusion coefficient D_J against the tracer diffusivity *D* calculated from Eq. (2.4) [69-71]. The jump diffusion coefficient D_J, which describes the collective migration of all ions, is estimated from the *MSD* of the mass center of all mobile ions. However, our analysis found that tracking the displacement of the single center point exhibits higher statistical variance. In this chpater, the scheme for estimating statistical variance is developed for tracer diffusivity *D* in Eq. (2.5-2.6), but a similar scheme can be applied and developed for analyzing the variance of D_J.

As in the experiments [20,22,72,73], AIMD simulations can be performed at multiple temperatures to obtain the Arrhenius relation of *D* as a function of *T*:

$$D = D_0 \exp(-\frac{E_a}{kT}). \tag{2.7}$$

The activation energy E_a of ion diffusion can be obtained through fitting the data of log D versus $1/T$ to the Arrhenius relationship (Eq. (2.7)). The fitted Arrhenius relationship can be used to extrapolate the diffusivity D and conductivity σ to other temperatures. It should be noted that, by extrapolating this Arrhenius relation to other temperatures, the identical diffusion mechanism is assumed at those extrapolated temperatures.

2.2.2. Regions of MSD-Δt dependence

Fig. 2.1 shows a typical MSD-Δt curve from AIMD simulations of the Li-ion superionic conductor LATP. The linear MSD-Δt dependence as described in the Einstein relationship (Eq. (4)) only holds within a certain range of time intervals Δt, and a notable fraction of this dependence is not linear. The MSD-Δt curve at short time interval $\Delta t < 0.1$ ps follows $MSD \propto \Delta t^{1.42}$, which is consistent with the local harmonic vibration motion model as shown in the Figure 2.3. This portion of the MSD-Δt curve is named the ballistic region, corresponding to the ballistic and vibrational motion of Li ions around their local equilibrium sites rather than Li-ion hopping to new sites [64,74]. More details of this ballistic region are discussed in the next section.

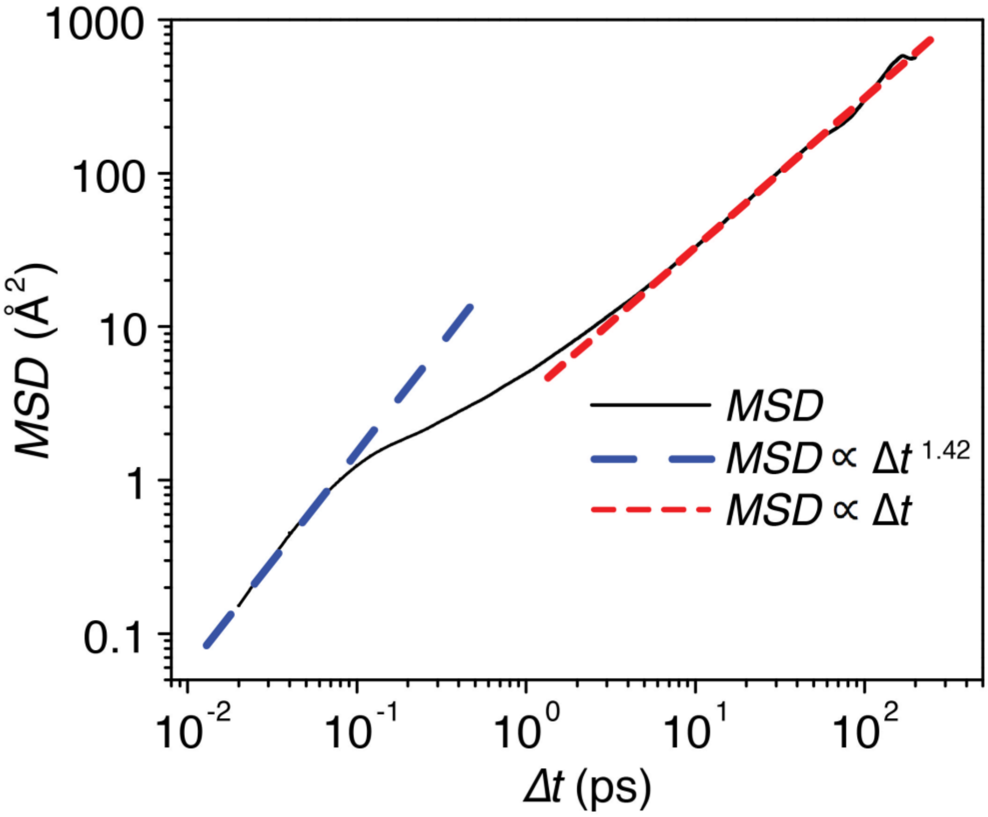

Fig. 2.1. MSD of Li$^+$ as a function of Δt in LATP from an AIMD simulation over 200 ps at 1200 K. The linear $MSD \propto \Delta t$ dependence (red dash line) corresponds to diffusional displacement. The $MSD \propto \Delta t^{1.42}$ dependence (blue dash line) shows the behavior for the local vibrational motion of ions. (Inset) the MSD-Δt curve at < 0.1ps in linear-scale axes.

In Δt range of 10 to 100 ps, the MSD-Δt curve follows $MSD \propto \Delta t$, the linear Einstein relationship for diffusional displacement. However, when Δt reaches a large fraction of t_{tot} (>100 ps in the case of Fig. 2.1), the MSD-Δt curve shows notable variance and deviation from the linear relationship. This deviation is a result of poor statistics for large Δt values, as values that are comparable to t_{tot} result in averaging a smaller number of time intervals $N_{\Delta t}$ in Eq. (2.2) than would be averaged for small Δt values that are a small fraction of t_{tot}. The effect of this deviation is quantified in the next section.

Given that the linear MSD-Δt dependence only holds at certain Δt range, one should not utilize the entire MSD-Δt curve to fit the Einstein relation (Eq. (2.4)) and to deduce the diffusivity. The ballistic region at short times intervals and the poor statistical region at large time intervals should be excluded from fitting diffusivity. The linear fitting of MSD-Δt curve should be performed in a range $[\Delta t_{low}, \Delta t_{up}]$, where Δt_{low} and Δt_{up} are the lower and upper bound, respectively. In last sections, we establish the procedures to determine the bounds Δt_{low} and Δt_{up} for the linear fitting of MSD-Δt in order to minimize the errors caused by improper fitting to the Einstein relation.

2.2.3. Lower bound of linear diffusion region

In Fig. 2.2, the local derivative $dMSD/d\Delta t$ calculated using a finite difference method shows the transition from the ballistic region to the linear region and is used to determine the lower fitting bound Δt_{low}. The derivative $dMSD/d\Delta t$ has a large value at small Δt values (< 0.2 ps), and decreases significantly as Δt increases. The MSD-Δt curve becomes linear at $\Delta t >$ ~1 ps, and the value of $dMSD/d\Delta t$ reaches a plateau value of ~3 Å^2/ps. In the case of Fig. 2.2, the cut-off of the ballistic region (black dotted line in Fig. 2.2) is at an *MSD* value of ~5 Å^2. An *MSD* of 5 Å^2 is approximately 0.5a^2, where a is the distance between two neighboring Li sites and is 3.2 Å in LATP, which is typical of Li ionic conductors. The ballistic region has the *MSD* cut-off at a fraction of a^2 because the local vibration of Li ions on their equilibrium sites is confined within the potential well between two nearby sites. This local vibrational displacement at small $\Delta t < \Delta t_{low}$ does not represent the ionic diffusion from site to site, and should be excluded from the linear fitting for D.

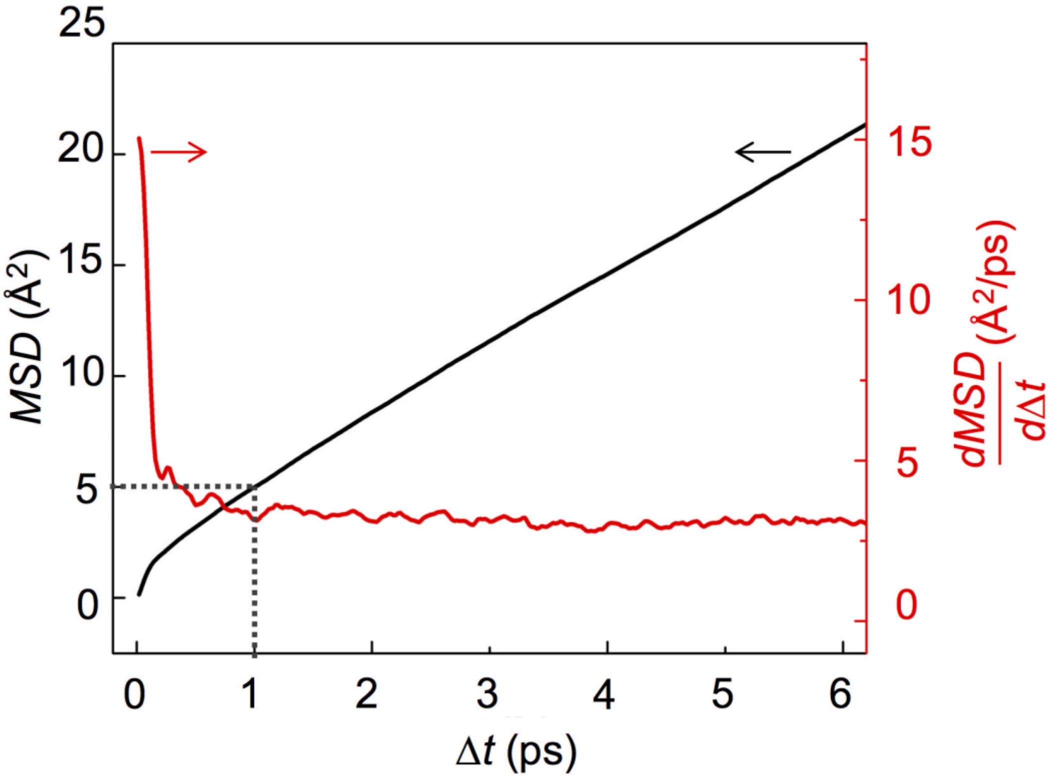

Fig. 2.2. *MSD* (black) of Li^+ and *dMSD/d*Δ*t* (red) as a function of Δ*t* from the AIMD simulation of LATP in Fig. 2.1. The black dotted line illustrates the cut-off of the ballistic region.

One may identify the specific range of the ballistic region and the precise lower fitting bound Δt_{low} for each individual AIMD simulation of different materials systems at different temperatures using the same procedure shown in Fig. 2.1 and 2.2. The cut-off values of Δ*t* (i.e., Δt_{low}) and *MSD* for the ballistic region are dependent on the temperatures and the materials, which yield different potential energy surfaces near the equilibrium sites. In general, the displacement of local vibration is within a fraction of site distance *a*, so the ballistic region corresponds to the *MSD* ranging from 0 to a fraction of a^2 (Fig. 2.3). Therefore, we propose to quantify the cut-off values of Δ*t*, i.e., Δt_{low}, by defining the cut-off in *MSD* using the value of a fraction of a^2 (e.g. 0.5 a^2). As a safer measure for lower fitting bound (i.e., Δt_{low}), the entire region with *MSD* less than this cut-off based on a^2 may be excluded.

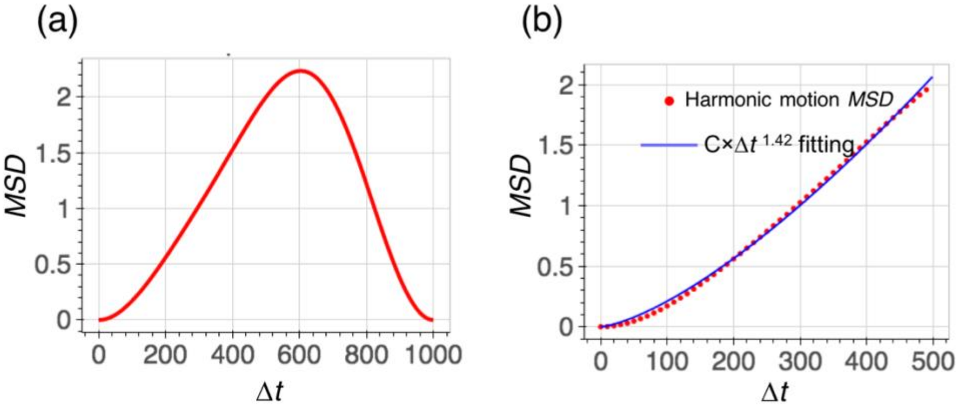

Fig. 2.3. **Harmonic motion model.** (a) The *MSD* as a function of Δ*t* for simple harmonic vibration, and (b) *MSD*-Δ*t* curve at $0 < \Delta t < 500$ gives a dependence of $\Delta t^{1.42}$.

The linear fitting to Einstein relation should only be performed on the linear region corresponding to diffusional displacement. Otherwise, a part of ballistic motion would be included into the fitting for *D*, leading to an over-estimation of *D*. This over-estimation of *D* would be pronounced for the *MSD*-Δ*t* curves with small values of the maximum *MSD* (~a few Å^2), due to a significant fraction of ballistic motion mixed into the *MSD*-Δ*t* curve. Therefore, AIMD simulation should be long enough to have the *MSD* per mobile ion larger than a few a^2, so that the ballistic region (and Δt_{low}) can be distinguished and separated from the linear fitting for *D*.

2.2.4. Upper bound of linear diffusion region

The upper fitting bound Δt_{up} is determined by the transition from the linear diffusion region to the region at large Δt with large variance and deviation. Ten different *MSD*-Δt curves from AIMD simulations of the same LATP structure model at 1200 K over 50 ps (Fig. 2.4a) were obtained by dividing a total AIMD simulation over 500 ps into ten non-overlapping parts. The significant deviations from the linear dependence of these ten *MSD*-Δt curves are typically observed at large values of Δt, i.e., > 25 ps in Fig. 2.3 or >~50% of t_{tot}. At large Δt, a smaller number of time intervals $N_{\Delta t}$ is averaged in Eq. (2.2) and many of these Δt intervals overlap other intervals that contain physically identical trajectories of ions, thus leading to larger deviation from the linear *MSD*-Δt relation. Therefore, the linear fitting for *D* should be performed below the upper bound Δt_{up} of the linear diffusion region.

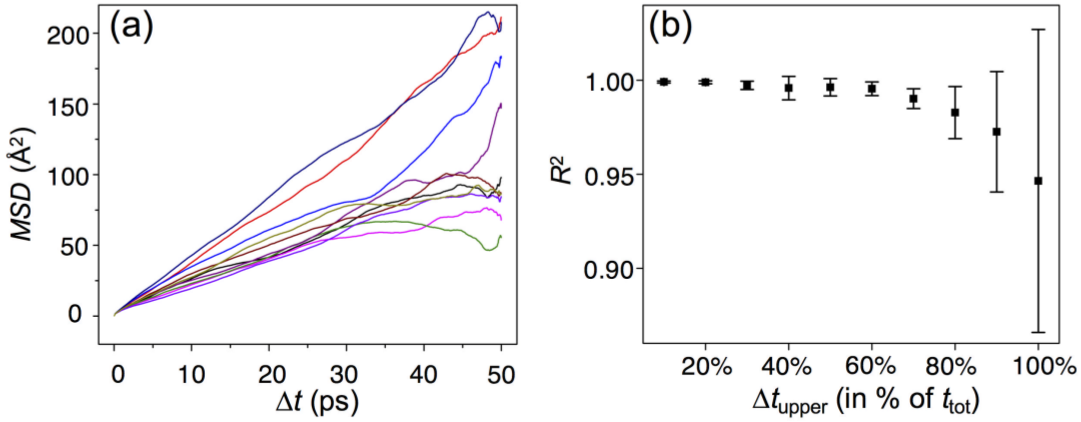

Fig. 2.4. Variances of *MSD*-Δ*t* curves. (a) *MSD*-Δ*t* curves from ten different AIMD simulations of the same LATP structure model over 50 ps at 1200 K. Each curve represents an independent AIMD simulation over 50ps (t_{tot} = 50 ps). (b) Goodness of linear fit R^2 of *MSD*-Δ*t* curves using different upper fitting bound. The values and error bars of R^2 are the average and the standard deviation, respectively, from ten AIMD simulations.

To determine the upper fitting bound Δt_{up}, we fitted these *MSD*-Δ*t* curves to the Einstein relation (Eq. (2.4)) with different Δt_{up} values ranging from 10% to 100% of t_{tot}. For the fitting of each curve, the value of R^2 in the linear regression was calculated to evaluate the goodness of fitting. The average and standard deviation of R^2 values over these 10 curves are shown in Fig. 2.4b. At $\Delta t_{up} \leq 0.3t_{\mathrm{tot}}$, all values of R^2 are very close to 1, showing good linearity of *MSD*-Δ*t* curves at small Δ*t*. At $\Delta t_{up} > 0.7t_{tot}$, R^2 values decrease significantly from 1, indicating poor linearity of *MSD*-Δ*t* curves at large Δt, and the standard deviation of R^2 also increases. Therefore, one should only fit the linear region of *MSD*-Δt below an upper fitting bound of $< 0.7t_{\text{tot}}$. By performing the same test on other fast ion conductor materials, such as LGPS and LLZO at a few different temperatures, we found this $\Delta t_{up} < 0.7t_{\text{tot}}$ to be generally applicable (Fig. 2.5). As the optimal Δt_{up} values may depend on the material (the mobile ions) and temperatures, for unique systems one may use this scheme to determine the specific Δt_{up} values.

Within properly determined lower and upper fitting bounds, the goodness of fitting to the *MSD*-Δt curve would always be good. Therefore, the goodness of fitting itself does not reflect the statistical variance in the fitted *D*, the slope of the *MSD*-Δt curve, and is different among different AIMD simulations for the same materials model (Fig. 2.4a). The changes in the slopes of *MSD*-Δt curves below Δt_{up} reflect the statistical variances in the fitted diffusivity *D* from different runs of AIMD simulations, which are quantified and analyzed in the next section.

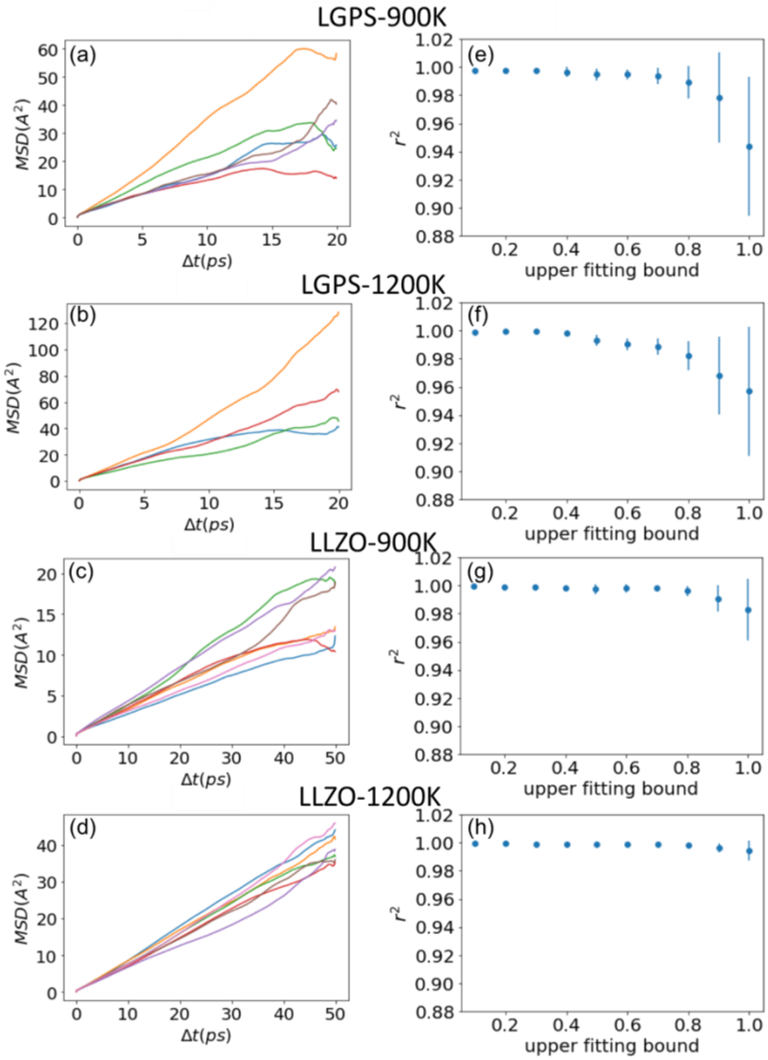

Fig. 2.5. **Upper fitting bound analysis of LGPS and LLZO.** (a-d) *MSD*-Δ*t* curves from several different AIMD simulations of the same LGPS (a-b) and LLZO (c-d) at 900 K (a, c) and 1200 K (b, d). Each curve represents an independent AIMD simulation. (e-h) Goodness of linear fit R^2 of *MSD*-Δ*t* curves for LGPS (e-f) and LLZO (g-h) at 900 K (e, g) and 1200 K (f, h) using different upper fitting bounds. The values and error bars of R^2 are the average and the standard deviation, respectively, from a number of AIMD simulations.

2.2.5. Statistical variance of diffusivity and conductivity

In Fig. 2.4a, the diffusivities, i.e. the slopes of different MSD-Δt curves, exhibit significant variance among different AIMD simulations of the exact same material model. The variance among the fitted diffusivities D are a result of the stochastic nature of the diffusion process, which causes different numbers of ion hops during AIMD simulations with different initial conditions.

In this section, we quantify the statistical variance of the fitted diffusivity D from AIMD simulations. The statistics were calculated based on a set of MD simulations that were created by dividing a long MD simulation into several non-overlapping shorter MD simulations, each of which was treated as an individual MD simulation. Following our established fitting procedure, the value of D was extracted from each MD simulation. The standard deviation of D, s_D, was calculated from the set of fitted D values. The relative standard deviation (RSD) of D was calculated as s_D/D_{true}, where the true value of the diffusivity D_{true} is calculated from the longest available MD simulation. Since more ion hops improve the sampling of the diffusional property, we found that the RSD of D decreases with the total effective ion hops N_{eff} as

$$\frac{s_D}{D_{\mathrm{true}}} = \frac{A}{\sqrt{N_{\mathrm{eff}}}} + B \ . \tag{2.8}$$

N_{eff} is calculated as

$$N_{\text{eff}} = \frac{\max\limits_{\Delta t}[TMSD(\Delta t)]}{a^2}, \qquad (2.9)$$

where $\max\limits_{\Delta t}[TMSD(\Delta t)]$ is the maximum value of *TMSD* over the entire *MSD*-Δt curve. N_{eff} can be considered as the effective number of ion hops that contributed to the *TMSD* of all mobile ions in the entire duration of the MD simulation. The value of a is 2.4, 3.2, 2.8, 3.4 Å for LLZO, LATP, LGPS, $RbAg_4I_5$, respectively, as averaged distance between neighboring mobile-ion sites. For all materials in Fig. 2.6, the values of *A* and *B* are fitted as 3.43 and 0.04, respectively. As shown in Fig. 2.6, Eq. (2.8) and its parameters are general for ionic conductor materials and also hold for a classical MD simulation of LLZO over much longer time duration with a large number of ion hops (Fig. 2.6b).

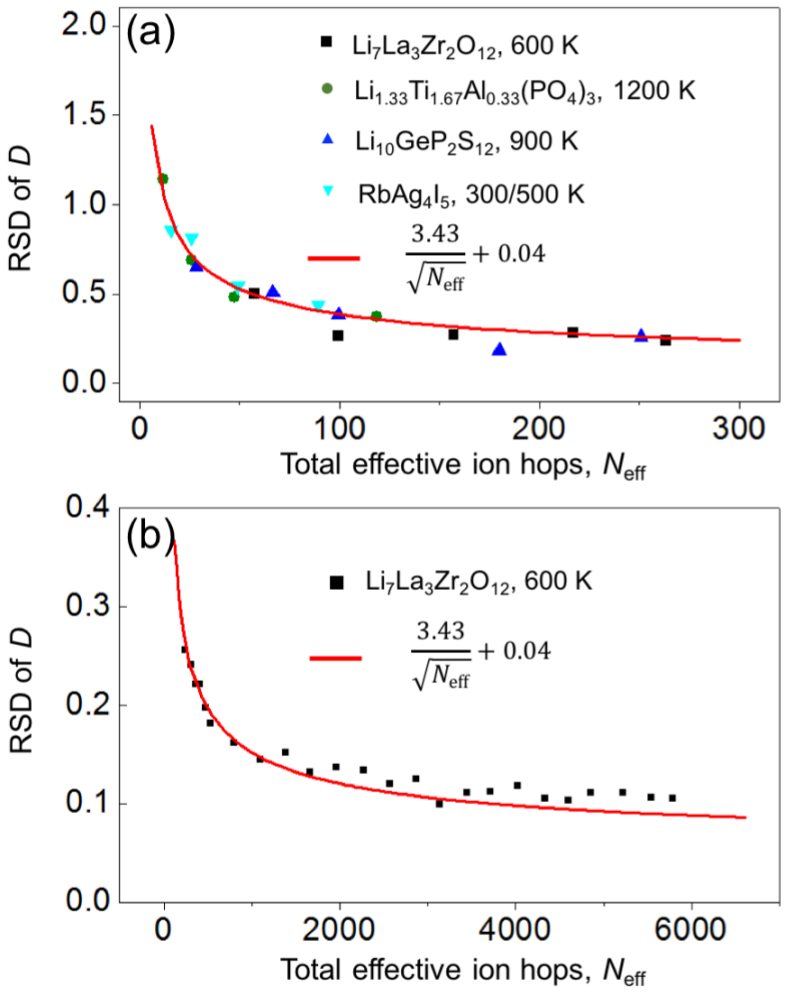

Fig. 2.6. Relative standard deviation (RSD) of D, s_D/D_{true}, as a function of total effective hops N_{eff} of the mobile ion (Li^+ or Ag^+). Red line is the fitted relationship between RSD of D and the total effective ion hops N_{eff}.

Eq. (2.8) can be used to estimate the statistical variance of D calculated from any given AIMD simulation, where the number of total effective ion hops N_{eff} can be first estimated from the maximum $TMSD$ of all mobile ions using Eq. (2.9). For example, in a material with site distance a = 3 Å (assumed for all following estimations), an AIMD simulation that reaches a maximum *TMSD* of 1800 Å^2, corresponding to N_{eff} = ~200, results in an RSD of D of ~28%. In addition, since the diffusivity D and ionic conductivity σ are linearly dependent (Eq. (2.5)), the RSD of σ is equivalent to the RSD of D. Thus, Eq. (2.8) is also valid for estimating the *RSD* of ionic conductivity σ from AIMD simulations.

This result suggests that in order to obtain more accurate diffusivity from AIMD simulations, one should run longer MD simulations that sample more diffusion events, i.e., have larger N_{eff}. For AIMD simulations with an estimated N_{eff} of 50, 100, and 150, corresponding to max(*TMSD*) of 450, 900, and 1350 Å^2, respectively, RSD of D is 52%, 38%, and 32%, respectively. These levels of RSD are reasonable, but still allow for a notable statistical error of the fitted D. To obtain D with <20% RSD, the AIMD simulation should observe more than max(*TMSD*) of ~4150 Å^2 (N_{eff} =~460). The RSD is reduced to ~10% for N_{eff} = 3200 and max(*TMSD*) = ~30000 Å^2. It should be noted that N_{eff} and *TMSD* are from all mobile ions, while only *MSD* per ion is often presented in the literature. A max(*TMSD*) of a few thousand Å^2 is quite significant for typical AIMD simulations within 1 ns and can only be reached in fast ion conductors at relatively high temperatures. In addition to running longer MD simulations, running MD simulations on larger systems with more mobile ions, for example as is done in classical MD simulations, can achieve more effective ion hops N_{eff} and hence less statistical variance in D and σ.

2.2.6. Accessible range of diffusivity, activation energy, and temperature

Given the short physical time duration of 100 ps to 1 ns in typical AIMD simulations, AIMD simulations of materials with large activation energy E_a or at low temperature T may not observe enough number of ion hops. In order to achieve a reasonable accuracy of the fitted D, AIMD simulations may only be applicable to materials with relatively high ionic conductivity. Given the high computational costs of AIMD simulations, it is often desired to pre-estimate the range of temperatures that can be performed for a given material (with an estimated E_a). The accessible ranges of T at a given E_a can be estimated as follows. The estimation here assumes an AIMD simulation over a total physical time duration of 1 ns and a supercell with a volume V of 1000 Å^3 (i.e., 10Å×10Å×10Å) with N=20 mobile ions and a site distance a = 3 Å. In order to achieve < 50% RSD of D and σ, N_{eff} should be >55 according to Eq. (2.8). For this RSD limit, the ionic conductivity should be >0.025 S/cm at 600 K to achieve $N_{\mathrm{eff}} > 55$ over 1 ns (Eq. (2.4) and (2.5)). This ionic conductivity corresponds to a Li$^+$ diffusivity of ~4.2×10^{-7} cm^2/s (Eq. (2.5)) for the assumed supercell model. For the materials supercell with different size V or different number of mobile carriers N, the accessible range of diffusivity can be estimated in the same way using Eq. (2.5-2.8). In general, a minimum diffusivity of ~10^{-7} cm^2/s is accessible by the AIMD simulations with typical size (~1 nm^3) and time duration (~1 ns), in order to have a reasonable number of effective ion hops ($N_{\mathrm{eff}} > 50$).

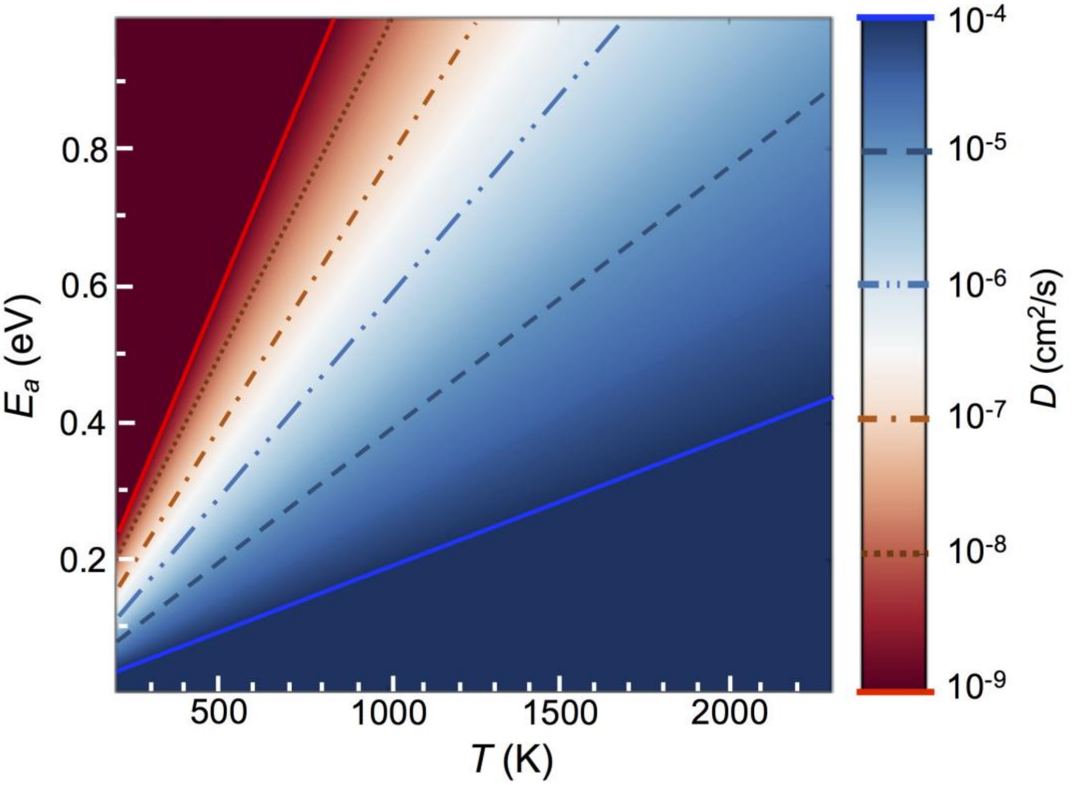

Fig. 2.7. Diffusivity D as a function of activation energy E_a and temperature T for a typical ionic conductor with assumed site distance a = 3 Å and an attempting frequency $\nu = 10^{12}$ Hz.

Figure 2.7 shows a plot of D as a function of E_a and T estimated from the transition state theory

$$D = a^2 v^* \exp\left(-\frac{E_a}{kT}\right), \tag{2.10}$$

where v^* is the attempting jump frequency and is chosen to be 10^{12} Hz, a is the neighboring-site distance, and k is the Boltzmann constant. The geometric factor and correlation factor, which also affect the value of D, were neglected in this back-of-the-envelope estimation. This plot can be used to estimate the range of E_a and T accessible to typical AIMD simulations. In the same example model above, a minimum diffusivity of ~5×10^{-7} cm^2/s is needed to achieve an RSD of ~50% within 1 ns. The highest E_a and lowest temperatures to have the desired D value can be read from this plot (Fig. 2.7). For materials with an E_a of 0.6 eV, as in some cathode materials, AIMD simulations below 900 K may not observe enough ion hops and the fitted D would have a large error. For super ionic conductors with an E_a of 0.20 eV or lower, the temperature accessible by AIMD simulations may go as low as 300 K.

In addition, this plot can be used to determine the appropriate temperatures for AIMD simulations to obtain D with reasonable accuracy. For example, in order to achieve a desired RSD of ~20%, a maximum *TMSD* of 4150 Å^2 over 1 ns is needed (Eq. (2.7–2.8)), and this maximum *TMSD* corresponds to a minimum diffusivity of ~3×10^{-6} cm^2/s (Eq. (2.5)) in the same example material model. To achieve that diffusivity, AIMD simulations of a material with E_a of 0.2 eV need to be at above 450 K (Fig. 2.7). An ionic conductor with E_a of 0.3 eV should have AIMD simulations above 700 K to achieve similar accuracy (RSD =~20%). An AIMD simulation at >1150K is needed for an ionic conductor with E_a of 0.5 eV. Therefore, for materials with slow diffusion, long AIMD simulations at high temperatures are essential to obtain D with low statistical uncertainty. In general, AIMD simulations containing a significant number of ion hops are crucial for achieving small error bounds and a high confidence level in the fitted D.

2.2.7. Estimating errors of diffusional properties from Arrhenius relation

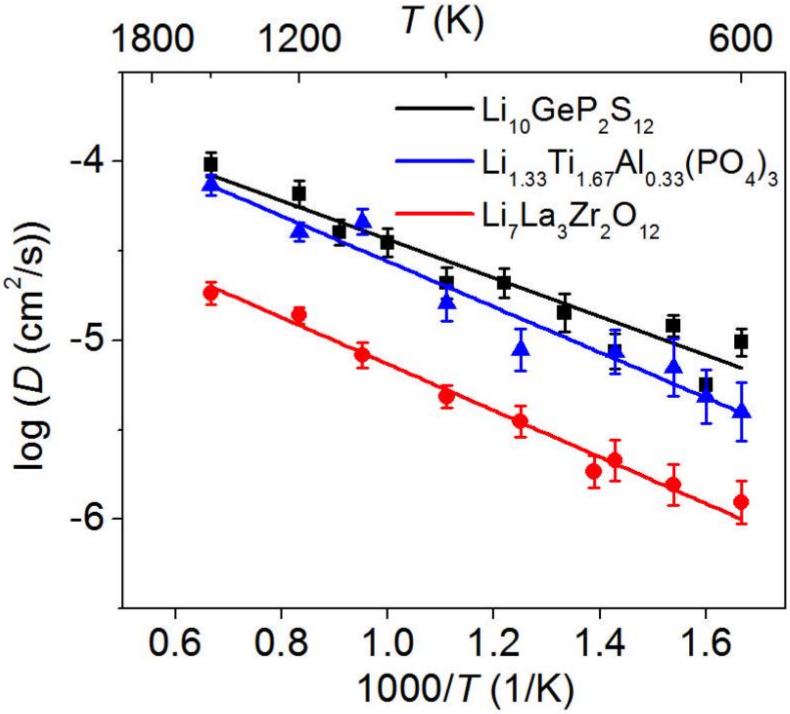

Fig. 2.8. Arrhenius plot of Li^+ diffusivity *D* as a function of temperature *T* in $Li_{1.33}Ti_{1.67}Al_{0.33}(PO_4)_3$ (LATP), $Li_{10}GeP_2S_{12}$ (LGPS) and $Li_7La_3Zr_2O_{12}$ (LLZO) from AIMD simulations. The error bar is the statistical uncertainty of each diffusivity data point estimated from Eq. (2.7–2.9).

Given the statistical uncertainty of fitted *D*, it is crucial to include the statistical uncertainty of every *D* data point into the fitting of Arrhenius relation. In particular, the data points from the simulations at lower temperatures or over shorter durations may have a significantly smaller number of ion hops and thus a higher uncertainty, and this uncertainty should be taken into account during the fitting. The data points in Fig. 2.8 indeed show significantly larger variance at lower temperatures. Therefore, these lower-temperature data points should have less weight in the fitting. As a common practice in linear regression, the inverse square of the standard deviation of log(D) is factored into the fitting as the weight of each data point to account for the statistical uncertainty [75]. Given that the fitting of the Arrhenius relationship is usually performed as a linear fitting of log(D) and 1/T, the derived standard deviation of log(D) shall be used as the weight on each point (as shown as error bars in Fig. 2.8) for the linear fitting . Therefore, the error bounds and statistical intervals of E_a and D_0 in the Arrhenius relation (Eq. (2.7)) can be obtained using standard error analysis for linear regression, and so are also the errors for diffusivity and conductivity when extrapolated to other temperatures.

Table 2.1. Activation energy E_a and extrapolated Li$^+$ conductivity σ at 300 K from fitted Arrhenius relation.

Composition	E_a (eV)	σ at 300 K (mS cm^{-1})	Error bound [σ_{min}, σ_{max}] (mS cm^{-1})
$Li_{1.33}Ti_{1.67}Al_{0.33}(PO_4)_3$	0.25 ± 0.02	1.2	[0.5, 2.5]
$Li_{10}GeP_2S_{12}$	0.21 ± 0.01	14.2	[8.1, 25.0]
$Li_7La_3Zr_2O_{12}$	0.26 ± 0.02	1.1	[0.5, 2.1]

Table 2.1 shows the error bounds of the activation energy E_a and ionic conductivity σ extrapolated to 300 K for LATP, LGPS and LLZO Li-ion conductors. E_a and extrapolated σ at 300 K agree well with experimental values, showing the

capability of AIMD simulations for quantifying diffusional properties.[20,22,24,76] For all three materials, the E_a has a standard deviation of ~0.02 eV, and the extrapolated σ at 300 K has the error bound within 1-2 orders of magnitude. It should be noted that extrapolated conductivity (i.e. room temperature conductivity) assumes that there is no change in the slope of the Arrhenius relation due to a phase change. While excellent agreement of AIMD simulations and experiments is widely reported, one should note that the statistical uncertainty of extrapolated σ at 300 K can be as large as an order of magnitude for typical AIMD simulations. The errors in E_a and σ may be larger for AIMD simulations over shorter duration or on slower ion conductors, which sample fewer diffusion events. Using short AIMD simulations, especially at low temperatures, would lead to significant overestimation of diffusivity and, in particular, the RT conductivity.

In addition, the errors of E_a and extrapolated σ also depend on the number of data points and the linearity of the relationship according to the error analyses of linear regression [75]. To minimize the error of E_a and extrapolated σ, more data points are helpful. For example, the error of E_a and σ may increase significantly if some data points are omitted for the LGPS data in Fig. 2.8, leading to more deviations from the experimental values. Therefore, having more data points of D (from sufficiently long AIMD simulations) would lead to smaller error and less statistical uncertainty for fitted diffusional properties.

2.2.8. Discussion

In this chapter, we systematically test and establish the procedures to obtain the diffusional properties and their statistical variances from AIMD simulations. Only the linear region of the *MSD*-Δt curve within the lower and upper fitting bound Δt_{low} and Δt_{up}, which corresponds to diffusional displacements, should be used to fit the diffusivity. The cut-off of the ballistic region, Δt_{low}, is at the *MSD* per mobile ion of less than a fraction of a^2 (a is the distance between neighboring mobile-ion sites), since the local ballistic vibration is limited within the potential well of the equilibrium site. The AIMD simulation should be long enough to have the *MSD* per mobile ion larger than a few times a^2 so that the distinction between the linear diffusion region and the ballistic region can be clearly observed. Otherwise, a part of ballistic motion would be mixed into the fitting, leading to the over-estimation of *D*. Moreover, the upper fitting bound Δt_{up} should be set as <30%–70% of t_{tot} to exclude the region with poor linearity at large Δt. An adequately long AIMD simulation with properly determined lower and upper fitting bounds is crucial to have a linear *MSD*-Δt curve for fitting *D*.

If the proper procedure is followed to determine the linear diffusion region of the *MSD*-Δt curve, the goodness of fitting to the *MSD*-Δt curve would be nearly perfect and would not reflect the statistical variance of the fitted diffusivity. The statistical variance of the fitted diffusivity and conductivity is instead a direct result of the total number of ion hops sampled during the MD simulations. The statistical variances of *D* from fitting Einstein relation should be quantified by the total displacement *TMSD* using the empirically determined relation in Eq. (2.8).

On the basis of these results, AIMD simulations should be adequately long to collect a sufficient number of ion hopping events. As shown in typical alkali-ion conductor materials, a simple rule of thumb is that a maximum *TMSD* of a few hundred Å^2 is necessary to obtain a reasonable estimation of *D* (with ~50% RSD), and a maximum *TMSD* of a few thousand Å^2 is necessary to obtain a more accurate *D* (~20–30% RSD). Given the high uncertainty of *D* from typical AIMD simulations, the error bounds of diffusivity and conductivity should be reported.

Given the need to collect a large number of ion hops, AIMD simulation is more suitable for studying fast-ion-conducting materials. Likewise, it is necessary to perform AIMD simulations at high temperature for most materials. A minimum diffusivity of ~10^{-7} cm^2/s is necessary for a material to be accessible by AIMD simulations and a diffusivity of ~10^{-5} cm^2/s may allow for the calculation of a more accurate *D*. On the basis of these estimated bounds of minimum diffusivity, the approximate accessible temperature ranges of AIMD simulations may be estimated using the plot in Fig. 2.5 or using a back-of-the-envelope estimation based on the Arrhenius relation. For materials with a high activation energy, running AIMD simulations at sufficiently high temperatures is crucial for simulating an adequate number of ion hops.

In addition, it is also crucial to include the statistical error bounds of each diffusivity data point when fitting to the Arrhenius relation (Eq. (2.7)). The error bounds of D should be accounted for as a weight into the linear fitting of log(D) over 1/T. The error of E_a and extrapolated σ can be established through standard regression error analysis. Such error analyses indicate that the typical statistical error bounds of extrapolated σ at 300 K may be as large as an order of magnitude, even for fast ionic conductors with many data points at different temperatures and with long AIMD simulations. One should consider the statistical variances when interpreting the diffusional properties calculated from AIMD simulations.

While the results of this chapter are largely based on AIMD simulations, our analyses, schemes, and conclusions are applicable for diffusional studies using classical MD simulations. While AIMD simulations provide *ab initio* potential energy surfaces, leading to more accurate diffusion properties, classical MD simulations can be performed on significantly larger model systems with more mobile ions and over longer time scales, so more diffusional events can be observed. When the *TMSD* and total effective ion hops N_{eff} from classical MD simulations are large, the statistical variances of diffusional properties are expected to be small. However, in classical MD simulations in which *TMSD* or N_{eff} is small, which is common for systems with slow diffusion or at low temperatures, our scheme and analyses should be carried out to properly quantify diffusional properties and their statistical variances.

2.3. Conclusion

In summary, the major conclusions for calculating diffusional properties from AIMD simulations are as follows. These conclusions also serve as specific guidelines for future practices.

1) In the calculation of diffusivity, fitting to the Einstein relation (Eq. (2.4)) should be limited to the linear diffusion region of the MSD-Δt curve. This linear diffusion region excludes the ballistic region at $MSD < \sim a^2$ and the poor linearity region at large $\Delta t > \Delta t_{up}$ ($\Delta t_{up} < 0.7 t_{\mathrm{tot}}$).
2) The AIMD simulations should be long enough and should only be performed on materials with reasonably fast diffusion so that a large number of diffusion events can be captured to obtain accurate diffusivity. In addition, the *MSD* per mobile ion should be larger than a few times a^2 to distinguish the ballistic region (i.e., Δt_{low}).
3) The statistical variance of the diffusivity should be derived from the total diffusional displacements (such as maximum *TMSD* using Eq. (2.8-2.9)) rather than the goodness of fitting to the Einstein relation. The statistical variance of fitted diffusivity values from AIMD simulations should be reported.
4) The statistical uncertainties of each data point of diffusivity should be included when fitting to the Arrhenius relation. The error bounds of activation energy and extrapolated ionic conductivity are non-negligible and should be evaluated using standard regression analysis.

Our study establishes the proper calculation procedures and statistical error analyses for the correct application of AIMD simulations in estimating diffusional properties. The obtained knowledge and established procedures are the basis for quantifying diffusional properties, drawing proper conclusions from the AIMD simulation results, and further developing AIMD simulations.

Chapter 3: Materials design of $Na_{0.5}Bi_{0.5}TiO_3$ oxygen ionic conductors[3]

3.1. Introduction

In this chapter, we establish the structure-property relationship of the NBT materials using first principles computation techniques, to understand the O diffusion mechanisms in the NBT material with different cation sublattice or with different doping, and to design the NBT material with improved ionic conductivity using newly gained materials understanding. We first investigated the phase stability and O diffusion mechanism of the NBT material using first principles calculations. On the basis of new understanding about this NBT material, we leveraged the first principles calculations to examine a large number of new dopants and to identify the potential dopants that can enhance oxygen diffusion in the NBT material. As a result, new NBT compositions with good phase stability were predicted offering several fold increases in oxygen ionic conductivity. Our study demonstrated the first principles calculation approach in providing materials insights into new materials systems and in designing materials with enhanced properties.

---

[3] This chapter has been published in
X. He and Y. Mo. "Accelerated materials design of $Na_{0.5}Bi_{0.5}TiO_3$ oxygen ionic conductors based on first principles calculations." *Physical Chemistry Chemical Physics*, (2015), 17: 18035–18044.

3.2. Methods

All density functional theory (DFT) calculations in this chapter were performed using the Vienna *Ab initio* Simulation package (VASP)[77] within the projector augmented-wave approach.[78] All total energy calculations were performed using the Perdew-Burke-Ernzerhof (PBE) generalized-gradient approximation (GGA) functional.[79] The static DFT calculations were spin-polarized using the convergence parameters consistent with the *Materials Project.*[80-82]

3.2.1. Site ordering of the NBT materials

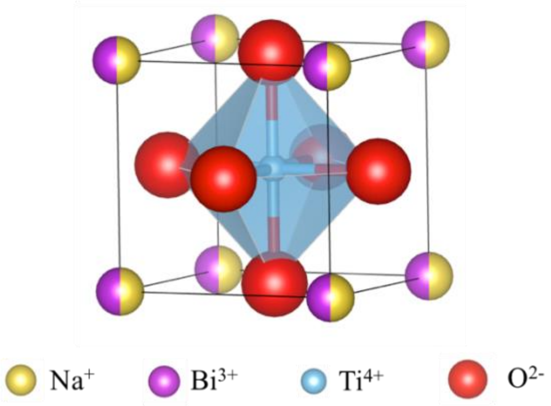

Fig. 3.1. Crystal structure of $Na_{0.5}Bi_{0.5}Ti_3O_3$. Na and Bi ions share the A sites and Ti ions occupy the B sites. The octahedral of TiO_6 is shown for clarity.

The $Na_{0.5}Bi_{0.5}TiO_3$ (NBT) material has a perovskite crystal structure ABO_3, where Na and Bi ions share the A sites with a disordered co-occupancy and Ti ions occupy the B sites (Fig. 3.1). The NBT perovskite materials have three phases, such as rhombohedral, tetragonal, and cubic phases.[83] The cubic phase is stabilized at the temperature of 520 °C or higher, and the rhombohedral phase is stabilized at the temperature of 255 °C or lower.[83] The calculations were performed on the cubic phase except for the Nudge-Elastic-Band (NEB) calculations. We used $\left(2\sqrt{2} \times 2\sqrt{2} \times 3\right)R45°$ supercell models of the NBT cubic perovskite structure, which contain 24 formula units of $Na_{0.5}Bi_{0.5}TiO_3$ and a total of 120 atoms. We first determined the A-site configurations of Na and Bi ions, which have disordered co-occupancy of the A sites in the NBT perovskite structure. We used the *pymatgen* package [84] to generate a total of 70 symmetrically distinctive structures, of which twenty were generated by minimizing the electrostatic energies of the structures and the other fifty were generated by randomizing the disordered occupancies. All these structures were statically relaxed in the DFT calculations, and the structure of the lowest DFT energy was identified as the ground state structure for other calculations.

3.2.2. Phase stability

We evaluated the phase stability of the doped NBT compositions using the scheme in ref. [85-87]. Computational phase diagram was constructed using the DFT data of all compounds in the relevant elementary spaces, e.g. Na-Bi-Ti-O, from the *Materials Project*[80,87,88] and our calculation results of the NBT compositions. The concept of 'energy above hull' defined in the previous studies[85-87,89] was used as the measure of the phase stability. The energy above hull ΔE at 0 K is the negative of the reaction energy for the NBT composition to decompose into the predicted equilibrium phases.

A positive value of ΔE suggests that the corresponding phase is not thermodynamically stable at 0 K.

To evaluate phase stability of doped NBT at non-zero temperatures, we defined the decomposition energy

$$\Delta G = \Delta E + P\Delta V - T\Delta S \tag{1}$$

at temperature T. Given the purpose of comparing the stability among solid phases, the contribution of the $P\Delta V$ term was small and was neglected as in prior studies,[85-87,89]. Given the disordering of the A-site Na/Bi cation sublattice, the A-site configurational entropy S_{config} is likely the dominant contribution to ΔS comparing to the configurational contribution of the dopants and the vibrational contribution to the entropy, which were neglected. On the basis of a random mixing of A-site Na and Bi cations at the temperatures of interests, we defined the A-site configuration entropy

$$S_{\mathrm{config}} = -k_{\mathrm{B}}(x\ln(x) + (1-x)\ln(1-x)) \tag{2}$$

where k_{B} was Boltzmann constant, and x was the partial occupancy of Na/Bi at the A sites.

3.2.3. Chemical stability

We assessed the chemical stability of the NBT materials by constructing oxygen grand potential phase diagrams. Oxygen grand potential phase diagram[85,86] provided the range of oxygen chemical potential where the NBT was thermodynamically stable. We correlated the O chemical potential to the temperature and O_2 gas partial pressure according to the following equation:

$$\mu_O(T, P_{O_2}) = \frac{1}{2}[E_{O_2} + \Delta H(T, P_{O_2}^0) - TS_{O_2}(T) + k_B T \ln(P_{O_2}/P_{O_2}^0)] - \mu_O^0 \tag{3}$$

where E_{O_2} was the DFT energy of O_2 molecules including a correction term of 1.36 eV/O_2 for the GGA errors determined by Wang *et al.*[90] We used the diatomic ideal gas enthalpy $\Delta H(T, P_{O_2}^0) = 7/2\, k_B T$ and the experimental O_2 gas entropy $S_{O_2}(T)$ at 1 atm.[91] The 1/2 term was to account for the two O atoms in the O_2 molecules. The logarithm term described the dependence of the entropy on the oxygen partial pressure based on the ideal gas approximation, where $P_{O_2}^0$ = 1 atm. In this paper, we set the reference $\mu_O^0 = \frac{1}{2} E_{O_2}$, thus $\mu_O = 0\ eV$ at 0 K.

3.2.4. Substitution and structure prediction

To investigate the Mg doped NBT material as demonstrated in the previous study,[12] the Mg doped structure, which corresponds to the composition $Na_{0.5}Bi_{0.5}Ti_{0.96}Mg_{0.04}O_{2.96}$ was generated by replacing a Ti atom with Mg and by removing an O atom from the supercell. This composition was chosen to have a similar oxygen vacancy concentration as the experimental composition $Na_{0.5}Bi_{0.49}Ti_{0.98}Mg_{0.02}O_{2.965}$. Other bivalent B^{2+} B-site substitutions, such as $Na_{0.5}Bi_{0.5}Ti_{0.96}B_{0.04}O_{2.96}$, were generated in the same way. We also considered trivalent

B^{3+} substitution for B-site Ti by adding an oxygen vacancy and replacing two Ti with B^{3+} in the supercell model, which had the composition $Na_{0.5}Bi_{0.5}Ti_{0.92}B_{0.08}O_{2.96}$. In addition, we considered A^{+} and A^{2+} substitutions for A-site Bi. The supercells of these A-site substituted structures had an oxygen vacancy and one or two Bi atoms replaced by A^{+} or A^{2+} to form the composition $Na_{0.5}A_{0.04}Bi_{0.46}TiO_{2.96}$ or $Na_{0.5}A_{0.08}Bi_{0.42}TiO_{2.96}$, respectively. The candidate dopants for the NBT material were suggested by the ionic substitution probabilistic model,[92] which was built on the data mining of all known inorganic crystal materials. We only considered the valences of the dopants that could potentially create oxygen vacancies, while some of the dopants might have multiple possible valences. The valence states of the dopants that were not energetically favorable would be screened and excluded during the phase stability calculations. The configurations of the A-site sublattice, dopants, and oxygen vacancies were determined by the computation methods described in 3.2.1, and the lowest-energy structures of the doped NBT compositions were identified. The phase stabilities of the doped compositions were calculated using the method described in 3.2.2, and the doped compounds with good phase stability were identified.

3.3. Results and discussion

3.3.1. Phase stability of the NBT material

We calculated and compared the DFT energy of all structures with different A-site Na and Bi configurations. The structure with the lowest DFT energy does not exhibit any particular ordering of Na and Bi at the A sites, and a large fraction of structures with different disordered A-site configurations have energies within a range of 20 meV/atom. We also found the structures with the ordered A-site sublattice with the rock-salt ordering or the layered ordering[93] exhibit higher DFT energies. These results indicate a disordered A-site Na/Bi sublattice in the NBT cubic perovskite structure, which is in agreement with the experimental observations.[83,94]

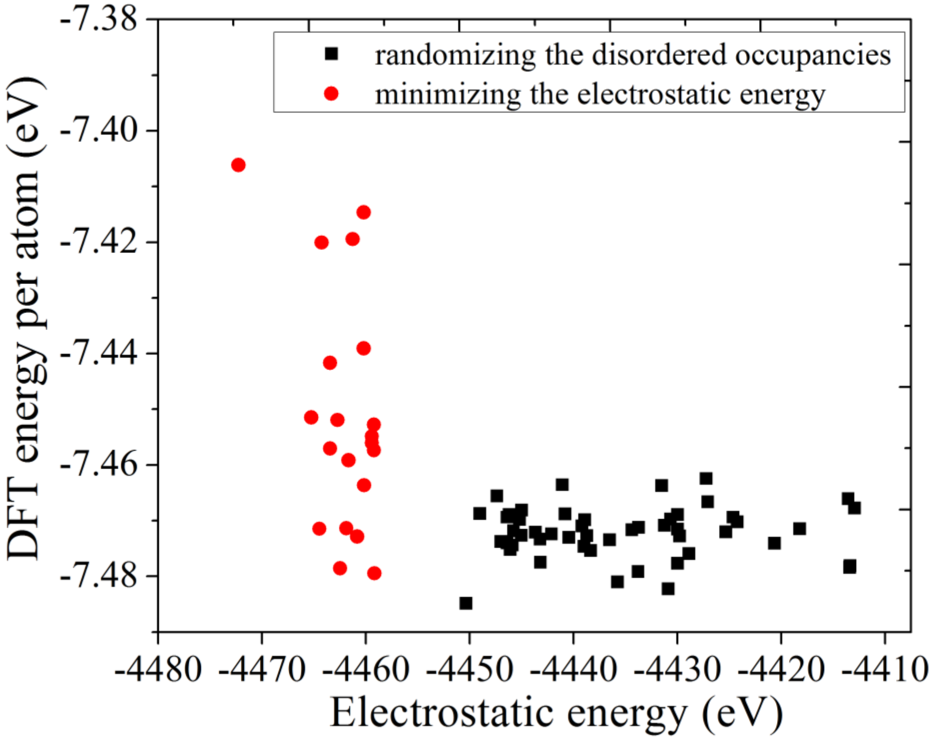

Fig. 3.2. Electrostatic energy versus DFT energy for the $Na_{0.5}Bi_{0.5}Ti_3O_3$ with different A-site configurations, which were generated by randomizing the disordered occupancies (black) and by minimizing the electrostatic energy (red) of A-site Na and Bi sublattice.

According to the phase diagram constructed using the DFT results at 0 K, the cubic NBT phase is not thermodynamically stable at 0 K and has an energy above hull ΔE of 18 meV/atom (Table 3.1). The phase equilibria of the $Na_{0.5}Bi_{0.5}TiO_3$ composition at 0 K are $Na_2Ti_6O_{13}$, $Na_4Ti_5O_{12}$ and Bi_2TiO_5. The computation predicted decomposition phase, $Na_2Ti_6O_{13}$, was observed as a secondary phase in the experiments.[94]

Our calculations show that the cubic phase is thermodynamically stable at high temperatures 1500 K (Table 3.1) after including the contribution of the configurational entropy of the A-site disordering to the free energy (section 3.2.2). Therefore, the entropy effect of the A-site disordering plays an important role in stabilizing the cubic perovskite structure of the NBT material. The computation result is consistent with the experimental observation that the NBT cubic structure is a high-temperature phase.[83]

The Mg doping introduces O vacancies in the NBT materials to achieve high oxygen conductivity.[12] We found that Mg doped compound, $Na_{0.5}Bi_{0.5}Ti_{0.96}Mg_{0.04}O_{2.96}$, exhibits a higher value of energy above hull ΔE of 23 meV/atom (Table 3.1), which is likely caused by the high formation energy of the charge-compensating oxygen vacancies. The value of ΔG is as small as 5 meV/atom at elevated temperatures, such as 1500 K, showing a reasonable phase stability of the doped compound.

Table 3.1. Phase equilibria and decomposition energies of undoped and Mg-doped NBT materials.

Composition	Phase equilibria at the composition	ΔE at 0 K (meV/atom)	ΔG at 1500 K (meV/atom)
$Na_{0.5}Bi_{0.5}TiO_3$	$Na_2Ti_6O_{13}$, $Na_4Ti_5O_{12}$, Bi_2TiO_5	18	0
$Na_{0.5}Bi_{0.5}Ti_{0.96}Mg_{0.04}O_{2.96}$	$MgTi_2O_5$, Bi_2TiO_5 , $Na_4Ti_5O_{12}$	23	5

3.3.2. Chemical stability against oxygen

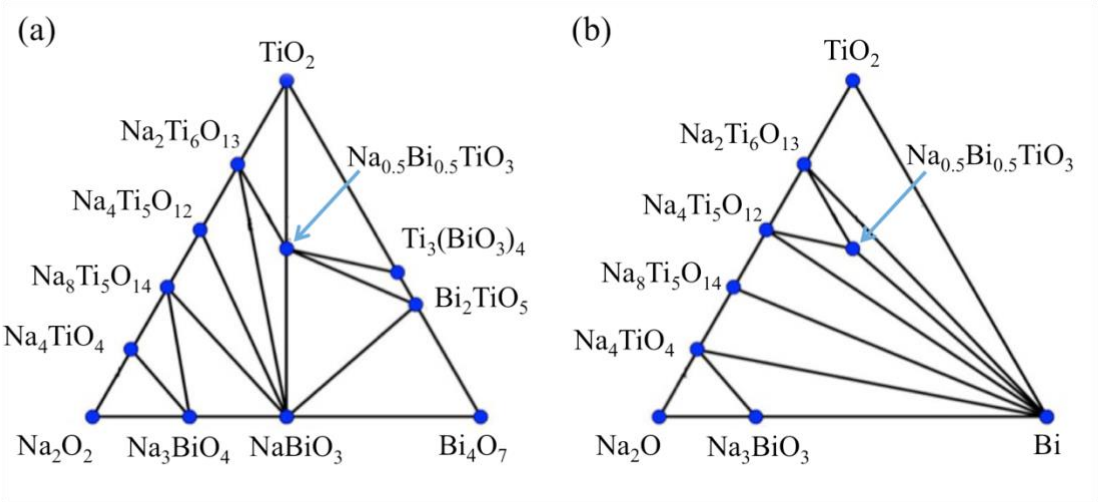

Fig. 3.3. Grand potential phase diagram of Na-Bi-Ti-O at oxygen chemical potential μ_O of (a) -0.60 eV and (b) -2.83 eV.

The chemical stability of a material against oxygen is critical for its application in electrochemical devices such as SOFCs.[10] A good solid electrolyte material in SOFCs needs to sustain the reducing and oxidizing conditions simultaneously at the anode and the cathode. Our DFT grand potential phase diagrams show that the NBT is stable in a wide range of oxygen chemical potential μ_O from –0.60 eV to –2.83 eV (μ_O = 0 eV at 0K). This chemical potential range corresponds to a pressure range from 10^{-3} to 10^{12} Pa of oxygen partial pressure at 1500 K. Our computation results are consistent with the good phase stability of the NBT material in a wide range of O_2 pressure and different chemical environments demonstrated in the experiments.[12]

In addition, we calculated the electronic structures, such as the density of states of the NBT materials (Fig. 3.4). The DFT calculation predicts a band gap of 2.3 eV for the un-doped NBT, whereas the experimental band gap is 3.26 eV.[95] The large band gap suggests poor electronic conduction in the NBT material. In addition, Mg dopants do not decrease the band gap or induce any defect states in the band gap (Fig. 3.4b). The computation results are consistent with the relatively low electronic conductivity for both undoped and Mg-doped NBT materials observed in the experiments.

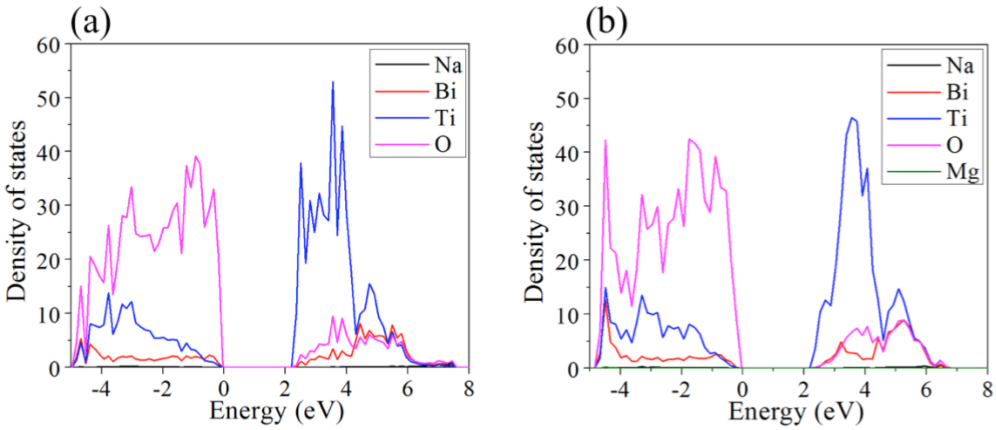

Fig. 3.4. Calculated density of states for (a) $Na_{0.5}Bi_{0.5}TiO_3$, and (b) $Na_{0.5}Bi_{0.5}Ti_{0.96}Mg_{0.04}O_{2.96}$.

3.3.3. Oxygen ion diffusion in the NBT material

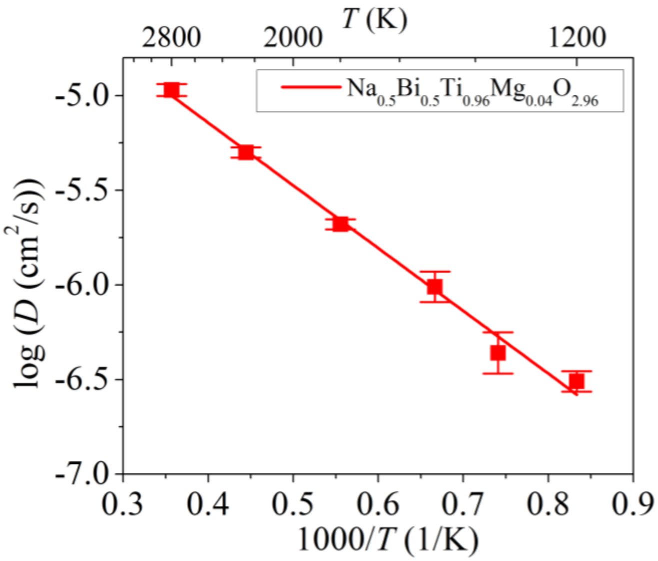

Fig. 3.5. Arrhenius-type plots of O^{2-} diffusion in the $Na_{0.5}Bi_{0.5}Ti_{0.96}Mg_{0.04}O_{2.96}$ from AIMD simulations.

Fast oxygen ion diffusions have been observed in the AIMD simulations of $Na_{0.5}Bi_{0.5}Ti_{0.96}Mg_{0.04}O_{2.96}$. The O^{2-} diffusivity at different temperatures from 1200 K to 2800 K follows an Arrhenius-type relationship (Fig. 3.5) with an activation energy of 0.61 eV, which is within the range of experimental values from 0.37 to 0.88 eV and is slightly higher than the experimental value of 0.37-0.50 eV for the cubic phase. The extrapolated oxygen diffusivity and conductivity at 900 K is 2.1×10^{-8} cm²/s and 8×10^{-3} S/cm, respectively, from the AIMD simulations (Table 3.2). The AIMD simulation results are in good agreement with the experimental diffusivity of 1.17×10^{-8} cm²/s at

905 K measured by the tracer diffusion experiments and the ionic conductivity of 8×10^{-3} S/cm measured by impedance spectroscopy at 873 K.[12] The small differences in the diffusional properties are likely caused by the different compositions used in the calculations and in the experiments. For example, comparing to our calculated compound $Na_{0.5}Bi_{0.5}Ti_{0.96}Mg_{0.04}O_{2.96}$, the $Na_{0.5}Bi_{0.49}Ti_{0.98}Mg_{0.02}O_{2.965}$ compound in the experiment has a lower Mg concentration and an additional A-site off-stoichiometry, both of which lower the activation energy for O diffusion as shown later in the NEB calculations. It is worth noting that the nominal composition is reported in previous experimental study,[12] while our computation uses the exact compositions. In summary, our AIMD simulations confirms the fast O diffusion in the NBT materials and the absence of Na diffusion in agreement with the tracer diffusion experiment.[12]

Table 3.2. Calculated and experimental O^{2-} conductivity σ, diffusivity D, and activation energy E_a of Mg-doped NBT materials.

	σ at ~900 K (mS/cm)	D at ~900 K (10^{-8} cm^2/s)	E_a (eV)
AIMD simulations ($Na_{0.5}Bi_{0.5}Ti_{0.96}Mg_{0.04}O_{2.96}$)	8 ± 3	2.1 ± 0.8	0.66 ± 0.03
Experiments [12] ($Na_{0.5}Bi_{0.49}Ti_{0.98}Mg_{0.02}O_{2.965}$)	8 *	1.17 **	0.37-0.5 (>593 K) 0.84-0.88 (<593 K)

* Ionic conductivity measured by impedance spectroscopy at 600°C [12].

** Oxygen diffusivity measured by tracer diffusion experiments at 632°C [12].

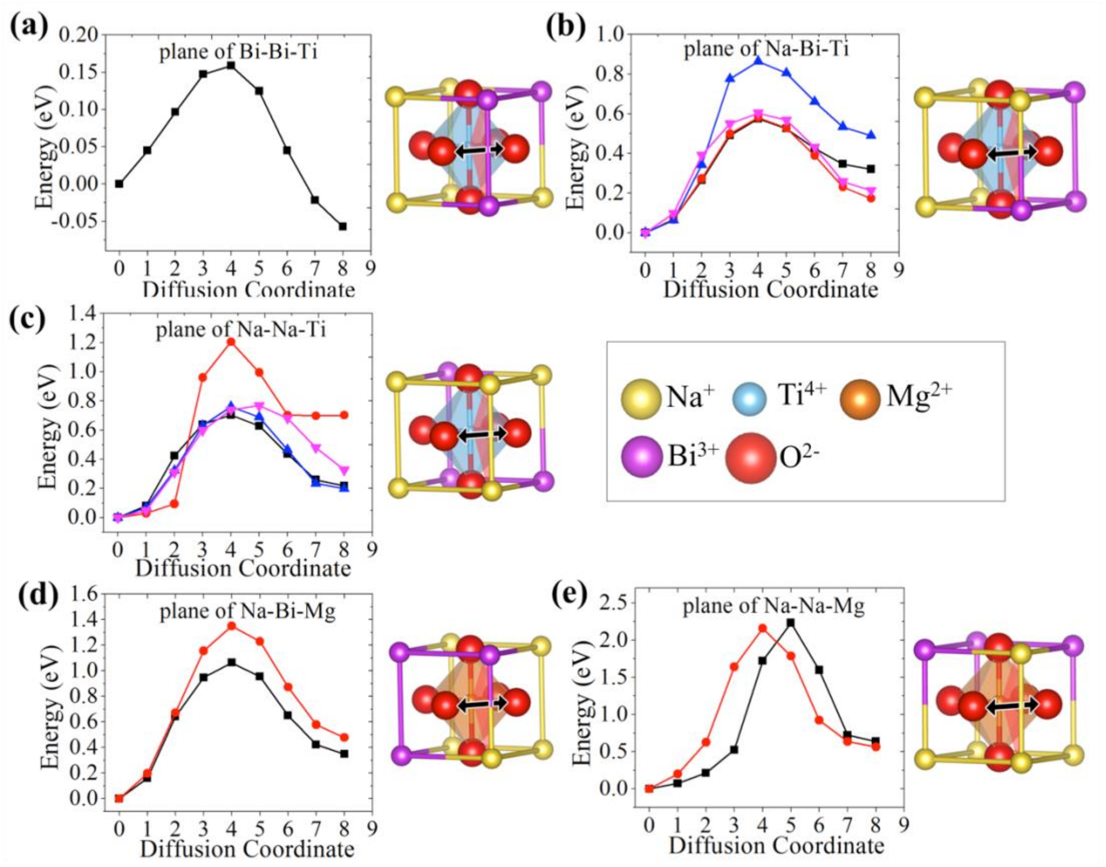

Fig. 3.6. Migration barriers for oxygen vacancies along different diffusion pathways, (a) Bi-Bi-Ti, (b) Na-Bi-Ti, (c) Na-Na-Ti (d) Na-Bi-Mg and (e) Na-Na-Mg. Each diffusion pathway (showing in different colors for clarity) is denoted by the two A-site ions and a B-site ion of the triangle. The subsets of the cubic perovskite structure on the right illustrate the atomic configuration of different pathways. The A-site ions that are not in the A-A-B triangle may vary in the actual calculations. All oxygen ions on the O sites are shown for clarity.

As observed in the AIMD simulations, the O^{2-} diffusion is mediated by oxygen vacancies migrating along the edge of the TiO_6 octahedra. This oxygen vacancy mechanisms and its diffusion pathway have been previously shown in other perovskite structures in both experiments and computation.[96-100] During the migration, an oxygen vacancy passes through a triangle comprising of two A-site ions and one B-site ion (Figure. 4). We denote the O diffusion pathway by these three atoms A-A-B in the triangle. For example, the Bi-Bi-Ti pathway represents the oxygen migration through a triangle consisting of two A-site Bi ions and one B-site Ti ion (Fig. 3.6a).

We investigated the oxygen vacancy migration along different diffusion pathways, such as Na-Bi-Ti, Na-Na-Ti, Bi-Bi-Ti, Na-Na-Mg and Na-Bi-Mg (Figure 3.6), using the Nudged Elastic Band (NEB) methods and found that the migration energy barriers are highly dependent on the different pathways. The oxygen migration along the Bi-Bi-Ti pathway has the lowest energy barrier of 0.22 eV. The Na-Bi-Ti pathway has higher migration energy barriers of 0.6 to 0.85 eV, and the Na-Na-Ti pathway has the highest barriers of 1.0 to 1.3 eV. The values of migration energy barriers vary due to the configurations of the rest of the A-site sublattice. The lower diffusion barriers at the vicinity of Bi atoms for Bi-Bi-Ti and Na-Bi-Ti pathways are likely due to high polarizability of Bi^{3+} ions caused by the $6s^2$ lone-pair electronic structure[10,14,101] In the AIMD simulations, most O^{2-} diffusion happened along the Bi-Bi-Ti and Na-Bi-Ti pathways. The oxygen migration along the Na-Bi-Ti pathway is likely the rate-limiting step in the overall oxygen diffusion, and the migration energy for the Na-Bi-Ti pathways of 0.6 eV to 0.85 eV from the NEB calculations is consistent with the activation energy of 0.61 eV from the AIMD simulations.

In addition to the significant impact of local A-site configurations on the O diffusion, the B-site dopants, such as Mg, significantly increase the migration energy barriers for O vacancies. The NEB calculations show that Na-Bi-Mg and Na-Na-Mg pathway have significantly higher migration barriers of 1.0 to 1.3 eV and of 2.1 to 2.2 eV, respectively. The higher migration barrier may be caused by the strong binding between O vacancies and Mg ions at the B sites. This higher migration barrier at the presence of Mg explains why the activation energy in the AIMD simulations is higher than those in the experiments, which were performed on the composition $Na_{0.5}Bi_{0.49}Ti_{0.98}Mg_{0.02}O_{2.965}$ with a lower Mg concentration.

3.3.4. Computational prediction of new dopants for the NBT materials

Alternative doping methods are identified to overcome the issue of Mg dopants, which are shown to increase the activation energy of oxygen diffusion. We aim to identify the doping methods that create oxygen vacancies, increase the oxygen conductivity, and in the meanwhile maintain the phase stability of the material. The substitution probability[92] predicted the following probable dopants for A-site and B-site substitutions, respectively:

B^{2+} =Zn^{2+}, Mn^{2+}, Ni^{2+}, V^{2+}, Mg^{2+}, Hg^{2+}, Co^{2+}, Yb^{2+}, Fe^{2+}, Cd^{2+}, Ca^{2+};

B^{3+}=V^{3+}, Mn^{3+}, Fe^{3+}, Ga^{3+}, Co^{3+}, Cr^{3+}, Al^{3+}, Ti^{3+};

A^+= Ag^+, Tl^+, Na^+, K^+, Li^+, Rb^+, Cu^+; and

A^{2+}=Yb^{2+}, Pb^{2+}, Sn^{2+}.

We calculated the phase stability for all doped compositions (Fig. 3.7). The decomposition energies, ΔE and ΔG, provide an indicator for the synthesizability of these doped compositions. Among the $Na_{0.5}Bi_{0.5}Ti_{0.96}B_{0.04}O_{2.96}$ and $Na_{0.5}Bi_{0.5}Ti_{0.92}B_{0.08}O_{2.96}$ generated by the aliovalent B^{2+} and B^{3+} substitution for B-site Ti, respectively (Table 3.3), the Mg doping exhibits the best phase stability (i.e. the lowest ΔG) as previously demonstrated in the experiment.[12] Other bivalent dopants, Zn, Cd, Hg, and Ni, and trivalent dopants, Fe and V, are predicted as potential dopants for B-site Ti substitution. It is worth noting that Zn and Fe doped NBT has been demonstrated in the experiments,[102,103] which confirm the predictivity of our first principles computation scheme in predicting potential dopants and in determining the phase stability of doped materials. The Ti^{3+} substitution corresponds to the reduction of B-site Ti^{4+} to Ti^{3+} with oxygen losses. The phase with oxygen loss has poorer phase stability than other doped phases with the same oxygen vacancy concentration. In addition, Fe^{3+} and V^{3+} doping gives better phase stability than their bivalent states. These results show the ability of the calculation in identifying the most energetically favorable valence states for the dopants.

The aliovalent doping of A^+ and A^{2+} for A-site Bi substitution in the composition $Na_{0.5}A_{0.04}Bi_{0.46}TiO_{2.96}$ and $Na_{0.5}A_{0.08}Bi_{0.42}TiO_{2.96}$ also maintains good phase stability (Table 3.4 and Fig. 3.7). For example, the Na and K doped compositions, $Na_{0.54}Bi_{0.46}TiO_{2.96}$ and $Na_{0.5}K_{0.04}Bi_{0.46}TiO_{2.96}$, have similar decomposition energy comparing to Mg doped $Na_{0.5}Bi_{0.5}Ti_{0.96}Mg_{0.04}O_{2.96}$. The nominal off-stoichiometry compositions, such as Bi deficiency and Na excess, in previous studies[12,15] may result in a similar effect of the Na substitution for A-site Bi. The good substitution with K is not surprising given that K and Na ions have similar chemistry, and that $K_{0.5}Bi_{0.5}TiO_3$ is known to form a solid solution with NBT.[104-106]

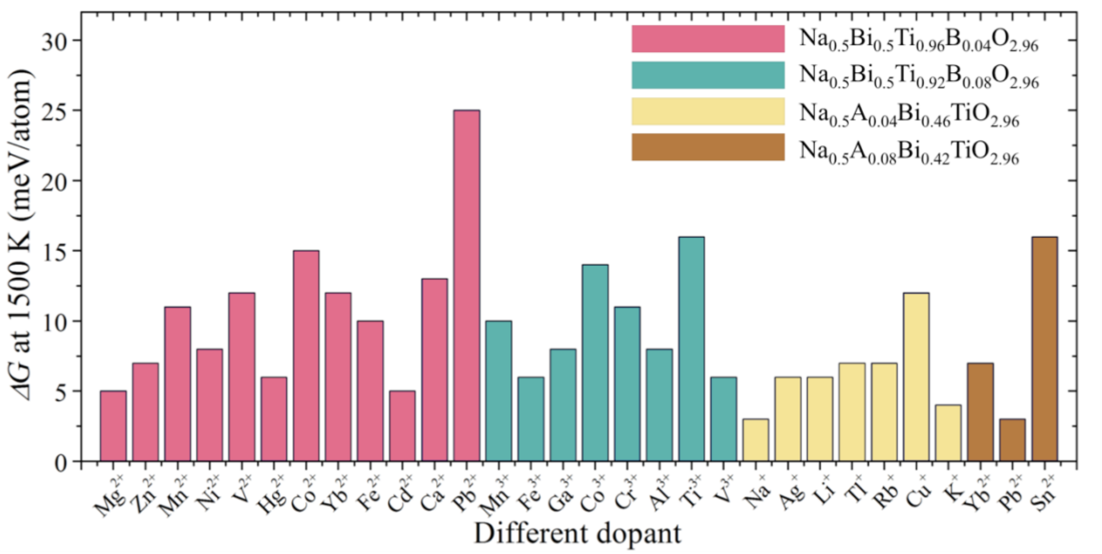

Fig. 3.7. Decomposition energies ΔG at 1500 K for the doped NBT compositions, (from left to right) $Na_{0.5}Bi_{0.5}Ti_{0.96}B_{0.04}O_{2.96}$, $Na_{0.5}Bi_{0.5}Ti_{0.92}B_{0.08}O_{2.96}$, $Na_{0.5}A_{0.04}Bi_{0.46}TiO_{2.96}$, and $Na_{0.5}A_{0.08}Bi_{0.42}TiO_{2.96}$.

Table 3.3: Phase equilibria and the decomposition energies for the NBT with B-site Ti substitution.

Dopant ion	Phase equilibria	ΔE at 0 K (meV/atom)	ΔG at 1500 K (meV/atom)
Mg^{2+}	$MgTi_2O_5$, Bi_2TiO_5, $Na_4Ti_5O_{12}$	23	5
Zn^{2+}	Bi_2TiO_5, $Na_4Ti_5O_{12}$, $Na_2Ti_6O_{13}$, ZnO	25	7
Mn^{2+}	Bi_2TiO_5, $Na_4Ti_5O_{12}$, $Na_2Ti_6O_{13}$, $MnTiO_3$	29	11
Ni^{2+}	Bi_2TiO_5, $Na_4Ti_5O_{12}$, $Na_2Ti_6O_{13}$, NiO	26	8
V^{2+}	Bi_2TiO_5, $Na_4Ti_5O_{12}$, $Na_2Ti_6O_{13}$, V_2O_3	30	12
Hg^{2+}	$Na_2Ti_6O_{13}$, Bi_2TiO_5, $Na_4Ti_5O_{12}$,HgO	24	6
Co^{2+}	Bi_2TiO_5, $Na_4Ti_5O_{12}$, $CoTi_2O_5$	33	15
Yb^{2+}	$Na_2Ti_6O_{13}$, Bi_2TiO_5, $Na_4Ti_5O_{12}$,$YbTiO_3$	30	11
Fe^{2+}	Bi_2TiO_5, $Na_4Ti_5O_{12}$, $FeTiO_5$	28	10
Cd^{2+}	Bi_2TiO_5, $Na_4Ti_5O_{12}$, $Na_2Ti_6O_{13}$, $CdTiO_3$	23	5
Ca^{2+}	Bi_2TiO_5 , $Na_4Ti_5O_{12}$, $Na_2Ti_6O_{13}$, $CaTiO_3$	31	13
Pb^{2+}	Bi_2TiO_5, $Na_4Ti_5O_{12}$, $Na_2Ti_6O_{13}$, $PbTiO_3$	43	25
V^{3+}	Bi_2TiO_5, $Na_4Ti_5O_{12}$, $Na_2Ti_6O_{13}$,V_2O_3	24	6
Mn^{3+}	Bi_2TiO_5, $Na_4Ti_5O_{12}$, $Na_2Ti_6O_{13}$, Mn_2BiO_5, Mn_3O_4	28	10
Fe^{3+}	Bi_2TiO_5, $Na_4Ti_5O_{12}$, $Na_2Ti_6O_{13}$, Fe_2O_3	24	6
Ga^{3+}	Bi_2TiO_5, $Na_4Ti_5O_{12}$, $Na_2Ti_6O_{13}$, $NaGaO_2$	26	8
Co^{3+}	Bi_2TiO_5, $Na_4Ti_5O_{12}$, $Na_2Ti_6O_{13}$, Co_3O_4, $NaCo_2O_4$	32	14
Cr^{3+}	Bi_2TiO_5, $Na_4Ti_5O_{12}$, $Na_2Ti_6O_{13}$, $NaCrO_2$	29	11
Al^{3+}	Bi_2TiO_5, $Na_4Ti_5O_{12}$, $Na_2Ti_6O_{13}$, $Al_4Bi_2O_9$	26	8
Ti^{3+}	Bi_2TiO_5, $Na_4Ti_5O_{12}$, $Na_2Ti_6O_{13}$, Bi	34	16

Table 3.4: Phase equilibria and the decomposition energies for the NBT with A-site Bi substitution.

Dopant ion	Phase equilibria	ΔE at 0 K (meV/atom)	ΔG at 1500 K (meV/atom)
Na^+	Bi_2TiO_5, $Na_4Ti_5O_{12}$, $Na_2Ti_6O_{13}$	21	3
Ag^+	Bi_2TiO_5, $Na_4Ti_5O_{12}$, $Na_2Ti_6O_{13}$, Ag_5BiO_4	24	6
Li^+	Bi_2TiO_5, $Na_4Ti_5O_{12}$, $Na_2Ti_6O_{13}$, Li_2TiO_3	24	6
Tl^+	Bi_2TiO_5, $Na_4Ti_5O_{12}$, $Na_2Ti_6O_{13}$, Tl_2TiO_3	25	7
Rb^+	Bi_2TiO_5, $Na_4Ti_5O_{12}$, $Na_2Ti_6O_{13}$, $Rb_2Ti_6O_{13}$	25	7
Cu^+	Bi_2TiO_5, $Na_4Ti_5O_{12}$, $Na_2Ti_6O_{13}$, Cu_2O	30	12
K^+	Bi_2TiO_5, $Na_4Ti_5O_{12}$, $K_2Ti_6O_{13}$, $Na_2Ti_6O_{13}$	22	4
Yb^{2+}	Bi_2TiO_5, $Na_4Ti_5O_{12}$, $Na_2Ti_6O_{13}$, $YbTiO_3$	25	7
Pb^{2+}	Bi_2TiO_5, $Na_4Ti_5O_{12}$, $Na_2Ti_6O_{13}$, $PbTiO_3$	21	3
Sn^{2+}	Bi_2TiO_5, $Na_4Ti_5O_{12}$, $Na_2Ti_6O_{13}$, $Sn_2Bi_2O_7$, Bi	34	16

Table 3.5. Diffusional properties of doped NBT materials. Error bound of the ionic conductivity is estimated based on the error bars of E_a and D obtained during the linear fitting.

Composition	E_a (eV)	σ at 900 K (mS/cm)	Error bound $[\sigma_{min}, \sigma_{max}]$ (mS/cm)
$Na_{0.5}Bi_{0.5}Ti_{0.96}Mg_{0.04}O_{2.96}$	0.66 ± 0.03	8	[5, 12]
$Na_{0.5}Bi_{0.5}Ti_{0.96}Zn_{0.04}O_{2.96}$	0.62 ± 0.06	13	[5, 31]
$Na_{0.5}Bi_{0.5}Ti_{0.96}Cd_{0.04}O_{2.96}$	0.64 ± 0.09	6	[2, 23]

$Na_{0.54}Bi_{0.46}TiO_{2.96}$	0.38 ± 0.03	30	[20, 46]
$Na_{0.5}K_{0.04}Bi_{0.46}TiO_{2.96}$	0.32 ± 0.04	96	[56, 164]

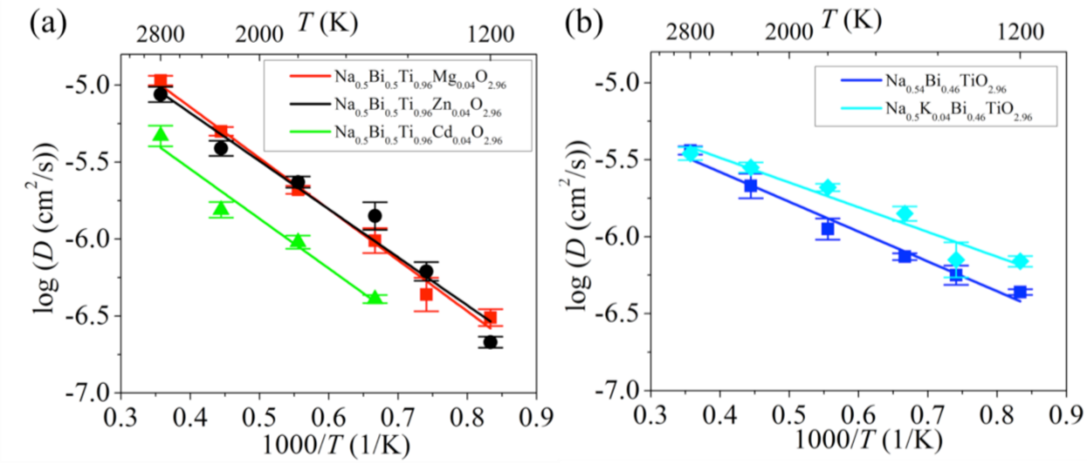

Fig. 3.8. Arrhenius-type plots of the diffusivity of (a) $Na_{0.5}Bi_{0.5}Ti_{0.96}B_{0.04}O_{2.96}$ (B=Mg, Zn, Cd) and (b) $Na_{0.54}Bi_{0.46}TiO_{2.96}$ and $Na_{0.5}K_{0.04}Bi_{0.46}TiO_{2.96}$.

The doped compounds with good phase stability were further evaluated for their oxygen diffusional properties. We performed AIMD simulations of $Na_{0.5}Bi_{0.5}Ti_{0.96}Zn_{0.04}O_{2.96}$ and $Na_{0.5}Bi_{0.5}Ti_{0.96}Cd_{0.04}O_{2.96}$ to evaluate their diffusional properties. The Zn-doped NBT shows similar O^{2-} conductivity (13 mS/cm at 900K) and activation energy (0.62 eV) comparing to Mg doping, while the Cd-doped NBT has a lower O^{2-} conductivity of 6 mS/cm at 900 K (Fig. 3.8 and Table 3.5). Therefore, Zn or Cd doping does not address the problems of Mg dopants in increasing oxygen migration barrier.

The NBT materials with A-site doping such as $Na_{0.54}Bi_{0.46}TiO_{2.96}$ and $Na_{0.5}K_{0.04}Bi_{0.46}TiO_{2.96}$ exhibit improved diffusional properties comparing to those with

B-site doping. Our AIMD simulations predict that the $Na_{0.54}Bi_{0.46}TiO_{2.96}$ compound has an activation energy of 0.38 eV and an ionic conductivity of 30 mS/cm at 900 K. The K doped compound $Na_{0.5}K_{0.04}Bi_{0.46}TiO_{2.96}$ has an even lower activation energy of 0.32 eV and the highest conductivity of 96 mS/cm at 900 K, which is an order of magnitude higher than the Mg-doped $Na_{0.5}Bi_{0.5}Ti_{0.96}Mg_{0.04}O_{2.96}$ at the same oxygen vacancy concentration. The A-site doping of the NBT material system overcomes the binding issue between O vacancies and B-site dopants (e.g. Mg) and provides a significant improvement in oxygen ionic conductivity.

3.3.5. Effect of cation sublattice ordering

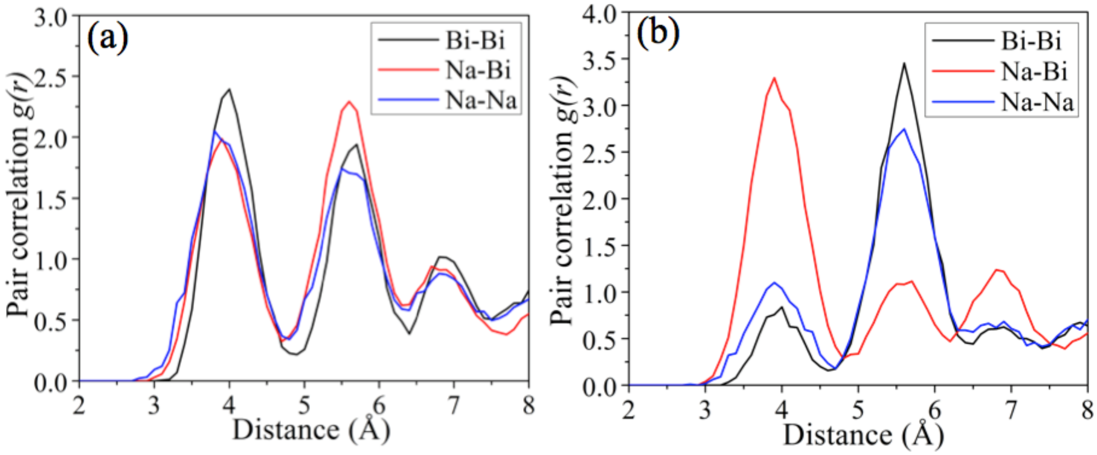

Fig. 3.9. Pair correlation function $g(r)$ of (a) a disordered A-site Na/Bi sublattice and (b) a relatively ordered A-site Na/Bi sublattice in the $Na_{0.54}Bi_{0.46}TiO_{2.96}$, respectively.

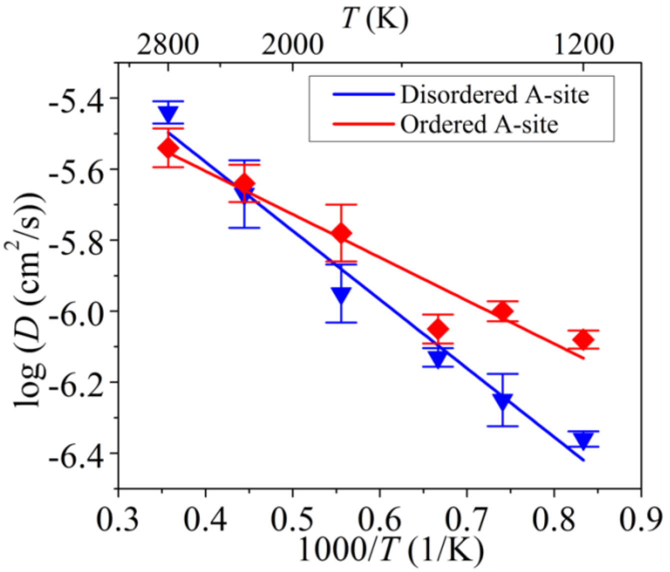

Fig. 3.10. Arrhenius-type plots of oxygen diffusivity in $Na_{0.54}Bi_{0.46}TiO_{2.96}$ with disordered (blue) and ordered (red) A-site cation sublattice.

Given that the oxygen vacancy migration energy barriers is strongly dependent on the local Na/Bi A-site configurations, the oxygen ionic conductivity in the NBT materials may depend on the specific ordering of the A-site Na/Bi cation sublattices. To investigate the ionic conductivity on the A-site ordering in the NBT, we generated a hypothetical structure of $Na_{0.54}Bi_{0.46}TiO_{2.96}$ with an A-site Na/Bi sublattice ordering that is nearly a rock-salt ordering.[93] In this rock-salt ordered A-site sublattice, most Na ions are nearest neighbors with Bi ions showing by the predominant first peak of Na-Bi at ~4 Å (Fig. 3.9b). The small occurrence of the first Na-Na and Bi-Bi peaks is due to the A-site off-stoichiometry and the symmetry incompatibility between the rock-salt ordering and the supercell lattice. The structure with the disordered Na/Bi sublattice has similar peak intensities for the Na-Bi, Na-Na, and Bi-Bi (Fig. 3.9a) nearest neighbors. This A-site disordered structure is the lowest energy structure of this composition, which has a formation energy of 27 meV/atom lower than the structure with ordered A-site sublattice.

A significant enhancement of the O^{2-} diffusion is observed in the structure with ordered A-site sublattice (Fig. 3.10). Comparing to the disordered A-site NBT, the O^{2-} conductivity extrapolated at 900 K is increased from 0.03 S/cm to 0.15 S/cm, and the activation energy is decreased from 0.38 eV to 0.24 eV (Fig. 3.10). Therefore, ordering the cation sublattice, as a potential design strategy, improves O^{2-} conductivity in the NBT materials.

3.3.6. Discussion

Our first principles computation results about the oxygen ionic conductivity, diffusivity, and activation energy of the NBT materials are in good agreement with the previous experimental report by Li *et al.*[12,15] This agreement demonstrated the validity of the computation scheme. Our computation revealed the strong dependence of the oxygen vacancy migration barrier on the nearest-neighbor cations at A sites and B sites of the perovskite structure. In particular, as a critical problem for the fast oxygen diffusion, the B-site substitution dopants, such as Mg, increase the oxygen vacancy migration barriers. According to our first principles computation results on a large number of B-site doped NBT materials, this high oxygen migration barrier is intrinsic for B-site substitutions, which bind with oxygen vacancies, and cannot be mitigated by using other dopants, such as Zn or Cd.

Our first principles computation predicted a more promising material design strategy based on the A-site substitutions to resolve the problem of the B-site substitutions. We demonstrated the A-site substitutions using a variety of dopants with reasonable phase stability in computation. In particular, the NBT compositions with the Na or K doping have shown good phase stability and high oxygen ionic conductivity. For example, the $Na_{0.54}Bi_{0.46}TiO_{2.96}$ and $Na_{0.5}K_{0.04}Bi_{0.46}TiO_{2.96}$ have similar phase stability and a significant increase in ionic conductivity, which is predicted to be 30 mS/cm and 96 mS/cm at 900K, respectively, comparing to the $Na_{0.5}Bi_{0.5}Ti_{0.96}Mg_{0.04}O_{2.96}$ at the same oxygen vacancy concentration. The improvement in the Na and K doped NBT materials is likely due to the disordered A-site sublattice of Na and Bi ions. This disordered A-site sublattice can form different local atomistic configurations to accommodate the electrostatic and strain fields of the dopants, which helps to maintain the phase stability of the doped structures and to reduce the undesired binding with B-site dopants. Our computation results of A-site doping are consistent with a recent report[15] showing the strong effects of A-site off-stoichiometry on electronic and ionic conduction, though a direct comparison between these two studies is difficult as nominal compositions were used in previous experiments.[12,15]

The computationally predicted doping methods and compositions are to be verified in experimental studies. The computational results for both phase stability and diffusional properties are based on the doped compositions with the oxygen vacancy concentration of 1.39% (one vacancy out of 72 oxygen sites). It is difficult to access lower doping concentrations, which require supercells with larger sizes. Even if the specific oxygen vacancy concentration were not achieved in the experiments, our predicted doping methods still provide correct trend for increasing ionic conductivity. In addition, we did not consider the formation of competing defects, such as planar defects, anti-site defects and segregations, in the doped compositions. Though these defects may potentially form to lower the oxygen vacancy concentration in the material, the identified phases with decent phase stability are expected to be synthesizable and to provide decent ionic conductivity.

In addition, we demonstrate the design strategy of ordering the A-site cation sublattice to increase oxygen diffusion in the NBT materials. The AIMD simulations predicted that the ordered A-site sublattice provided a higher O^{2-} conductivity and a lower activation energy. The different A-site sublattices in these two structures lead to different local pathways for O diffusion and different overall O percolation networks. The O diffusion in the structure with ordered A-site sublattice is dominated by Na-Bi-Ti diffusion pathways, while all Na-Bi-Ti, Bi-Bi-Ti, and Na-Bi-Ti pathways are present in the disordered structure. However, the poorer O^{2-} diffusion in the disordered A-site sublattice cannot be explained by the higher fraction of the low-barrier Bi-Bi-Ti diffusion pathways. We speculate that the ordered cation sublattice makes a homogenous energy land scape for oxygen migrations, where the local trapping of oxygen ions is inhibited.[107] Unfortunately, the higher formation energy of the ordered

A-site lattice may impede the realization of the NBT structures with ordered A-site sublattice.

This study demonstrated how one can use first principles calculation methods to understand the limitations in a new material system and to overcome these limitations by designing the materials. The first principles computation identified promising dopants out of all possible elements, and determined whether the doped phases are stable and whether they provide enhanced properties. The materials design capabilities rely on accurate calculations of materials properties,[37,86,87] an algorithm to predict new dopants and substitutions,[92] and an infrastructure, such as the *Materials Project*,[80] to assess the phase stability of new compounds and structures. The first principles computation design is scalable and can be performed in a highly parallel and rapid fashion to predict new materials with enhanced properties. The materials design workflow demonstrated in this study is not limited to oxygen ionic conductor materials, and can be easily transferred to other (e.g. Li^+, Na^+) ionic conductor materials.

3.4. Conclusion

In summary, we performed a first principles study of the phase stability, chemical stability, and diffusion mechanisms of the NBT oxygen ion conductor materials. The computation results were in good agreement with previous experiments[12]. Our calculations confirm that the oxygen conduction is mediated by oxygen vacancies, and that the local atomistic configurations have a significant impact on the oxygen diffusion. While the high polarizability of the Bi ions promotes fast O diffusion, the Mg dopants bind with oxygen vacancies and increase the oxygen migration barriers. This fundamental limitation of the Mg dopants motivated the first principles computational design to identify new doped NBT materials. Our first principles computation predicted that Zn and Cd dopants at B sites did not improve the oxygen ionic conductivity, and that Na and K were promising dopants to increase oxygen ionic conductivity. The newly designed NBT materials with A-site Na and K substituted A sites exhibited a many-fold increase in the ionic conductivity at 900K comparing to that in the Mg doped compound at the same oxygen vacancy concentration. This study demonstrated that the NBT material system is promising as fast oxygen ionic conductors, and that first principles computation has the ability to significantly accelerate the materials design processes.

Chapter 4: Origin of fast ion diffusion in super-ionic conductors[4]

4.1. Introduction

In this chapter, we aim to provide a general understanding about the origin of fast ionic diffusion in SIC materials beyond the classical diffusion model by considering the energy landscape of the structural framework and the mobile-ion sublattice, which have unique configurations and concentrations at super-ionic states. Specifically, we establish a simple, general conceptual framework for activating fast ion conduction with low migration barriers through materials design, which is not limited to one material system but is generally applicable.

4.2. Methods

4.2.1. Computation Methods

All density functional theory (DFT) calculations in this study were performed using Vienna *Ab initio* Simulation package (VASP)[77] within the projector augmented-wave approach. Perdew-Burke-Ernzerhof (PBE)[79] generalized-gradient approximation (GGA) functionals were adopted in all calculations. The parameters in static DFT calculations were consistent with the *Materials Project*[80-82]. The nudged

---

[4] This chapter has been published in
X. He, Y. Zhu and Y. Mo. "Origin of Fast Ion Diffusion in Super-Ionic Conductors." *Nature Communications*, (2017), 8: 15893

elastic band (NEB) calculations were performed in supercell models using *Γ*-centered 2×2×2 *k*-point grid.

4.2.2. Time correlation of Li+ dynamics

The van Hove correlation function[108] was calculated from the AIMD simulations. The distinctive part G_d describes the radial distribution of different ions after time interval Δt with respect to the initial ion,

$$G_d(r, \Delta t) = \frac{1}{4\pi r^2 N n} \left\langle \sum_{i=1}^{N} \sum_{j \neq i = 1}^{N} \delta\left(r - \left| \mathbf{r}_i(t + \Delta t) - \mathbf{r}_j(t) \right| \right) \right\rangle_t , \tag{4.1}$$

where δ is the Dirac delta function. The correlation function is averaged over the time t.

Haven ratio is often used to measure the correlation effect of ionic diffusion.[109] In this study, we defined a similar correlation factor f to quantify the correlation of ion migration:

$$f = \frac{N D_\sigma}{D} . \tag{4.2}$$

While D is the self-diffusion diffusivity of individual ions, D_σ is the diffusivity of the center of all diffusion ions and is calculated as:

$$D_\sigma = \frac{1}{2 d \Delta t} \left\langle \left| \frac{1}{N} \sum_{i=1}^{N} \mathbf{r}_i(t + \Delta t) - \frac{1}{N} \sum_{i=1}^{N} \mathbf{r}_i(t) \right|^2 \right\rangle_t . \tag{4.3}$$

4.2.3. Energy landscape of single-ion migration

The energy landscape of a single Li^+ along the migration channel (Fig. 4.3d-f) is calculated using NEB methods. In LGPS, three Li^+ in the *c* channel were removed, and the energy landscape was obtained by migrating a Li^+ across *c* channel. The energy landscape of cubic-phase LLZO corresponds to single Li^+ migration between two neighboring tetrahedral sites after removing a Li ion. The energy landscape of LATP corresponds to single Li^+ migration between two neighboring M1 sites after removing a Li ion. In the NEB calculations, the charge states of all ions were maintained by inserting extra electrons into the system as in the previous study[26]. To avoid excessive relaxation of the Li^+ sublattice, only non-Li cations and anions were relaxed during the NEB calculations.

4.2.4. Diffusion model for concerted migration

In the diffusion model illustrated in Fig. 4.4, four mobile ions were arranged in a 1D lattice consisting of two unit cells. The 1D unit cell has a period of L = 6 Å, which is similar between two nearest-neighbor M1 sites in LATP (Fig. 4.2f, 4.3f). The total energy E of the entire structure is given by the sum of the potential energy ϕ of the crystal lattice (i.e., the energy landscape) and the Coulomb interaction among mobile ions:

$$E = \sum_{i} \phi(x_i) + \sum_{i,j,i\neq j} \frac{K}{|x_i - x_j|}, \tag{4.4}$$

where x_i is the position of the ion *i*, and *K* is Coulomb interaction strength between two mobile ions. The lattice energy landscape ϕ considered in the main text (Fig. 4.6a, b) are defined as follows. The energy landscape in Fig. 4.6a is given by

$$\phi_a(x) = E_a \times \frac{\cos\theta - 0.25\cos 2\theta - C_1}{C_2}, \tag{4.5}$$

where $\theta = 2\pi x/L - \pi$, and the normalization factors $C_1 = -1.25$, $C_2 = 2.00$. The energy landscape has the highest point of $E_a = 0.6$ eV, which is set similar to the single Li-ion energy landscape of LLZO (Fig. 4.4e). The energy landscape in Fig. 4.6b is given by

$$\phi_b(x) = E_a \times \frac{\cos\theta - 1.5\cos 2\theta - C_1}{C_2}, \tag{4.6}$$

where $C_1 = -2.50$, $C_2 = 4.08$. This energy landscape has the same highest energy point of 0.6 eV, but a higher local barrier of 0.3 eV at the high-energy sites (Fig. 4.4b).

4.2.5. Materials construction

The crystal structures investigated were obtained from Inorganic Crystal Structure Database (ICSD)[110] and *Materials Project*. The structures with disordered site occupancies were ordered using the same method in the previous studies[38,111]. The structure of $Li_{1.3}Ti_{1.7}Al_{0.3}(PO_4)_3$ (LATP) was derived from $LiTi_2(PO_4)_3$ structure by partially substituting Ti with Al and by inserting extra Li atoms into M2 sites (Fig. 4.2f). The sites of Al/Ti and Li were reordered to obtain the structure.

4.3. Results and Discussion

4.3.1. Concerted ion migration in super-ionic conductors

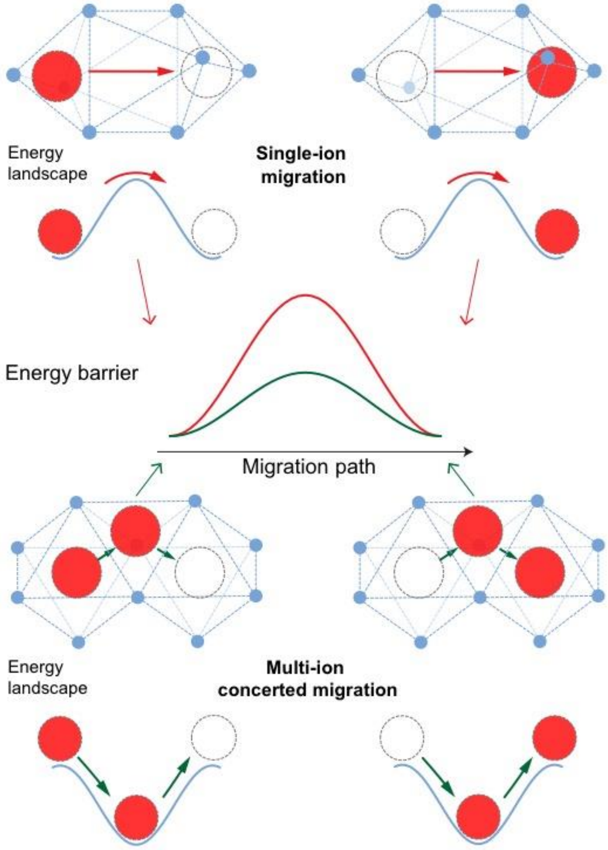

Fig. 4.1. Schematic illustration of single-ion migration versus multi-ion concerted migration. For single-ion migration (upper insets), the migration energy barrier is the same as the barrier of the energy landscape. By contrast, the concerted migration of multiple ions (lower insets) have lower energy barrier as a result of unique mobile ion configuration and strong ion-ion interactions in super-ionic conductors.

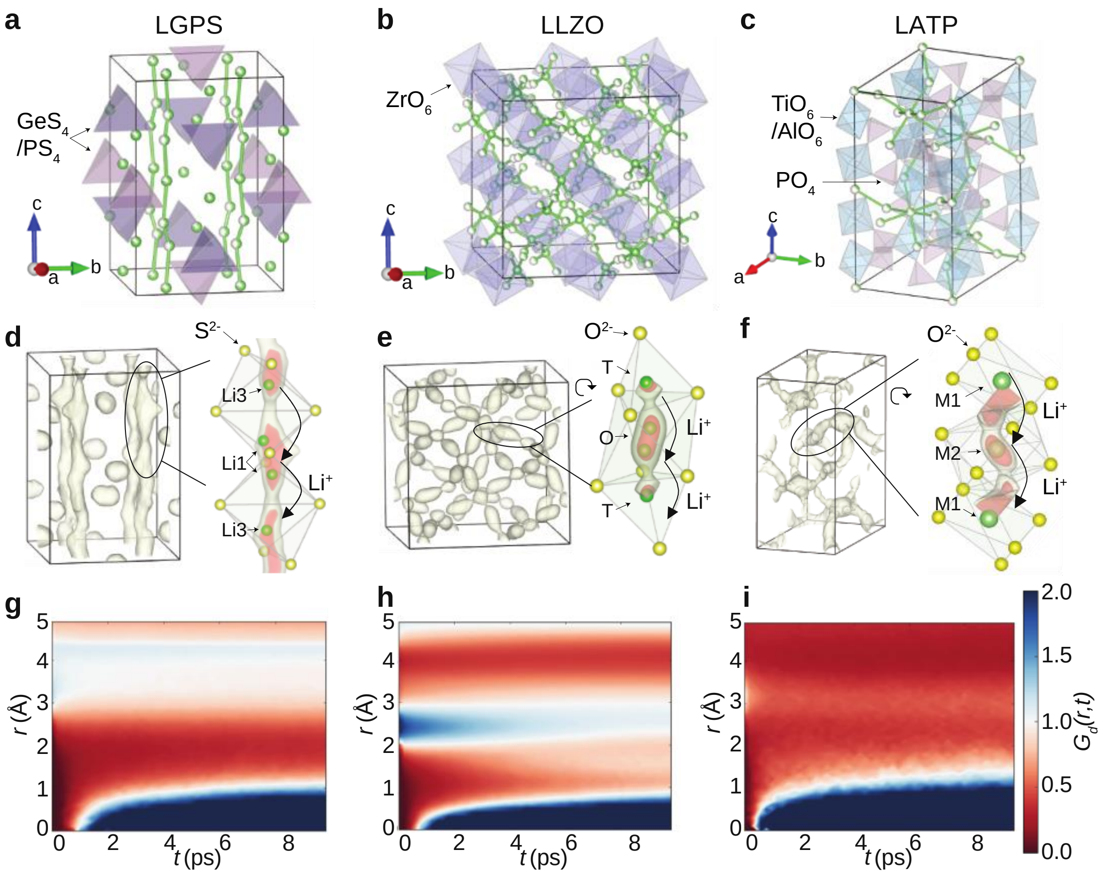

Fig. 4.2. Li ion diffusion in super-ionic conductors. a-c, Crystal structures of (**a**) LGPS, (**b**) LLZO, and (**c**) LATP marked with Li sites (partially filled green spheres), Li$^+$ diffusion channels (green bars), and polyanion groups (purple and blue polyhedra). **d-f**, The probability density of Li$^+$ spatial occupancy during AIMD simulations. The zoom-in subsets show the elongation feature of probability density along the migration channel (Li: green; O/S: yellow). The isosurfaces are $6\rho_0$, $6\rho_0$, $2\rho_0$ for LGPS, LLZO, LATP, respectively, where ρ_0 is the mean probability density in each structure and the inner isosurfaces have twice density as the outer isosurfaces. **g-i,** van Hove correlation functions of Li$^+$ dynamics on distinctive Li ions during AIMD simulations.

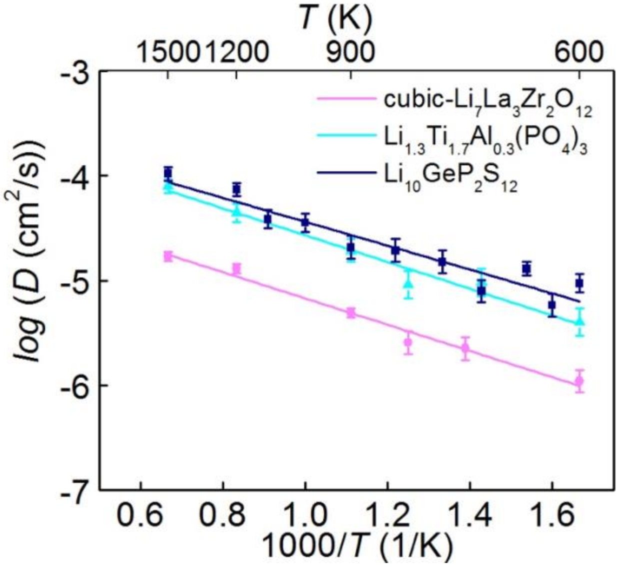

Fig. 4.3. Diffusion properties of super-ionic conductors. Arrhenius plot of Li^+ diffusivity *D* in $Li_{10}GeP_2S_{12}$, cubic-$Li_7La_3Zr_2O_{12}$, $Li_{1.3}Ti_{1.7}Al_{0.3}(PO_4)_3$ from AIMD simulations. The error bar of *D* is the statistical uncertainty from the linear fitting of mean square displacement (MSD) over time[38].

Table 4.1. Calculated (AIMD) and experimental (Expt.) Li^+ conductivity σ and activation energy E_a of $Li_{10}GeP_2S_{12}$ (LGPS), $Li_7La_3Zr_2O_{12}$ (LLZO) and $Li_{1.3}Ti_{1.7}Al_{0.3}(PO_4)_3$ (LATP). Error bound of calculated σ was estimated from the linear fitting of the Arrhenius plot (Fig. 4.3).

Composition	E_a (eV)	σ at 300 K ($mS\ cm^{-1}$)	Error bound [σ_{min}, σ_{max}] ($mS\ cm^{-1}$)
$Li_{10}GeP_2S_{12}$ (AIMD)	0.23 ± 0.03	10	[3.40, 30.65]
$Li_{10}GeP_2S_{12}$ (Expt.) [20]	0.24	12	
cubic-$Li_7La_3Zr_2O_{12}$ (AIMD)	0.25 ± 0.02	1.3	[0.47, 3.49]
cubic-$Li_7La_3Zr_2O_{12}$ (Expt.)*[22,76,112]	0.31–0.34	0.31–0.51	
$Li_{1.3}Ti_{1.7}Al_{0.3}(PO_4)_3$ (AIMD)	0.25 ± 0.03	1.1	[0.30, 4.05]
$Li_{1.3}Ti_{1.7}Al_{0.3}(PO_4)_3$ (Expt.)**[24,72,113]	0.28–0.29	0.55–5	

* Ref. [112] are based on $Li_7La_3Zr_2O_{12}$ with 1.7 wt% Sr doping

** Ref. [72,113] are based on the $Li_{1.2}Ti_{1.8}Al_{0.2}(PO_4)_3$ composition

We performed *ab initio* molecular dynamic (AIMD) simulation to study diffusion mechanism in the model SIC materials, LGPS, cubic-phase $Li_7La_3Zr_2O_{12}$ (LLZO), and $Li_{1.3}Al_{0.3}Ti_{1.7}(PO_4)_3$ (LATP) (Fig. 4.2 and 4.3), which have different anion packing (bcc in LGPS versus non-bcc in LLZO and LATP). High Li ionic conductivity and low activation energy calculated from AIMD simulations are in good agreement with those from experiments[20,22,24] (Table 4.1 and Fig. 4.3). By analyzing Li^+ dynamics from AIMD simulations, we found that most Li ions migrate in a highly concerted fashion, i.e., multiple ions hop simultaneously into their nearest sites within a few picoseconds. The van Hove correlation function (Fig. 4.2g-i) of Li^+ dynamics also confirm strong time correlation in Li^+ dynamics. In addition, we calculated the correlation factor related to Haven ratio to characterize the extent of concerted migrations. As a value of 1.0 corresponds to isolated, single ion migration, the correlation factor is calculated as 3.0, 3.0, and 2.1 for LGPS, LLZO, and LATP, respectively, in the AIMD simulations at 900 K, confirming highly concerted migration in these SICs. Therefore, the concerted migration is the dominant mechanism for fast diffusion in SICs, as observed in liquid[114,115].

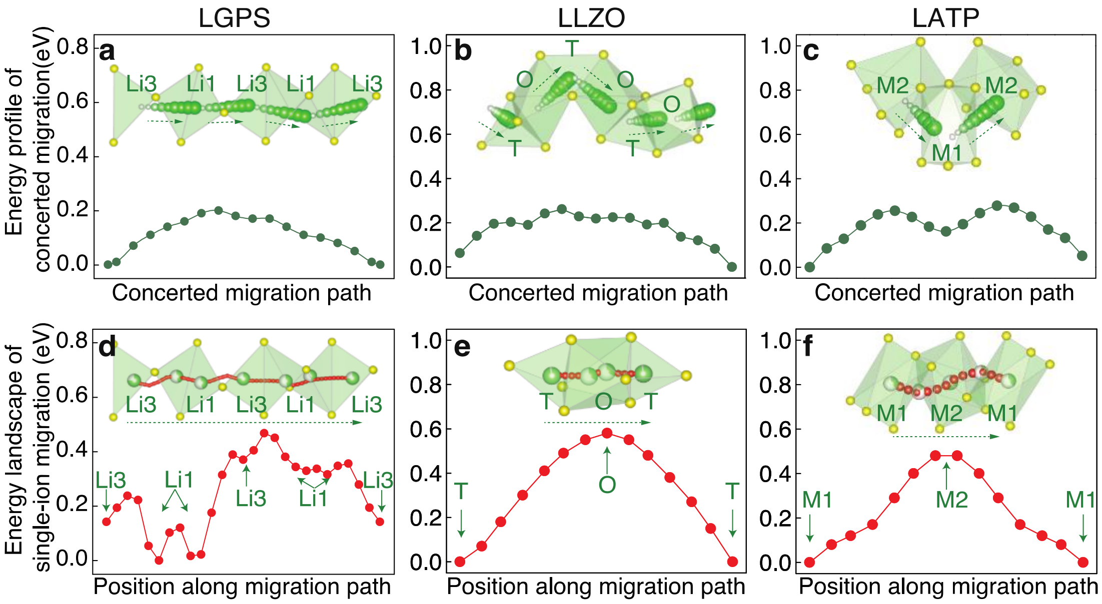

Fig. 4.4. Concerted migration and energy landscape in super-ionic conductors. a-c, Migration energy barrier in **(a)** LGPS, **(b)** LLZO, **(c)** LATP for concerted migration of multiple Li ions hopping into the next sites along the diffusion channel. Insets show the Li^+ pathway (green spheres) and O/S ions (yellow spheres). **d-f,** The energy landscape of single Li^+ along the migration channel (Inset) across multiple Li sites (partially filled green sphere) and Li^+ pathway (red spheres).

The concerted migration extracted from AIMD simulations (Fig. 4.4a-c) comprises simultaneous hopping of multiple adjacent ions into their nearest sites. Such migrations are illustrated as insets of Fig. 4.4a-c. In LGPS, a typical concerted migration mechanism involves four Li ions occupying Li1 and Li3 sites hop simultaneously along the *c* channel into their nearest-neighbor Li3 and Li1 sites, respectively (Fig. 4.4a), as observed in a previous study.[55] In LLZO, the mobile Li^+

sublattice partially co-occupy tetrahedral (T) sites and octahedral (O) sites. During concerted migration, T-site Li ions hop to the next nearest-neighbor O sites, and the Li ions occupying these O sites hop into their nearest neighbor T sites, resulting concerted hopping of multiple Li ions along the garnet diffusion channel (Fig. 4.4b) in consistency with previous modeling studies[56,57]. In LATP, two Li ions at adjacent M1 and M2 sites migrate in pair as typical concerted migration mode. The Li^+ on M1 site hops into the unoccupied M2 site, and at the same time the Li^+ on M2 site hops into the next M1 site (Fig. 4.4c). Using the NEB methods based on *ab initio* computation, the migration barriers of the concerted migration were calculated (Fig. 4.4a-c) to be 0.20, 0.26, and 0.27 eV in LGPS, LLZO, and LATP, respectively. Given the highly disordered nature of the Li sublattice, various modes of concerted migration mechanisms involving different number of Li and different Li configurations are observed during AIMD simulations. The other modes of concerted migration also show similar migration barriers as those typical modes in Fig. 4.4. The calculated energy barriers of concerted migration are in good agreement with the activation energies obtained from AIMD simulations and from the experiments[20,22,24] (Table 4.1). Therefore, these typical concerted migrations observed in AIMD simulations represent the key diffusion mechanisms in SICs.

Given such low energy barriers for multi-ion concerted migration, a relatively flat energy landscape along Li^+ diffusion channels is expected. Surprisingly, the energy landscape has barriers of 0.47, 0.58, and 0.49 eV for LGPS, LLZO, and LATP, respectively (Fig. 4.4d-f), which is significantly higher than the energy barrier of concerted migration. On the basis of classical diffusion model, these high barriers of the energy landscape would lead to even higher activation energy E_a, as each migrating ion feels the high barriers of the energy landscape along the diffusion channel. The low-barrier concerted migration of multiple ions cannot be explained by the classical diffusion model. Since these low-barrier migrations are only activated at specific composition, the mobile ion interaction and specific ion configuration, which has been neglected in classical diffusion model of single ion hopping, must be considered to properly describe the concerted migration mechanism in SICs.

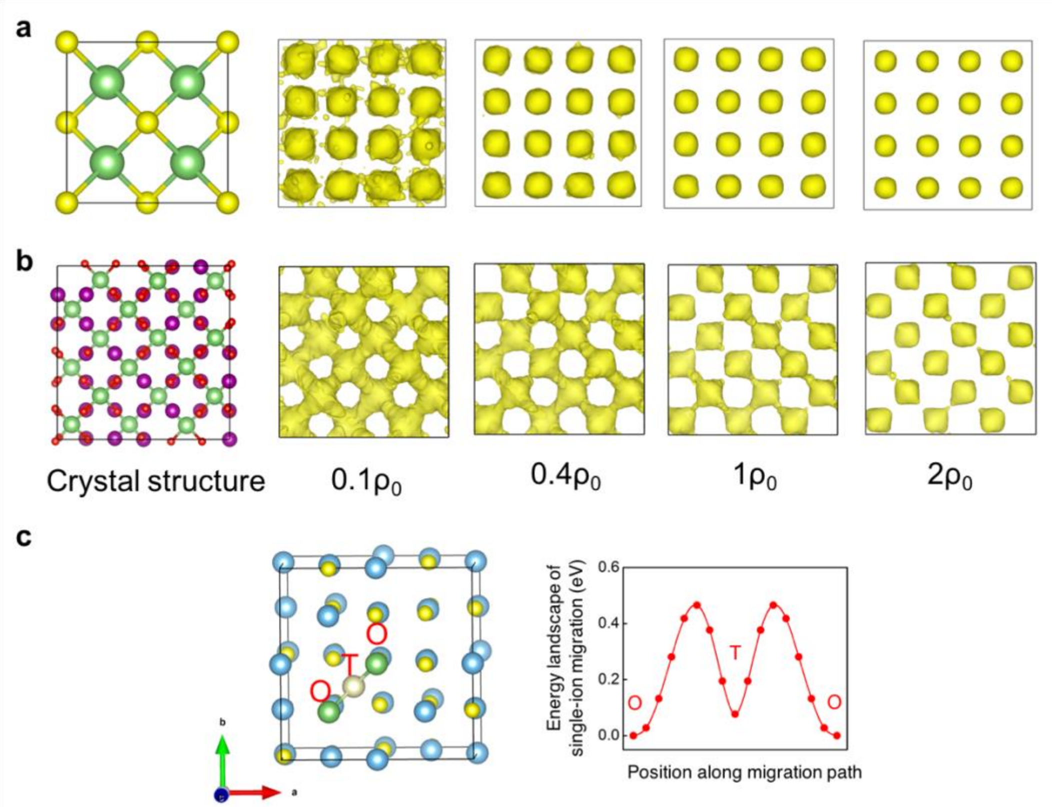

Fig. 4.5. Li ion diffusion in non-SICs. (a, b) Crystal structure (left) for (**a**) Li_2S and (**b**) $LiMn_2O_4$, and Li^+ probability densities at different isosurfaces (right), where ρ_0 is

the average probability density. **(c)** Crystal structure (left) and the energy landscape (right) of single Li^+ migration in $LiTiS_2$. Li, Mn, Ti, S and O are represented by green, purple, blue, yellow and red spheres, respectively. Octahedral (O) and tetrahedral (T) sites in $LiTiS_2$ are marked as dark and light green spheres, respectively.

4.3.2. Origin of concerted migration with low barriers

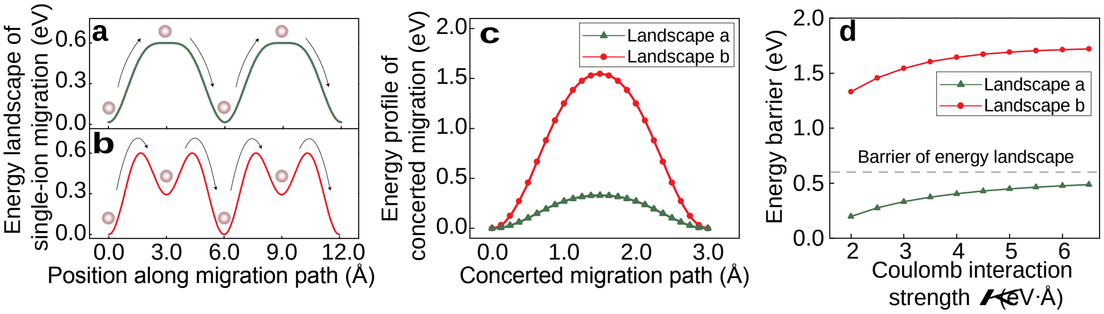

Fig. 4.6. Diffusion model for concerted migration. a, b, The potential energy of the structural framework with low (**a**) or high (**b**) barriers at the high-energy sites. The mobile ion (grey sphere) configurations and the migration paths (arrows) are illustrated. **c**, The energy profile for the concerted migration in the energy landscape (a) and (b) at $K = 3$ eV·Å. **d**, The energy barrier of concerted migration at different Coulomb interaction strength K.

Here we performed a simple diffusion model on the basis of classical diffusion model to reveal the mechanism of multi-ion concerted migration by taking into account realistic mobile ions configurations and mobile ion-ion interactions in the SICs. In the model, we chose an energy landscape (Fig. 4.6a) with a 0.6 eV barrier similar to that in LLZO (Fig. 4.4e), and include mobile ion-ion interactions with a Coulomb interaction strength K of ~2 to 4 eV·Å fitted to *ab initio* calculations. In addition, the Li^+ configuration in SIC materials (Fig. 4.4d-f) is unique. In SICs, the mobile ions occupy the high-energy sites (Fig. 4.6a, b), for example, the octahedral O sites in LLZO (Fig. 4.4e) and M2 sites in LATP (Fig. 4.4f), which are near the highest energy point along the diffusion path. At high Li concentration of these SIC materials, the high-energy sites in SICs are occupied, because the low-energy sites (e.g. tetrahedral T sites in LLZO and M1 sites in LATP) are preferably occupied and cannot accommodate all Li ions. The extra inserted ions occupying high-energy sites are stabilized by strong Coulomb interactions from nearby mobile ions (within ~2-3 Å), which also lead to the minimization of the overall lattice energy. Our model shows that such unique mobile ion configuration under strong mobile ion-ion interactions is the key for achieving low-barrier concerted migration in these SICs. At typical K values of 2-4 eV·Å in these SICs, the concerted migration of multiple ions shows significantly lower migration barrier of ~0.2-0.4 eV (Fig. 4.6d), which is in good agreement with those from NEB calculations (Fig. 4.4a-c) and AIMD simulations (Table 4.1). Therefore, this simple diffusion model captures the key physics of concerted migration. Low energy barrier of multi-ion concerted migration is a result of the unique mobile-ion configuration with high-energy site occupancy. During the concerted migration of multiple ions, the ions located at the high-energy sites are migrating downhill, which cancels out a part of energy barrier felt by other uphill-climbing ions. As a result, concerted migration of multiple ions has significantly lower energy barrier than the energy landscape of the crystal structural framework.

In addition, the energy landscape of structural framework must have high-energy sites with locally low barriers (e.g., Fig. 4.6a) for occupying ions to migrate out. The high-energy sites are associated with elongated spatial occupancy density of mobile Li ions as observed in the AIMD simulations (Fig. 4.2d-e). For example, Li probability density is elongated at the octahedral (O) sites in LLZO (Fig. 4.2e). Such elongated density indicates flat energy landscape facilitating Li^+ to hop out from these sites. Otherwise, for the energy landscape in Fig. 4b, multiple ions would simultaneously climb uphill, leading to higher energy barrier of concerted migration (Fig. 4.6c). In addition, easy migration of ions occupying high-energy sites may facilitate the onset of multi-ion concerted migration[68].

4.4. Conclusion

In summary, our theory demonstrates a simple conceptual framework for understanding fast ion diffusion in SICs. Specifically, mobile ion occupying high-energy sites can activate concerted migration with reduced migration energy barrier. In addition to the SIC behavior of lithium garnet and NASICON SICs with non-bcc anion framework, such mechanism is verified to be universal as observed in other SIC materials, such as $Li_7P_3S_{11}$, β-Li_3PS_4, LISICON, $Li_xLa_{2/3-x/3}TiO_3$ (LLTO) perovskite[66], and Na^+-conducting NASICON, where high-energy sites are occupied along the diffusion path and the concerted migration with low energy barrier is confirmed in AIMD simulations. The concerted migration of multiple ions is also reported for low-barrier diffusion in other Li ionic conductors, e.g., Li_3OX (X=Cl, Br)[116] and doped Li_3PO_4[59,117]. In addition to alkali Li^+ and Na^+ conductor, our proposed model is generally applicable to conductor of other ions. Ag super-ionic conductor, e.g., AgI[118], is known for highly concerted migration. O ionic conductors of fluorite structure (e.g. Bi_2O_3) and $La_{1-x}Ba_{1+x}GaO_{4-x/2}$[119] have also shown concerted migration behavior. Therefore, our proposed theory and identified mechanism are universally active for fast diffusion in a broad range of ionic conducting materials.

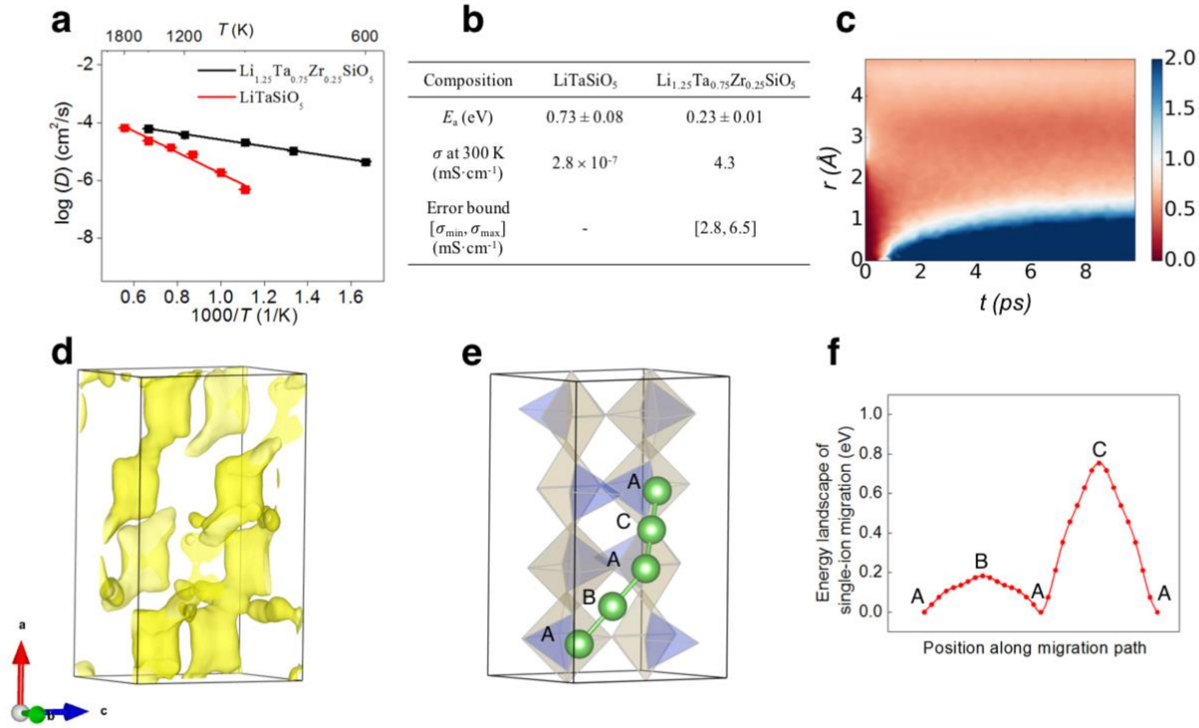

Composition	$LiTaSiO_5$	$Li_{1.25}Ta_{0.75}Zr_{0.25}SiO_5$
E_a (eV)	0.73 ± 0.08	0.23 ± 0.01
σ at 300 K (mS·cm^{-1})	2.8 × 10^{-7}	4.3
Error bound [$\sigma_{\min}$, $\sigma_{\max}$] (mS·cm^{-1})	-	[2.8, 6.5]

Fig. 4.7. Li ion diffusion in $Li_{1+x}Ta_{1-x}Zr_xSiO_5$ (x=0, 0.25). (a) Arrhenius plot of Li^+ diffusivity D in $Li_{1+x}Ta_{1-x}Zr_xSiO_5$ (x=0 and 0.25) from AIMD simulations. (b) Calculated Li^+ conductivity σ at 300 K and activity energy E_a. (c) Distinctive part of van Hove correlation function for Li^+ in $Li_{1.25}Ta_{0.75}Zr_{0.25}SiO_5$ at 900 K. (d) Li^+ probability density in $Li_{1.25}Ta_{0.75}Zr_{0.25}SiO_5$ from AIMD simulation at 900 K. The isosurface is plotted at $4\rho_0$, whereas ρ_0 is the average density. (e) Crystal structure of $LiTaSiO_5$. Li sites and MO_x (M=Ta, Si) polyhedra are colored as green, yellow and purple. High-energy B and C sites are partially occupied in doped $Li_{1.25}Ta_{0.75}Zr_{0.25}SiO_5$. (f) Energy landscape of single Li^+ migration along typical diffusion paths.

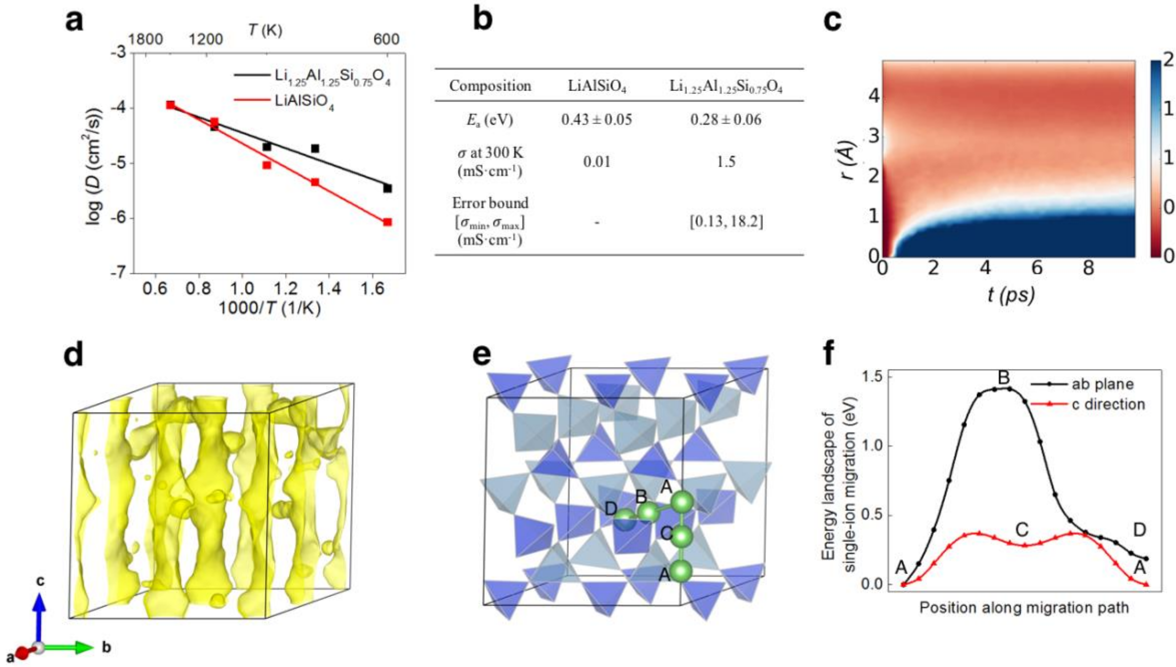

Composition	$LiAlSiO_4$	$Li_{1.25}Al_{1.25}Si_{0.75}O_4$
E_a (eV)	0.43 ± 0.05	0.28 ± 0.06
σ at 300 K (mS·cm^{-1})	0.01	1.5
Error bound $[\sigma_{min}, \sigma_{max}]$ (mS·cm^{-1})	-	[0.13, 18.2]

Fig. 4.8. Li ion diffusion in $Li_{1+x}Al_{1+x}Si_{1-x}O_4$ (x=0, 0.25). (a) Arrhenius plot of Li^+ diffusivity D in $Li_{1+x}Al_{1+x}Si_{1-x}O_4$ (x=0, 0.25) from AIMD simulations. (b) Calculated Li^+ conductivity σ at 300 K and activity energy E_a. (c) Distinctive part of van Hove correlation function for Li^+ in $Li_{1.25}Al_{1.25}Si_{0.75}O_4$ at 900 K. (d) Li^+ probability density in $Li_{1.25}Al_{1.25}Si_{0.75}O_4$ from AIMD simulation at 900 K. The isosurface is plotted at ρ_0, whereas ρ_0 is the average density. (e) $LiAlSiO_4$ crystal structure. Li sites and MO_x (M=Al, Si) polyhedra are colored as green, grey and purple. High-energy B and C sites are partially occupied in doped $Li_{1.25}Al_{1.25}Si_{0.75}O_4$. (f) Energy landscape of single Li^+ migration along typical diffusion paths.

Moreover, our theory provides a conceptually simple framework for guiding the design of super-ionic conductor materials, that is, inserting mobile ions into high-energy sites to activate concerted ion conduction with lower migration barriers. This explains how super-ionic conduction in lithium garnet and NASICON SICs is activated at certain compositions with increased Li concentration. Here, we demonstrate this strategy by designing a number of novel fast ion conducting materials to activate concerted migration with reduced diffusion barrier. We select $LiTaSiO_5$ and $LiAlSiO_4$ whose structures have decent bottleneck size of diffusion channels and well-connected Li^+ percolation network but have not been studied for Li^+ transport. The original structures show low Li^+ conductivity and high activation energy similar to their high-barrier energy landscape (Fig. 4.7-4.8). Extra Li ions are inserted into the high-energy sites of $LiTaSiO_5$ and $LiAlSiO_4$ by aliovalent substitution of non-Li cations with lower valences. In the doped materials, AIMD simulations show Li^+ concerted migrations with significantly reduced migration barrier of 0.23-0.28 eV and Li^+ conductivity of 1-4 mS/cm at RT (Fig. 4.7-4.8) comparable to many well-known Li SICs. Therefore, the design strategy based on our simple conceptual framework is demonstrated for designing novel fast ion conducting materials. Such strategy for facilitating diffusion is universal and can be generally applied to any ion conducting materials.

Chapter 5: Lithium super-ionic conductors discovery with high-throughput screening

5.1. Introduction

Super-ionic conductors (SIC) are critical for a broad range of electrochemical devices, such as batteries, fuel cells and electrochemical membranes. Recently discovered solid ceramic SICs such as $Li_{10}GeP_2S_{12}$ (LGPS) and garnet-structured $Li_7La_3Zr_2O_{12}$ (LLZO) serve as solid electrolyte enabling all-solid-state-battery (SSB) technology. SSBs have demonstrated the potential to be with improved safety, higher energy density, and longer cycle life compared to commercial lithium ion batteries with liquid electrolytes. Despite significant research efforts, SICs are rare among known solid materials. Therefore, there is significant research interest in understanding the structural characteristics that facilitate superionic conducting properties. Understanding and quantifying these structure-property relationships will motivate the discovery and development of novel SICs.

In fast ion conductors, Li ions migrate in the structural framework of the material, which consists of non-Li cations and anions. The structural framework and Li ion sublattice are known to significantly impact the Li ion diffusion within the material in several ways. An open structural framework with decent-width channels which allow Li percolation is important. In addition, an appropriate Li concentration coupled with a disordered Li sublattice generates a high carrier concentration in the material, which is also critical for high ionic conductivity, as given by the Nernst-

Einstein equation. Previous analysis of anion frameworks has provided some insight into common structural characteristics of SICs. Ceder and co-workers found that the materials with a body center cubic (bcc) anion sublattice had the lowest migration barrier.[26] This explains the SICs, LGPS and $Li_7P_3S_{11}$. This bcc anion sublattice has been successfully applied as a design principle for discovering new SICs, such as $LiZnPS_4$. While bcc anion framework provides the lowest energy landscape for Li ion migration, it is unfortunately rare among Li-containing oxides and sulfides. Other SICs such as lithium garnet and NASICON are do not have a bcc anion framework but still exhibit exceptional room temperature Li^+ conductivity. Recent work by He et al. revealed the concerted migration of multiple Li ions, as a dominant ion diffusion mechanism shared by most SICs such as LGPS, LLZO, $Li_{1.3}Al_{0.3}Ti_{1.7}(PO_4)_3$ (LATP), etc, can also exhibit low migration energy barrier in the structural framework with no bcc anion framework. He et al. showed that the unique Li ion configurations, such as high-energy site occupancy, and strong Li-Li interaction cause the canceling out effect of energy migration barrier and activate the concerted migration of multiple ions with lower energy barrier than the barrier for single ion migration.[40]

It has been an outstanding question what are the common features of the crystal structural framework of Li SICs, such as LGPS, garnet, and NASICON, etc., which have very different crystal structural frameworks. Beside the open diffusional channels, the shared structural features of these crystal structural framework are not obvious among these SICs. In addition, a quantitative description of such crystal structural features among SICs has also been lacking. For example, the bottleneck size of the crystal structural framework is known to affect migration barrier, but the optimal range of crystal bottleneck size for Li migration is yet to be identified, as the size too small or too big would both lead to high migration barrier. In addition, while short distance between Li sites is hypothesized to be a feature of SICs, it is not clear what there would be the optimal distance between Li sites. Understanding the crystal structural features shared by LGPS, LLZO, LATP, and other SICs would be critical for the future discovery of novel SICs. In particular, given the rarity of bcc anion framework, the crystal structural framework that can active concerted migration to achieve low migration barrier and disordering of Li mobile sublattice of particular importance.

This chapter aims to use computation techniques to identify such features of crystal structural framework for Li SICs, through AIMD simulations of Li diffusion within the SIC structures combined with detailed topological analyses of the crystal structural framework. From these analyses, we found unique features shared by the Li^+ spatial occupancy density and the crystal structural framework of SICs. In addition, these features of crystal structural framework are quantified. These attributes outlined the guidance for further discovery of SICs. Based on the determined attributes, we performed a high-throughput screening of all known lithium-containing oxide and sulfide compounds from inorganic crystal structure database (ICSD). Our structural framework screening uncovered all known SICs, confirming the validity of our results and approach. In addition, we also uncovered many crystal structure frameworks with potential to be fast ion conductors. For each crystal structure framework, we selected an representative compound and did aliovalent doping to modified the Li content of these structures which resulting in different Li sublattice within the structure. We found 19 SIC compounds which are predicted by AIMD simulations to have Li^+ conductivities greater than 0.1 mS/cm at 300K.

5.2. Methods

5.2.1. Ab initio Computation methods

All density functional theory (DFT) calculations in this study were performed using Vienna *Ab initio* Simulation package (VASP)[77] within the projector augmented-wave approach. Perdew-Burke-Ernzerhof (PBE)[79] generalized-gradient approximation (GGA) functionals were adopted in all calculations. The parameters in static DFT calculations were consistent with the *Materials Project*[80-82].

Ab initio molecular dynamics (AIMD) simulations were performed in supercell models using non-spin-polarized DFT calculations with a Γ-centered k-point. The time step was set to 2 fs. The initial structures were statically relaxed and were set to an initial temperature of 100 K. The structures were then heated to targeted temperatures at a constant rate by velocity scaling during 2 ps. NVT ensemble using Nosé-Hoover thermostat[120] was adopted. The total time of AIMD simulations were in the range of 100 ps to 1000 ps until the diffusivity is converged. The ionic diffusivity and conductivity were calculated following established method in previous study.[38,40,121] The probability density of mobile ions was calculated as the fraction of time that each spatial location is occupied.

5.2.2. Topological analysis of crystal structural framework

The topological analysis of crystal structural framework is performed using the Voronoi-Dirichlet partition algorithm implemented in Zeo++ [122,123]. The topological analysis is performed on the non-Li crystal structural framework (Fig. 5.2a), where all Li were removed. The crystal ionic radius is used for all ion species[124], and for sites with co-occupancy of more than one ion species, the smallest crystal ionic radius is used. All topologically accessible Voronoi void nodes are obtained by performing Voronoi-Dirichlet partition (Fig.5.2b). These Voronoi nodes correspond to the center of local space that may be occupied Li ions.

The effect of anions and non-Li cations in the crystal structural framework are also considered for determining potential Li occupancy in Voronoi nodes. Each Voronoi node has the property of void radius, which is the size of the local void space. The Voronoi nodes that are too short distance to other non-Li cations were removed as not suitable for Li-ion occupancy. The minimum cut-off distance between the Li sites and cations is 2.3 Å and 2.5 Å for oxides and sulfides, respectively. The value is determined from analysis of all Li containing oxides and sulfides compounds from Materials Project. In addition, to consider the effect of anions framework, bond valence analyses are performed on every Voronoi nodes using *pymatgen* package[84], and the Voronoi nodes of poor values of bond valence were also removed as not suitable for Li-ion occupancy (Fig.5.2c). The appropriate bond valence for potential Li sites is set to be 0.5-1.2 for oxide materials and 0.4-1.1 for sulfide materials. The cut-off values for cation distances and BV are chosen so to reproduce all experimental Li sites in Li_2O and Li_2S.

Since each Voronoi nodes represents a local space and many Voronoi nodes are nearby each other, we determined potential Li site as a collection of multiple nearby Voronoi nodes by the following steps: Firstly, we grouped the nodes to groups if the corresponding void spaces overlap with each other. Secondly, we select the potential Li sites from each group. In each group, if the maximum value of d_{ij} (d_{ij} is distance between node i and node j) is smaller than 1.8 Å, we used the center of all nodes to represent the group. In the case of larger node cluster, we selected the node by the order of large radius to small radius and make sure no any two nodes are within distance of 1.8 Å. With the potential Li sites, we divided all nodes into **node clusters** based on the distance to the potential Li sites. The size of node cluster is defined as maximum value of $r_i+r_j+d_{ij}$, (r_i, r_j are node radius of node i and j, d_{ij} is distance between node i and node j) over all pairs of nodes within the cluster. As shown in Results (5.3.1), these predicted potential Li sites agrees perfectly with the experimental Li sites, suggesting the validity of topological analysis in identifying the Li sites of crystal structure framework (Fig.5.2e.f).

To analyze connectivity among Li nodes, we determine the minimum Li-Li distance d that can connect the Li nodes to form a 3D percolated network. The smaller value of *d* suggests that the Li nodes/sites have smaller distances and can more easily form a form 3D percolated network.

5.2.3. HT screening of crystal structural framework

Table 5.1. The results of HT computation screening framework.

Screening Step	**Number of oxides compounds**	**Number of sulfides compounds**
1. All oxides/sulfides containing Li	5537	510
2. Structure checking	2878	157
3. Proper Li percolation radius	2212	114
4. Well-connected 3D Li channel	984	59
5. Large nodes cluster	704	40
6. Practical consideration	290	40
7. Unique frameworks	79	20

We performed the HT screening of crystal structural framework using our identified features. The HT screening is performed on all oxides/sulfides containing Li from ICSD database (V3.4.0, step 1 in Table 5.1). The screening step and corresponding number of compounds passed the step are summarized in the table 1. The details about the screening steps are as follow:

Structure checking (Step 2): We excluded the compounds that have any following attributes: having number of elements < 3; having number of sites > 500;

containing radioactive elements; having no/wrong oxidation states; containing water; containing disordered anion sites. For structures with sites with partial occupancy or multiple ionic species, we handled them as follows: the sites with Li partial occupancy are treated as Li sites, other sites with partial occupancy or multiple ions are treated as the ion species with the smallest radius. For example, the site shared by Ge^{4+} and P^{5+} in LGPS is treated as P^{5+}.

Proper Li percolation radius (Step 3): We excluded the compounds without decent percolation radius for the 3D diffusion network of crystal structural framework. Using topological analysis, we excluded oxides compounds with percolation radius of < 0.5 Å and sulfides with percolation radius of < 0.55 Å. These values are chosen so all known SICs can pass the screen as shown in 5.3.2.

Well-connected 3D Li channel (Step 4): We calculated the minimum linking length d that can connect Li nodes to form a 3D percolation network as shown in the 5.3.2. We excluded the compounds with $d > 3$ Å. The value is chosen so all SICs can pass the screen as shown in 5.3.2.

Practical consideration (Step 5): For practical consideration, we excluded all following compounds: ternary compounds Li-O-X, where X is S, I, Si, C, P, Al, Ge, Se, B, or Cl, which we consider to be well explored; oxide compounds containing conductive transition metal elements, such as Fe, Mn, Ni, Ti, Mo, V, or Co; oxide compounds containing N, Re, Ho, Hf, Ru, Eu, Lu; compounds in which Li share sites with other elements. The details of these compounds can be found in SI.

Doping and DFT computation of representative compounds

For each identified compound potential to be SIC, we aim to identify the doping methods that increase the Li concentration or introduce Li vacancies into the structure, and in the meanwhile maintain the phase stability of the material. For one compound, we selected one or several dopants with highest substitution probability[92] for the major cation substitution. We calculated the phase stability for all doped compositions and we rejected the compounds with poor stability ($E_{hull} > 50$ meV/atom). The doped compounds with good stability were further evaluated for their lithium diffusional properties.

Diffusion screening by AIMD simulations

From Nernst-Einstein relation and Arrhenius relation, we have the following relationship between conductivity and temperature:

$$\sigma T = \sigma_0 T_0 \exp(-\frac{E_a}{kT}), \tag{5.1}$$

where σ is conductivity, T is temperature, σ_0 and T_0 are pre-exponential factors, E_a is activation energy and k is Boltzmann constant. We only run AIMD simulations at 1150 K and 900 K, using a scheme modified from Ong et al.[125] To achieve $\sigma_{300K} > 0.1$ mS/cm, $\log(\sigma T)_{1150K}$ can be calculated from equation (5.1) to be smaller than 1.1 $\log(\sigma T)_{900K} - 0.16$, where σ is conductivity in unit of mS/cm, T is temperature in unit of K. We exclude the materials with $\sigma_{1150K} < 33$ mS/cm, which would not likely to be super-ionic at RT (assuming E_a=0.25 eV and σ_{300K} = 0.1 mS/cm) and would be have poor statistics errors in our AIMD simulations screening.

5.2.4. Doping and DFT computation of representative compounds

For each identified compound potential to be SIC, we aim to identify the doping methods that increase the Li concentration or introduce Li vacancies into the structure, and in the meanwhile maintain the phase stability of the material. For one compound, we selected one or several dopants with highest substitution probability[92] for the major cation substitution. We calculated the phase stability for all doped compositions and we rejected the compounds with poor stability (E_{hull} > 50 meV/atom). The doped compounds with good stability were further evaluated for their lithium diffusional properties.

5.2.5. Diffusion screening by AIMD simulations

From Nernst-Einstein relation and Arrhenius relation, we have the following relationship between conductivity and temperature:

$$\sigma T = \sigma_0 T_0 \exp(-\frac{E_a}{kT}),$$

where σ is conductivity, T is temperature, σ_0 and T_0 are pre-exponential factors, E_a is activation energy and k is Boltzmann constant. We only run AIMD simulations at 1150 K and 900 K, using a scheme modified from Ong et al.[125] To achieve $\sigma_{300\mathrm{K}} > 0.1$ mS/cm, $\log(\sigma T)_{1150\mathrm{K}}$ should be smaller than $1.1 \log(\sigma T)_{900\mathrm{K}} - 0.16$, where σ is conductivity in unit of mS/cm, T is temperature in unit of K. We exclude the materials with $\sigma_{1150\mathrm{K}} < 33$ mS/cm, which would not likely to be super-ionic at RT (assuming E_a=0.25 eV and $\sigma_{300\mathrm{K}} = 0.1$ mS/cm) and would be have poor statistics errors in our AIMD simulation screening.

5.3. Results and Discussion

5.3.1 Li-ion spatial occupancy density from AIMD simulations

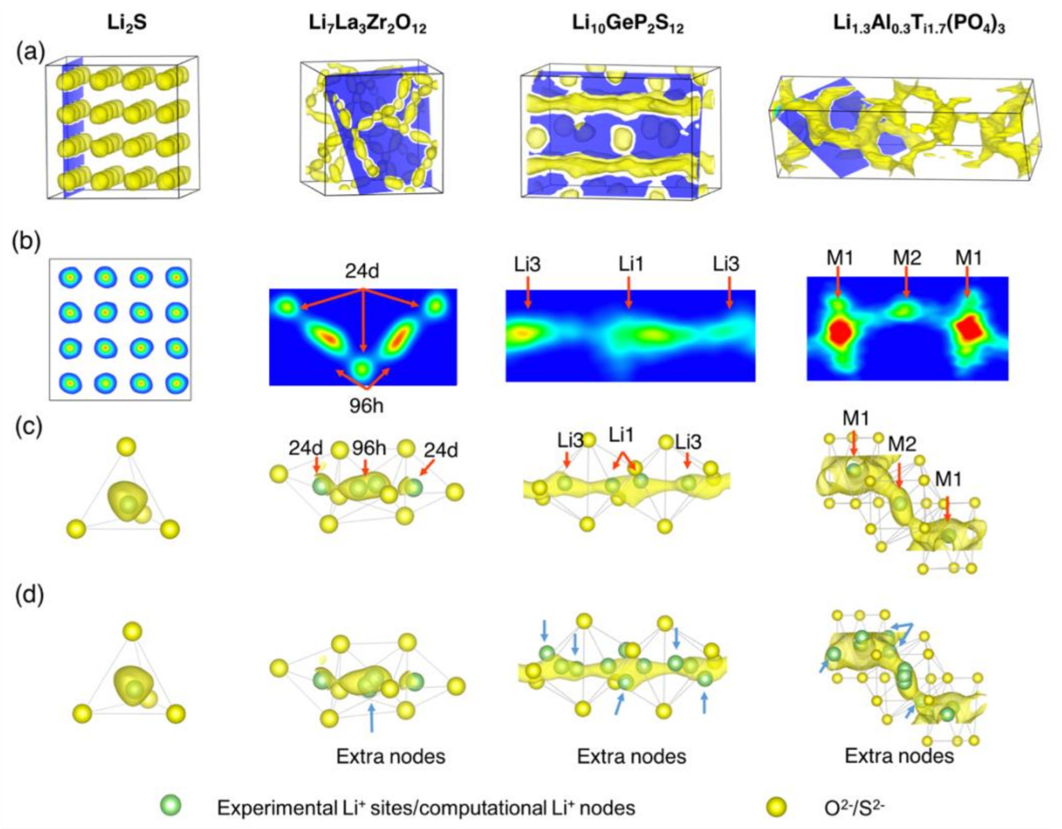

Fig. 5.1. Li ion diffusion in typical lithium containing compounds, Li_2S, LLZO, LGPS, LATP. (a) Li^+ spatial occupancy density from AIMD simulations, (b) The cross section of Li^+ spatial occupancy density as shown in (a), (c-d) Li+ spatial occupancy density with (c) experimental sites and (d) Voronoi nodes within local Li sites and diffusion channel.

A notable common feature of SIC crystal structural framework is noted from the Li^+ spatial occupancy density in the crystal structure from AIMD simulations. We noted many SICs exhibit an elongated spatial occupancy density of Li ions (Fig. 5.1). For non-SIC structures such as Li_2S, the single experimental Li site and Voronoi nodes can fully represent the local spherically symmetric occupancy density. In contrast to Li_2S, for SIC structures such as LGPS, LLZO, LATP, the local occupancy density is not necessarily spherically symmetric, such as the octahedral sites in LLZO or Li sites in LGPS and LATP. The experimental two Li 96h sites and two Li1 sites are results of the non-spherically symmetric local occupancy density. The Li^+ spatial occupancy density from AIMD simulations agrees with the nuclear density obtained from neutron diffraction analyses[126-128]. The elongated spatial occupancy density corresponds to a flat energy landscape, which can promote the Li disordering. It was speculated that the flat energy landscape corresponding to the elongated spatial occupancy density is the key for the low energy barrier concerted migration mechanism[40].

In addition, these Li^+ spatial occupancy densities coincide with the multiple partially occupied sites (Fig. 5.1). These sites are within a short Li-Li distance, where only one Li can occupy one of such sites. For example, there are two neighboring Li1 sites in LGPS with a partial occupancy of 0.466 and a short distance of 1.5 Å, and two 96h sites in LLZO with a partial occupancy of 0.35 and a short distance of 0.8 Å. These two close sites with partial occupancy may also be a crucial feature of SICs, as they indicate a flat energy landscape nearby these two sites. Therefore, as shared common features of SICs, these elongated sites are highly correlated with the elongation in Li density. Since Li sites and their potential energy surface (PES) are originated from the crystal structural framework, we then analyze the topology of the crystal structural framework.

5.3.2. Analyzing Li diffusion channel

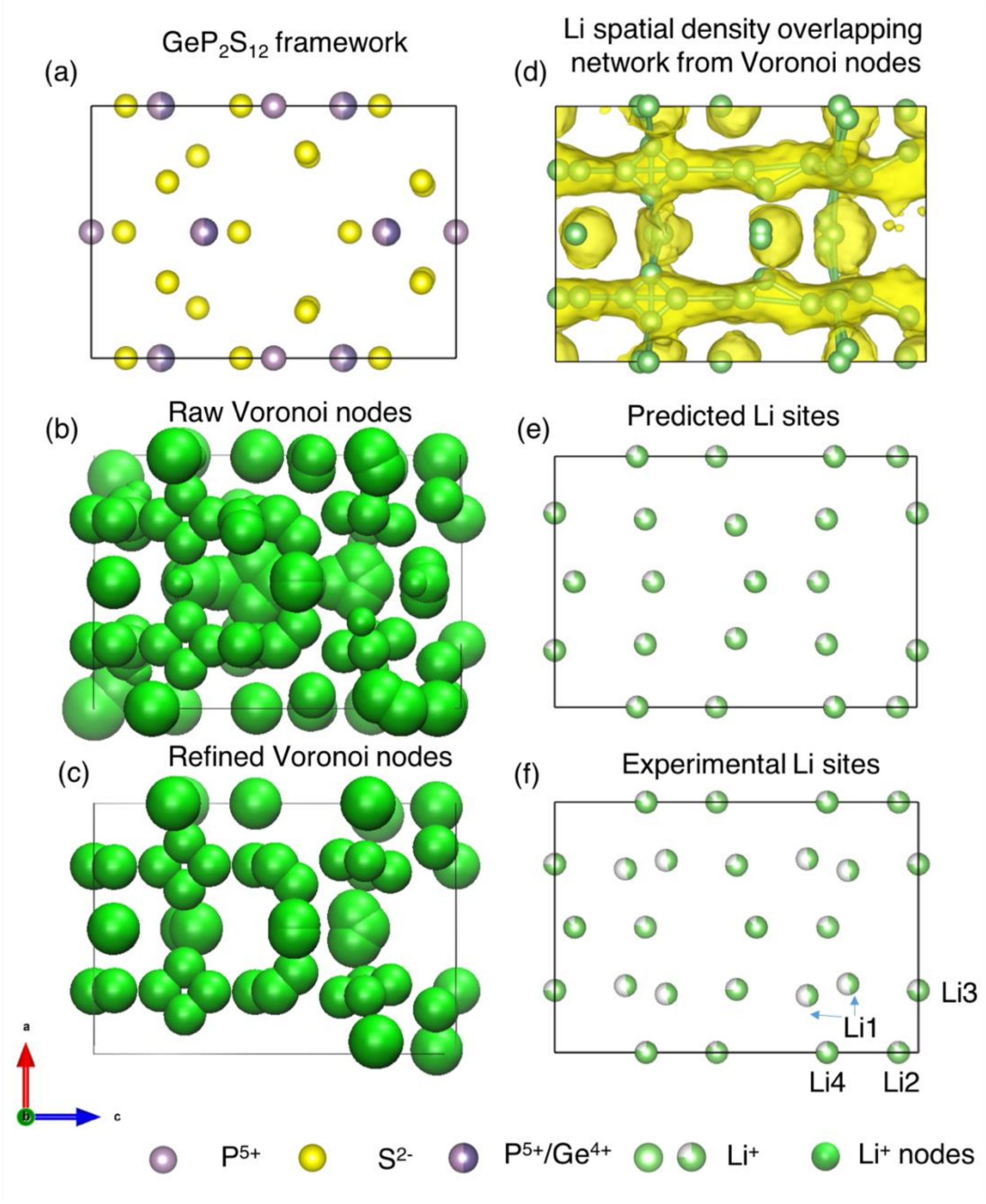

Fig. 5.2. Topological Analysis of Li sites and diffusion channels in LGPS. (a) Crystal structure of LGPS without Li. (b) All Voronoi nodes from topological

analysis on non-Li crystal structural framework. (c) Li nodes after considering the chemical environment such as BV and cation distances. (d) Li^+ spatial occupancy density from AIMD simulations in consistency with Voronoi nodes in (c), and the connection among Voronoi nodes represent the Li diffusion channels from AIMD simulations. (e) Predicted Li sites from Voronoi clusters in good agreement with (f) Experimental Li sites (Li1-Li4).

Through topological analyses, we found that Li sites characterized from the experiments can be well represented by the Voronoi nodes of the non-Li crystal structural framework. The Voronoi nodes with the proper consideration of cation and anion effects provide a very good description of the local energy landscape of Li in the crystal structural framework. For example, In LGPS as shown in Fig. 5.2, the node clusters (Fig. 5.2e) match well with the Li1-Li4 sites in LGPS (Fig. 5.2f). In consistent with previous observation, two neighboring Li1 sites can be considered as a single elongated site, since only one of the neighboring two Li1sites can be occupied at the same time. These two Li1 sites are in agreement with the multiple Li nodes clustered together, suggesting a local large and elongated space for Li occupancy with a possibly flat, low-barrier energy landscape.

The Voronoi nodes with proper chemical considerations are both approximate representations of the spatial occupancy density. For a range of SICs, we also observed the experimental sites agree well with the grouped node clusters (Fig. 5.1d). In addition, the connections among Li nodes (Fig. 5.2d) form a percolation network with a connection of 2.5A, and agree well (Fig. 5.2d) with the Li^+ spatial occupancy density, which describes the Li^+ distribution within the structure. Beside LGPS, other SIC compounds LLZO and LATP also showed the good agreement between Voronoi nodes and Li sites.

Therefore, both Li sites and Li diffusion channels in Li-ion conducting structural framework can be reproduced from the topological analysis with simple chemical considerations. The agreement between Li Voronoi nodes and experimental Li sites, and the consistency between diffusion channels from MD simulations and diffusion channels predicted by connecting the Li Voronoi nodes, demonstrate the intrinsic physical relationship between the non-Li framework structure and Li sublattice. The physical relationship allows us to identify and predict potential Li-ion conductors using the non-Li crystal structural framework as the input.

5.3.3. Criteria for good Li diffusion channels

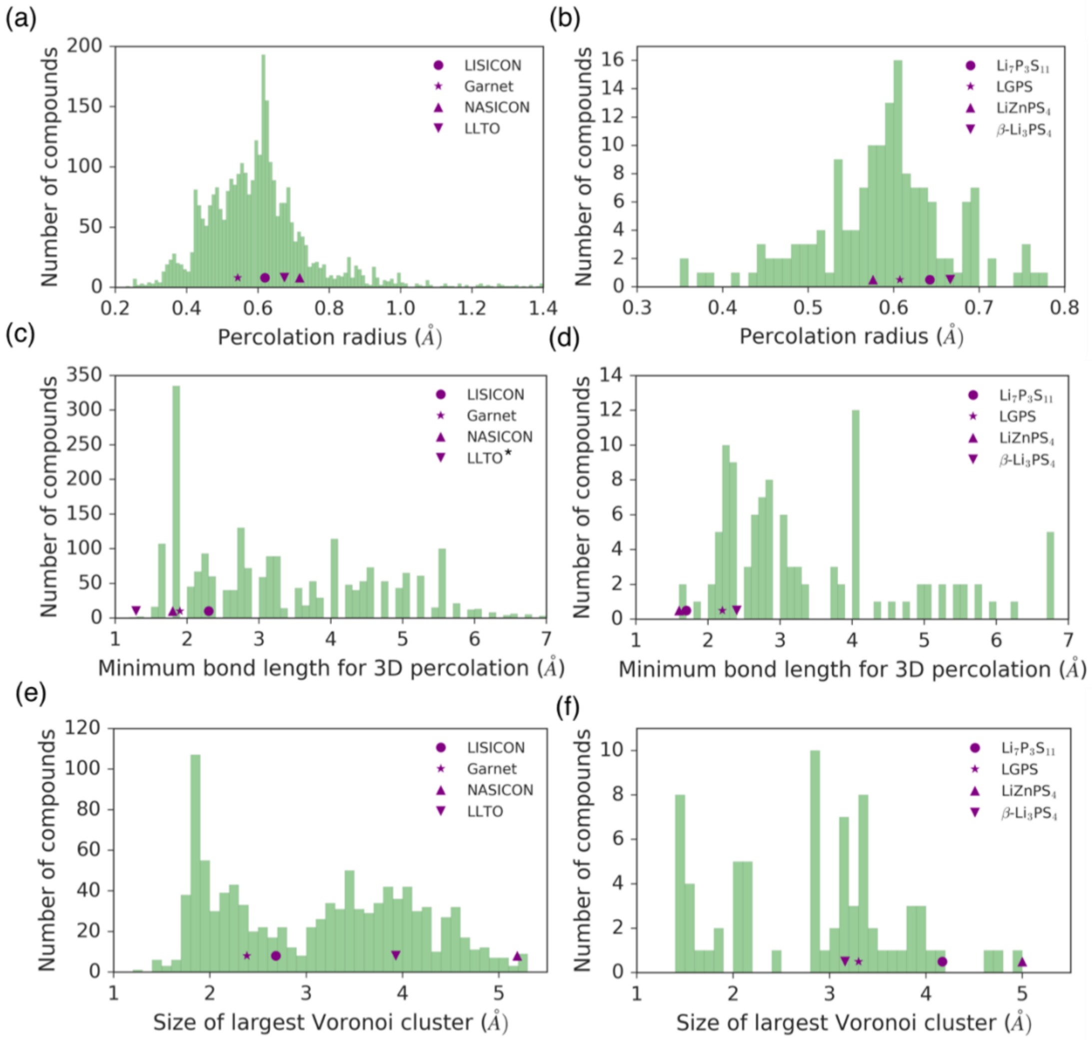

Fig. 5.3. Statistical analysis of structural features in Li-containing oxides and sulfides. (a-b) Distribution of Li percolation radius of oxides (a) and sulfides (b). (c-d) Distribution of minimum Li-Li distance for forming 3D percolation in oxides (c) and sulfides (d), *LLTO is for 2D percolation. (e-f). Distribution of the size of node cluster of all compounds with 3D percolated channel in oxides (e) and (f) sulfides.

*LLTO is with 2D percolation channel (f). Values for representative known SICs are marked in each histogram.

To identify the features of structural frameworks for SICs, here we perform topological analyses on all Li containing oxides and sulfides. It is well known that the bottleneck radius is crucial for having low energy barrier of Li migration. The Li percolation radius of all Li containing oxides and sulfides are summarized in Fig. 5.3a-b. In general, we observe that the percolation radii of known SICs fall within a narrow range (Fig. 5.3a-b). Oxide SICs have percolation radii within the small range of 0.5–0.75 Å. The percolation radii are 0.54 Å, 0.62 Å, 0.72 Å for garnet LLZO, LISICON and NASICON, respectively. For sulfides (Fig. 5.3b), the percolation radii of SICs are in the range of 0.55 Å–0.7 Å. The percolation radii are 0.58 Å, 0.61 Å 0.64 Å, 0.67 Å for $LiZnPS_4$, LGPS, $Li_7P_3S_{11}$ and β-Li_3PS_4, respectively. This observation is consistent with the common knowledge that a diffusion channel size that is too big or too small would lead to higher barrier for ion migration.

The connectivity of Li nodes, which corresponds to the Li diffusion channel, is crucial for fast ion conductors. We calculated the minimum Li-Li distance of *d* that can connect Li nodes to form a 3D percolated network. In all SIC compounds, the Li nodes form a 3D percolation network with a minimum Li-Li distance of < 3 Å. The well-connected 3D network can facilitate the ionic diffusion within the structure.

Many SICs exhibit an elongated spatial occupancy density of Li ions, as observed in Fig. 5.1 and 5.2. The elongated spatial density corresponds to a spatially large space with flat energy landscape and can be the key for the low barrier Li+

migration. We analyzed the size of the largest node cluster for all compounds with 3D percolation network (3 Å bond length). A large node cluster corresponds to a large void space of proper chemical environment within the framework. The sizes of the largest Voronoi cluster in known SICs are all larger than 2.2 Å. For example, the size of largest node cluster is 2.4 Å, 2.7 Å, 3.3 Å, 4.5 Å and 5.2 Å for LLZO, LISICON, LGPS, β-Li_3PS_4 and $LiZnPS_4$. The infinite size for NASICON and $Li_7P_3S_{11}$ are due to the periodic boundary condition. Such large void space is necessary for the elongated spacial occupancy density.

5.3.4. High Throughput screening of crystal structural framework

Since we demonstrated the topological analyses of crystal structural framework is effective in determining Li sites and diffusion channels, we then use the same topological analyses with these identified criteria of structural features, such as the percolation radius, minimum Li-Li length for 3D percolation, and size of node clusters (values as identified in 5.3.3), to screen for new crystal structural framework with potential to be good Li-ion conductors. In our HT screening, we analyze all lithium containing oxides (5537) and sulfides (510) from ICSD. In addition to other basic considerations in methods, The screening criteria are as follows. The structures should have Li percolation radius larger than 0.5 Å and 0.55 Å for oxides and sulfides, respectively, as determined in the section 5.3.3. In order to have well-connected 3D Li network, the structures should have minimum Li-Li distance for 3D percolation of less than 3 Å. In addition, the structure should have large node cluster with a size is > 2.2 Å, as determined in section 5.3.3. Out of 5537 oxides and 510 sulfides analyzed, 704 oxides compounds and 40 sulfides compounds passed these three structural criteria. In addition, we apply some practical consideration as described in 5.2.3, and some oxides with certain transition metal elements or in a few well-explored oxide system are excluded. Moreover, we also grouped those structural frameworks that are symmetrically similar. Finally, we obtained 81 unique oxides and 20 unique sulfides crystal structural frameworks (Table 5.2). Among them, there are 4 well-known SIC oxides groups, Garnet, NASICON, $Li_3A_2(PO_4)_3$ [129] and LISICON, and 4 known SIC sulfides, LGPS, $LiZnPS_4$, $Li_7P_3S_{11}$ and β-Li_3PS_4. We summarized the ICSD collection indexes and representative compositions for these 101 crystal structural frameworks in table 5.2.

Table 5.2. HT screening results for the crystal structural framework of potential Li-ion conductors. Compounds that pass further AIMD screening are highlighted.

	ICSD ID	**Composition**	**ICSD ID**	**Composition**	**ICSD ID**	**Composition**
Known SICs	100169	$Li_{3.4}Zn_{0.3}GeO_4$	69763	$LiGe_2(PO_4)_3$	422259	$Li_7La_3Zr_2O_{12}$
	50420	$Li_3Sc_2(PO_4)_3$	180319	Li_3PS_4	95785	$LiZnPS_4$
	188887	$Li_{10}GeP_2S_{12}$	157654	$Li_7P_3S_{11}$		
Compounds with high potential to be SICs	635	$Li_2Hg(PO_3)_4$	50612	Li_2AlBO_4	97909	$LiAlSiO_4$
	1044	Li_2WO_4	50950	$LiZnPO_4$	161763	$Li_2Ga_2GeS_6$
	1045	Li_2WO_4	51314	$LiAlB_2O_5$	**172184**	**$Li_9Ga_3P_8O_{29}$**
	1123	LiP_3PbO_9	51754	$Li_3Al(BO_3)_2$	180318	$Li_6P_2S_{7.8}$
	1411	Li_4PbO_4	55665	$LiAlSiO_4$	182033	$LiNbO_3$
	1485	Li_2TeO_4	**60948**	**$Li_3In_2(PO_4)_3$**	**192496**	**$Li_2B_3PO_8$**
	1897	$Li_2W_2O_7$	65260	KLi_4AlO_4	**200520**	**$LiPr(WO_4)_2$**
	2452	$LiTa_3O_8$	65764	$LiZnPO_4$	202116	$NaLi_3GeO_4$
	2929	**$LiAlSiO_4$**	66137	$LiAlSiO_4$	238234	Li_2FeGeS_4
	4253	$LiNd(PO_3)_4$	67535	$LiGeBO_4$	240704	$Li_{1.44}Al_{1.44}Si_{1.56}O_6$
	4317	Li_2TeO_3	67991	$Li_{14}Be_5B_{10}O_{27}$	**241234**	**$Li_3Sc(BO_3)_2$**
	8237	**Li_2ZnSiO_4**	68465	$LiGaS_2$	248343	$Li_3B(PO_4)_2$
	14235	$LiAlSi_2O_6$	68653	$Li_6Y(BO_3)_3$	250678	Li_2TeWO_6
	15395	Li_2WO_4	**71035**	**KLi_6BiO_6**	**262642**	**$Li_2In_2SiS_6$**
	15415	$LiAl(Si_2O_5)_2$	72098	Li_3AlGeO_5	279578	$Li_2Al(BO_2)_5$
	22010	$LiAlSiO_4$	73124	KLi_4NbO_5	280992	$LiTaGeO_5$
	23017	$Li_4Zn(PO_4)_2$	73150	$Li_5B_7S_{13}$	**291512**	**$NaLi_2B(PO_4)_2$**
	26451	$Li_2Te_2O_5$	73151	$Li_9B_{19}S_{33}$	**291513**	**$Na_2LiB_5(PO_7)_2$**
	26836	$Li_4SiGe_3O_{10}$	74860	$LiAl(PO_3)_4$	380104	Li_3BS_3
	30909	$Ba_2Li_3(PO_3)_7$	**78326**	**$Li_{10}Si_2PbO_{10}$**	**413371**	**Li_7NbO_6**

Table 5.2. (continued).

Compounds with high potential to be SICs	31316	$LiScO_2$	79098	$CsNa_3Li_{12}(GeO_4)_4$	415208	$LiEuPS_4$
	31941	Li_2ZrO_3	79352	$LiZnPO_4$	415336	$Li_9Nd_2(PS_4)_5$
	35250	$K_2Li_{14}Pb_3O_{14}$	79616	$SrLi(BS_2)_3$	417653	$Li_6Y_3(PS_4)_5$
	35252	$Li_8Nb_2O_9$	82277	$LiBiO_3$	418488	$Li_{24.8}P_4S_{21}Br_3$
	36475	**$Li_{2.1}W_{0.9}Nb_{0.1}O_4$**	86458	$Li_3Sc_2(PO_4)_3$	423127	$LiIn(WO_4)_2$
	37084	KLi_3PbO_4	88785	Li_2GeTeO_6	424079	$Li_2B_8SeO_{15}$
	38250	$KLi(PO_3)_2$	90849	$LiSi_2BO_6$	424834	Li_3SbS_3
	38324	KLi_3GeO_4	**91496**	**$LiScP_2O_7$**	**425763**	**$Li_4MnGe_2S_7$**
	39464	**$LiNbGeO_5$**	92708	$LiAlSiO_4$	427399	$CsLi(B_3O_5)_2$
	39648	**$LiTaSiO_5$**	**93013**	**$BaLi(B_3O_5)_3$**	429249	$Li_3AsW_7O_{25}$
	40245	Li_3BiO_3	94355	$Li_3In(BO_3)_2$	430770	$LiBi_3S_5$

5.3.5. New SIC compounds

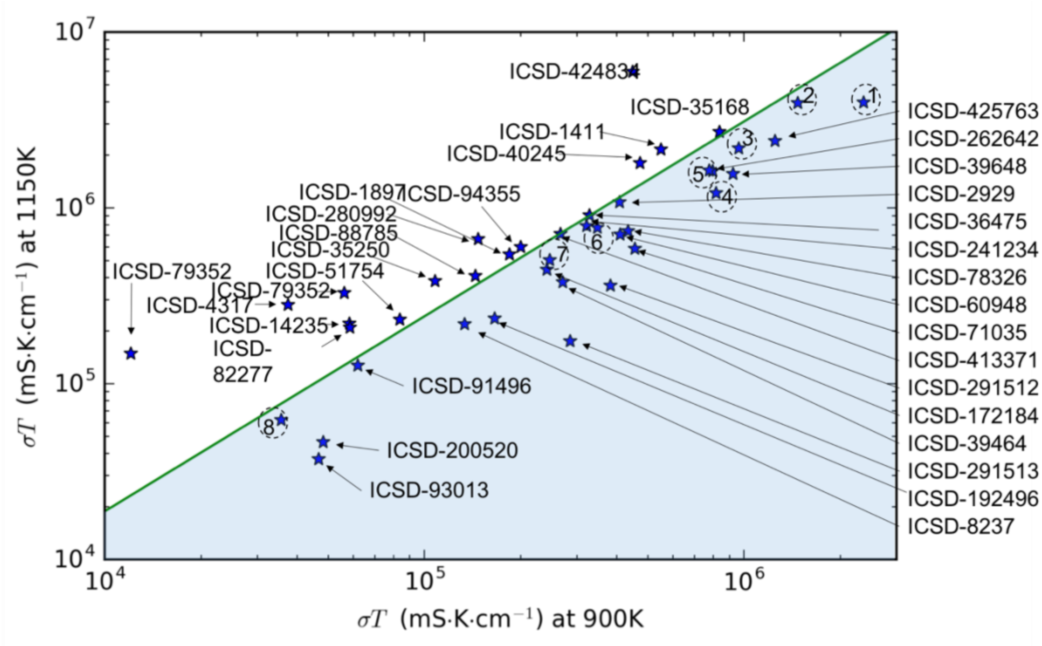

Fig. 5.4. AIMD screening. The σ *T at 900 K and 1150 K for known Li SIC and the representative compounds of new crystal structural framework in this study. The known SICs are numbered : $Li_7P_3S_{11}$ (1), β -Li_3PS_4 (2), $Li_2Zn_{0.5}PS_4$ (3), LGPS (4), LISICON (5), NASICON (6), Garnet (7), LLTO (8)

From the HT screening, we obtained 93 potential **new** SIC oxide or sulfide frameworks. For each framework, we select one representative composition. In order to activate the fast ionic diffusion within these potentially good compounds, we applied aliovalent doping to change the Li concentration. Only those doped compounds with a reasonable phase stability is further screened in AIMD simulation.

Since we have a large number of candidates, we adopted a quick diffusion estimation scheme as in previous study by Ong et al. (details in method section 5.2.5). The AIMD simulation were performed at 1150 K and 900 K to calculated the Li^+ conductivity. According to the preliminary screening scheme based on two conductivity data points, those falling within the blue region (Fig. 5.4) have the potential to have Li conductivity of > 0.1 mS/cm at 300K. All known SICs fall within the good region to be predicted to be > 0.1 mS/cm at 300K. The ability to uncover known SICs confirm that our identified features for crystal structures are effective descriptors of fast-ion conductors, and also confirm the validity of our entire structural and AIMD screening scheme. In addition, Our AIMD simulation screening found 19 candidates that are predicted to have Li+ conductivity of > 0.1 mS/cm at 300 K. These computationally predicted compounds may need further detailed computational study and experimental studies to confirm.

5.4. Conclusion

In summary, we performed a quantitative analysis of crystal frameworks for Li SICs. With the aid of AIMD simulations of Li diffusion within the SIC structures combined with detailed topological analyses of the crystal structural framework, we identified the key common feature of crystal structural framework for SICs. Based on the determined attributes, we performed a high-throughput screening of all lithium-containing oxide and sulfide compounds from ICSD. Our structural screening uncovered all known SICs, confirming the validity of our results and approach. In addition, we also uncovered many crystal structure frameworks with potential to be fast ion conductors. Through aliovalent doping, we modified the Li content of these structures which resulting in different Li sublattice within the structure and we found 19 SIC compounds which are predicted by AIMD to have Li+ conductivities greater than 0.1 mS/cm at 300K.

Chapter 6: Conclusions and Future work

6.1. Conclusions

The major conclusions of this dissertation are summarized below:

1) We re-examined the process to estimate diffusivity and ionic conductivity from the AIMD simulations and establish the procedure to minimize the fitting errors. We proposed methods for quantifying the statistical variance of the diffusivity and ionic conductivity from the number of diffusion events observed during the AIMD simulation. Our work provides the foundation for quantifying the statistical confidence levels of diffusion results from AIMD simulations and for correctly employing this powerful technique.
2) In NBT, oxygen conduction is mediated by oxygen vacancies, and that the local atomistic configurations have a significant impact on the oxygen diffusion. While the high polarizability of the Bi ions promotes fast O diffusion, the Mg dopants bind with oxygen vacancies and increase the oxygen migration barriers. Our first principles computation predicted that Na and K were promising dopants to increase oxygen ionic conductivity. The newly designed NBT materials with A-site Na and K substituted A sites exhibited a many-fold increase in the ionic conductivity at 900K comparing to that in the Mg doped compound at the same oxygen vacancy concentration.
3) We demonstrated that the concerted migration with low energy barrier is the common mechanism of fast ionic diffusion in a broad range of ionic conducting

materials. Our theory provides a conceptually simple framework for guiding the design of super-ionic conductor materials, that is, inserting mobile ions into high-energy sites to activate concerted ion conduction with lower migration barriers.

4) We demonstrated this strategy by designing a number of novel fast ion conducting materials to activate concerted migration with reduced diffusion barrier. We used aliovalent doping to convert poor Li-ion conductors, such as $LiTaSiO_5$, LiAlSiO4, into SIC materials with significantly reduced migration barrier of 0.23-0.28 eV and Li^+ conductivity of 1-4 mS/cm at RT.
5) We identified the key common feature of crystal structural framework for fast lithium ionic diffusion. Based on the determined attributes, we performed a high-throughput screening of all known lithium-containing oxide and sulfide compounds from ICSD. Our HT screening scheme uncovered many crystal structure frameworks with potential to be fast ion conductors. Through aliovalent doping, we modified the Li content of these structures which resulting in different Li sublattice within the structure and we found 17 SIC compounds which are predicted by AIMD simulations to have Li^+ conductivities greater than 0.1 mS/cm at 300K.

6.2. Future work

This dissertation demonstrates the study on atomistic diffusion process in fast ionic conductors by first principles calculations. There are many remaining research problems regarding ionic conductors. A few possible future directions are listed as follows.

The computational techniques for the design and discovery of new ionic conductor materials can be further improved. In current computational approaches, we often need to explore a large number of dopants and compositions to identify the compositions with optimal properties. Therefore, a predictive model that requires only a small computational cost to predict optimal doped compositions and their diffusional properties would greatly accelerate the design and optimization of ionic conductor materials. High-throughput computation combined with data-driven approaches may play a crucial role in quantifying composition-structure-property relationships over a broad materials space.

In addition to fast ionic diffusion, ionic conductors must simultaneously satisfy more requirements to be successfully used in ASBs. The SE need to fulfill the mechanical requirements to allow it to retain physical contact with the electrodes after repeated voltage cycling, where both electrodes undergo significant volume changes. Air and moisture stability of SEs is important for reducing manufacturing costs and for enabling solution-based processing to achieve a high loading of active electrode material. In addition, the synthesis, processing, and manufacturing of the SE must be cost-effective at a large scale.

6.3. Publications and conference presentations

Publications

1. Q. Bai, Y. Zhu, **X. He** and Y. Mo. “First principles hybrid functional study of small polarons in doped $SrCeO_3$ perovskite: towards computation design of materials with tailored polaron”. Ionics, (2018), 24, 1139-1151
2. Q. Bai, **X. He**, Y, Zhu and Y. Mo. “First Principles Study of Oxyhydride H-Ion Conductors: Toward Facile Anion Conduction in Oxide-Based Materials” ACS Applied Energy Materials, (2018), 1: 1626-1634
3. **X. He**, Y. Zhu, A. Epstein and Y. Mo. “Statistical Variances of Diffusional Properties from Ab Initio Molecular Dynamics Simulations.” NPJ Computational Materials, (2018), 4: 18.
4. **X. He**, Y. Zhu and Y. Mo. "Origin of Fast Ion Diffusion in Super-Ionic Conductors." *Nature Communications*, (2017), 8: 15893.
5. Y. Zhu, **X. He** and Y. Mo. "Strategies Based on Nitride Materials Chemistry to Stabilize Li Metal Anode." *Advanced Science*, (2017): 1600517.
6. X. Han, Y. Gong, K. K. Fu, **X. He,** G. T. Hitz, J. Dai, A. Pearse, B. Liu, H. Wang, G. Rubloff, Y. Mo, V. Thangadurai, E. D. Wachsman and L. Hu. "Negating interfacial impedance in garnet-based solid-state Li metal batteries." *Nature Materials*, (2017), 16: 572–579.
7. F. Han, Y. Zhu, **X. He,** Y. Mo and C. Wang. "Electrochemical stability of

$Li_{10}GeP_2S_{12}$ and $Li_7La_3Zr_2O_{12}$ solid electrolytes." *Advanced Energy Materials*, (2016), 6: 1501590.

8. Y. Zhu, **X. He** and Y. Mo. "First principles study on electrochemical and chemical stability of solid electrolyte–electrode interfaces in all-solid-state Li-ion batteries." *Journal of Materials Chemistry A*, (2016), 4: 3253-3266.

   Highlighted on front cover

9. **X. He** and Y. Mo. "Accelerated materials design of $Na_{0.5}Bi_{0.5}TiO_3$ oxygen ionic conductors based on first principles calculations." *Physical Chemistry Chemical Physics*, (2015), 17: 18035–18044.

10. Y. Zhu, **X. He** and Y. Mo. "Origin of Outstanding Stability in the Lithium Solid Electrolyte Materials: Insights from Thermodynamic Analyses Based on First-Principles Calculations." *ACS Appl Mater Interfaces*, (2015), 7: 23685-23693.

Presentations

1. **X. He**, Y. Zhu and Y. Mo. "Universal Design Strategy for Li Super-Ionic Conductors in All-Solid-State Li-ion Batteries : A First-Principles Study". Oral, 2017 MRS Fall Meeting & Exhibit (Nov. 26 – Dec. 1, 2017)
2. **X. He**, Y. Zhu and Y. Mo. "Universal Design Strategy for Li Super-Ionic Conductors in All-Solid-State Li-ion Batteries : A First-Principles Study". Oral, 232nd ECS Meeting (Oct. 1-6, 2017)

3. **X. He**, Y. Zhu and Y. Mo. “Facilitating Fast Ion Diffusion in Solids: Origin of Super-Ionic Conductors”. Oral, 254th ACS Meeting (Aug. 20-24, 2017)
4. **X. He** and Y. Mo. " Accelerated Materials Design of Ionic Conducting Materials based on First-Principles Calculations." Oral, APS March Meeting, Baltimore, MD, (Mar. 15-19, 2016)
5. **X. He** and Y. Mo. "Accelerated materials design of $Na_{0.5}Bi_{0.5}TiO_3$ oxygen ionic conductors based on first principles calculations." Poster Session, SSI-20, Keystone, CO, (Jun. 14-19, 2015)

Bibliography

1 Faraday, M. *Phil. Trans. R. Soc* **90** (1838).

2 Hull, S. Superionics: crystal structures and conduction processes. *Rep. Prog. Phys.* **67**, 1233–1314 (2004).

3 Sunandana, C. *Introduction to solid state ionics: phenomenology and applications*. (CRC Press, 2015).

4 Tarascon, J.-M. & Armand, M. Issues and challenges facing rechargeable lithium batteries. *Nature* **414**, 359–367 (2001).

5 Dunn, B., Kamath, H. & Tarascon, J.-M. Electrical energy storage for the grid: a battery of choices. *Science* **334**, 928–935 (2011).

6 Wachsman, E. D. & Lee, K. T. Lowering the temperature of solid oxide fuel cells. *Science* **334**, 935–939 (2011).

7 Sunarso, J. *et al.* Mixed ionic–electronic conducting (MIEC) ceramic-based membranes for oxygen separation. *J. Membr. Sci.* **320**, 13–41 (2008).

8 Xu, T. Ion exchange membranes: state of their development and perspective. *J. Membr. Sci.* **263**, 1–29 (2005).

9 Janek, J. & Zeier, W. G. A solid future for battery development. *Nat. Energy* **1**, 16141 (2016).

10 Wachsman, E. D. & Lee, K. T. Lowering the temperature of solid oxide fuel cells. *Science* **334**, 935-939 (2011).

11 Skinner, S. J. & Kilner, J. A. Oxygen ion conductors. *Materials Today* **6**, 30-37, doi:http://dx.doi.org/10.1016/S1369-7021(03)00332-8 (2003).

12 Li, M. *et al.* A family of oxide ion conductors based on the ferroelectric perovskite Na0. 5Bi0. 5TiO3. *Nat. Mater.* **13**, 31-35 (2014).

13 Haavik, C., Ottesen, E. M., Nomura, K., Kilner, J. A. & Norby, T. Temperature dependence of oxygen ion transport in Sr+Mg-substituted LaGaO3 (LSGM) with varying grain sizes. *Solid State Ionics* **174**, 233-243, doi:http://dx.doi.org/10.1016/j.ssi.2004.07.033 (2004).

14 Jung, D. W., Duncan, K. L. & Wachsman, E. D. Effect of total dopant concentration and dopant ratio on conductivity of (DyO1.5)x–(WO3)y–(BiO1.5)1−x−y. *Acta Mater.* **58**, 355-363, doi:http://dx.doi.org/10.1016/j.actamat.2009.08.072 (2010).

15 Li, M. *et al.* The dramatic influence of A-site non-stoichiometry on the electrical conductivity and conduction mechanisms in the perovskite oxide Na0.5Bi0.5TiO3. *Chem. Mater.* **27**, 629-634, doi:10.1021/cm504475k (2015).

16 Taskin, A., Lavrov, A. & Ando, Y. Achieving fast oxygen diffusion in perovskites by cation ordering. *Appl. Phys. Lett.* **86**, 091910 (2005).

17 Hermet, J., Geneste, G. & Dezanneau, G. Molecular dynamics simulations of oxygen diffusion in GdBaCo[sub 2]O[sub 5.5]. *Appl. Phys. Lett.* **97**, 174102, doi:10.1063/1.3504250 (2010).

18 Parfitt, D., Chroneos, A., Tarancón, A. & Kilner, J. A. Oxygen ion diffusion in cation ordered/disordered GdBaCo2O5+δ. *J. Mater. Chem.* **21**, 2183-2186, doi:10.1039/c0jm02924f (2011).

19 Kim, G. *et al.* Rapid oxygen ion diffusion and surface exchange kinetics in PrBaCo 2 O 5+ x with a perovskite related structure and ordered A cations. *J. Mater. Chem.* **17**, 2500-2505 (2007).

20 Kamaya, N. *et al.* A lithium superionic conductor. *Nat. Mater.* **10**, 682–686 (2011).

21 Seino, Y., Ota, T., Takada, K., Hayashi, A. & Tatsumisago, M. A sulphide lithium super ion conductor is superior to liquid ion conductors for use in rechargeable batteries. *Energy Environ. Sci.* **7**, 627–631 (2014).

22 Murugan, R., Thangadurai, V. & Weppner, W. Fast lithium ion conduction in garnet‐type Li7La3Zr2O12. *Angew. Chem. Int. Ed.* **46**, 7778‐7781 (2007).

23 Thangadurai, V., Narayanan, S. & Pinzaru, D. in *Chem. Soc. Rev.* Vol. 43 4714–4727 (2014).

24 Aono, H., Sugimoto, E., Sadaoka, Y., Imanaka, N. & Adachi, G.-y. Ionic conductivity and sinterability of lithium titanium phosphate system. *Solid State Ionics* **40/41**, 38–42 (1990).

25 Kato, Y. *et al.* High-power all-solid-state batteries using sulfide superionic conductors. *Nat. Energy* **1**, 16030 (2016).

26 Wang, Y. *et al.* Design principles for solid-state lithium superionic conductors. *Nat. Mater.* **14**, 1026–1031 (2015).

27 Allen, J. L., Wolfenstine, J., Rangasamy, E. & Sakamoto, J. Effect of substitution (Ta, Al, Ga) on the conductivity of Li7La3Zr2O12. *J. Power Sources* **206**, 315–319 (2012).

28 Li, Y., Han, J.-T., Wang, C.-A., Xie, H. & Goodenough, J. B. Optimizing Li+ conductivity in a garnet framework. *J. Mater. Chem.* **22**, 15357–15361 (2012).

29 Thangadurai, V., Kaack, H. & Weppner, W. J. F. Novel fast lithium ion conduction in garnet-type Li5La3M2O12 (M=Nb, Ta). *J. Am. Ceram. Soc.* **86**, 437–440 (2003).

30 Arbi, K., Rojo, J. M. & Sanz, J. Lithium mobility in titanium based Nasicon Li1+xTi2−xAlx(PO4)3 and LiTi2−x Zrx(PO4)3 materials followed by NMR and impedance spectroscopy. *J. Eur. Ceram. Soc.* **27**, 4215–4218 (2007).

31 Jónsson, H., Mills, G. & Jacobsen, K. W. in *Classical and quantum dynamics in condensed phase simulations* 385-404 (World Scientific, 1998).

32 Carloni, P., Rothlisberger, U. & Parrinello, M. The role and perspective of ab initio molecular dynamics in the study of biological systems. *Acc. Chem. Res.* **35**, 455–464 (2002).

33 Iftimie, R., Minary, P. & Tuckerman, M. E. Ab initio molecular dynamics: Concepts, recent developments, and future trends. *Proc. Natl. Acad. Sci. U.S.A.* **102**, 6654–6659 (2005).

34 Kirchner, B., di Dio, P. J. & Hutter, J. *Real-World Predictions from Ab Initio Molecular Dynamics Simulations*. Vol. 307 (Springer, Berlin, Heidelberg, 2011).
35 Hassanali, A. A., Cuny, J., Verdolino, V. & Parrinello, M. Aqueous solutions: state of the art in ab initio molecular dynamics. *Philosophical Transactions of the Royal Society A* **372**, 20120482 (2014).
36 Mo, Y., Ong, S. P. & Ceder, G. First Principles Study of the Li10GeP2S12 Lithium Super Ionic Conductor Material. *Chem. Mater.* **24**, 15-17 (2012).
37 Mo, Y., Ong, S. P. & Ceder, G. Insights into diffusion mechanisms in P2 layered oxide materials by first-principles calculations. *Chem. Mater.* **26**, 5208–5214 (2014).
38 He, X. & Mo, Y. Accelerated materials design of Na0.5Bi0.5TiO3 oxygen ionic conductors based on first principles calculations. *Phys. Chem. Chem. Phys.* **17**, 18035–18044 (2015).
39 Deng, Z., Mo, Y. & Ong, S. P. Computational studies of solid-state alkali conduction in rechargeable alkali-ion batteries. *NPG Asia Materials* **8**, e254 (2016).
40 He, X., Zhu, Y. & Mo, Y. Origin of Fast Ion Diffusion in Super-Ionic Conductors. *Nat. Commun.* **8**, 15893 (2017).
41 He, K. *et al.* Sodiation kinetics of metal oxide conversion electrodes: a comparative study with lithiation. *Nano Lett.* **15**, 5755-5763 (2015).
42 Mosconi, E., Azpiroz, J. M. & De Angelis, F. Ab Initio Molecular Dynamics Simulations of Methylammonium Lead Iodide Perovskite Degradation by Water. *Chem. Mater.* **27**, 4885-4892 (2015).
43 Zhang, C., Wu, J., Galli, G. & Gygi, F. Structural and Vibrational Properties of Liquid Water from van der Waals Density Functionals. *J. Chem. Theory Comput.* **7**, 3054-3061 (2011).
44 Lin, I. C., Seitsonen, A. P., Tavernelli, I. & Rothlisberger, U. Structure and Dynamics of Liquid Water from ab Initio Molecular Dynamics-Comparison of BLYP, PBE, and revPBE Density Functionals with and without van der Waals Corrections. *J. Chem. Theory Comput.* **8**, 3902-3910 (2012).
45 Thomas, M., Brehm, M., Fligg, R., Vöhringer, P. & Kirchner, B. Computing vibrational spectra from ab initio molecular dynamics. *Phys. Chem. Chem. Phys.* **15**, 6608–6622 (2013).
46 Car, R. & Parrinello, M. Structural, dynamical, and electronic properties of amorphous silicon: An ab initio molecular dynamics study. *Phys. Rev. Lett.* **60**, 204-207 (1988).
47 Kresse, G. & Hafner, J. Ab initio molecular-dynamics simulation of the liquid-metal–amorphous-semiconductor transition in germanium. *Phys. Rev. B.* **49**, 14251-14269 (1994).
48 Johari, P., Qi, Y. & Shenoy, V. B. The mixing mechanism during lithiation of Si negative electrode in Li-ion batteries: an ab initio molecular dynamics study. *Nano Lett.* **11**, 5494-5500 (2011).

49 Lee, T. & Elliott, S. Ab initio computer simulation of the early stages of crystallization: application to Ge 2 Sb 2 Te 5 phase-change materials. *Phys. Rev. Lett.* **107**, 145702 (2011).

50 Ong, S. P. *et al.* Phase stability, electrochemical stability and ionic conductivity of the Li10±1MP2X12 (M = Ge, Si, Sn, Al or P, and X = O, S or Se) family of superionic conductors. *Energy Environ. Sci.* **6**, 148–156 (2013).

51 Deng, Z., Radhakrishnan, B. & Ong, S. P. Rational Composition Optimization of the Lithium-Rich Li3OCl1-xBrxAnti-Perovskite Superionic Conductors. *Chem. Mater.* **27**, 3749−3755 (2015).

52 Zhu, Z., Chu, I.-H., Deng, Z. & Ong, S. P. Role of Na+ Interstitials and Dopants in Enhancing the Na+ Conductivity of the Cubic Na3PS4 Superionic Conductor. *Chem. Mater.* **27**, 8318-8325 (2015).

53 Ling, C., Zhang, R., Arthur, T. S. & Mizuno, F. How General is the Conversion Reaction in Mg Battery Cathode: A Case Study of the Magnesiation of α-MnO2. *Chem. Mater.* **27**, 5799-5807 (2015).

54 Ling, C. & Suto, K. Thermodynamic Origin of Irreversible Magnesium Trapping in Chevrel Phase Mo6S8: Importance of Magnesium and Vacancy Ordering. *Chem. Mater.* **29**, 3731-3739 (2017).

55 Xu, M., Ding, J. & Ma, E. One-dimensional stringlike cooperative migration of lithium ions in an ultrafast ionic conductor. *Appl. Phys. Lett.* **101**, 031901 (2012).

56 Jalem, R. *et al.* Concerted migration mechanism in the Li ion dynamics of garnet-type Li7La3Zr2O12. *Chem. Mater.* **25**, 425–430 (2013).

57 Meier, K., Laino, T. & Curioni, A. Solid-state electrolytes: revealing the mechanisms of Li-ion conduction in tetragonal and cubic LLZO by first-principles calculations. *J. Phys. Chem. C* **118**, 6668–6679 (2014).

58 Panchmatia, P. M. *et al.* Oxygen defects and novel transport mechanisms in apatite ionic conductors: combined 17O NMR and modeling studies. *Angew. Chem. Int. Ed.* **50**, 9328-9333 (2011).

59 Deng, Y. *et al.* Structural and mechanistic insights into fast lithium-ion conduction in Li4SiO4-Li3PO4 solid electrolytes. *J. Am. Chem. Soc.* **137**, 9136–9145 (2015).

60 Saxton, M. J. Single-particle tracking: the distribution of diffusion coefficients. *Biophys. J.* **72**, 1744–1753 (1997).

61 Berglund, A. J. Statistics of camera-based single-particle tracking. *Physical Review E* **82**, 011917 (2010).

62 Michalet, X. Mean square displacement analysis of single-particle trajectories with localization error: Brownian motion in an isotropic medium. *Physical Review E* **82**, 041914 (2010).

63 Michalet, X. & Berglund, A. J. Optimal diffusion coefficient estimation in single-particle tracking. *Physical Review E* **85**, 061916 (2012).

64 Chitra, R. & Yashonath, S. Estimation of error in the diffusion coefficient from molecular dynamics simulations. *The Journal of Physical Chemistry B* **101**, 5437–5445 (1997).

65 Leetmaa, M. & Skorodumova, N. V. Mean square displacements with error estimates from non-equidistant time-step kinetic Monte Carlo simulations. *Comput. Phys. Commun.* **191**, 119–124 (2015).

66 Catti, M. Short-range order and Li+ ion diffusion mechanisms in Li5La9□2(TiO3)16 (LLTO). *Solid State Ionics* **183**, 1 – 6 (2011).

67 Lang, B., Ziebarth, B. & Elsässer, C. Lithium Ion Conduction in LiTi2(PO4)3and Related Compounds Based on the NASICON Structure: A First-Principles Study. *Chem. Mater.* **27**, 5040-5048 (2015).

68 Burbano, M., Carlier, D., Boucher, F., Morgan, B. J. & Salanne, M. Sparse cyclic excitations explain the low ionic conductivity of stoichiometric Li7La3Zr2O12. *Phys. Rev. Lett.* **116**, 135901 (2016).

69 Uebing, C. & Gomer, R. Determination of surface diffusion coefficients by Monte Carlo methods: Comparison of fluctuation and Kubo–Green methods. *J. Chem. Phys.* **100**, 7759-7766 (1994).

70 Van der Ven, A., Ceder, G., Asta, M. & Tepesch, P. First-principles theory of ionic diffusion with nondilute carriers. *Phys. Rev. B.* **64**, 184307 (2001).

71 Murch, G. E. The Haven ratio in fast ionic conductors. *Solid State Ionics* **7**, 177-198 (1982).

72 Arbi, K., Mandal, S., Rojo, J. & Sanz, J. Dependence of ionic conductivity on composition of fast ionic conductors Li1+xTi2-xAlx(PO4)3, 0⩽ x⩽ 0.7. a parallel NMR and electric impedance study. *Chem. Mater.* **14**, 1091–1097 (2002).

73 Kosova, N., Devyatkina, E., Stepanov, A. & Buzlukov, A. Lithium conductivity and lithium diffusion in NASICON-type Li1+ xTi2–xAlx (PO4) 3 (x= 0; 0.3) prepared by mechanical activation. *Ionics* **14**, 303-311 (2008).

74 Huang, R. *et al.* Direct observation of the full transition from ballistic to diffusive Brownian motion in a liquid. *Nat. Phys.* **7**, 576–580 (2011).

75 Ruppert, D. & Wand, M. P. Multivariate locally weighted least squares regression. *The annals of statistics*, 1346-1370 (1994).

76 Li, Y. *et al.* Ionic distribution and conductivity in lithium garnet Li7La3Zr2O12. *J. Power Sources* **209**, 278–281 (2012).

77 Kresse, G. & Furthmuller, J. Efficient iterative schemes for ab initio total-energy calculations using a plane-wave basis set. *Phys. Rev. B.* **54**, 11169–11186 (1996).

78 Blöchl, P. E. Projector augmented-wave method. *Phys. Rev. B.* **50**, 17953-17979, doi:10.1103/PhysRevB.50.17953 (1994).

79 Perdew, J. P., Ernzerhof, M. & Burke, K. Rationale for mixing exact exchange with density functional approximations. *J. Chem. Phys.* **105**, 9982–9985 (1996).

80 Jain, A. *et al.* Commentary: the materials project: a materials genome approach to accelerating materials innovation. *Apl Mater.* **1**, 011002 (2013).

81 Jain, A. *et al.* A high-throughput infrastructure for density functional theory calculations. *Comput. Mater. Sci.* **50**, 2295–2310 (2011).

82 Jain, A. *et al.* Formation enthalpies by mixing GGA and GGA+U calculations. *Phys. Rev. B.* **84**, 045115 (2011).

83 Jones, G. & Thomas, P. Investigation of the structure and phase transitions in the novel A-site substituted distorted perovskite compound Na0. 5Bi0. 5TiO3. *Acta Crystallogr. Sect. B: Struct. Sci.* **58**, 168-178 (2002).

84 Ong, S. P. *et al.* Python Materials Genomics (pymatgen): A robust, open-source python library for materials analysis. *Comput. Mater. Sci.* **68**, 314-319, doi:10.1016/j.commatsci.2012.10.028 (2013).

85 Ong, S. P., Wang, L., Kang, B. & Ceder, G. Li-Fe-P-O2 Phase Diagram from First Principles Calculations. *Chem. Mater.* **20**, 1798-1807 (2008).

86 Mo, Y., Ong, S. P. & Ceder, G. First principles study of the Li10GeP2S12 lithium super ionic conductor material. *Chem. Mater.* **24**, 15-17 (2011).

87 Ong, S. P. *et al.* Phase stability, electrochemical stability and ionic conductivity of the Li 10±1 MP 2 X 12 (M= Ge, Si, Sn, Al or P, and X= O, S or Se) family of superionic conductors. *Energy Environ. Sci.* **6**, 148-156 (2013).

88 Ong, S. P., Jain, A., Hautier, G., Kang, B. & Ceder, G. Thermal stabilities of delithiated olivine MPO< sub> 4</sub>(M= Fe, Mn) cathodes investigated using first principles calculations. *Electrochem. Commun.* **12**, 427-430 (2010).

89 Ong, S. P., Wang, L., Kang, B. & Ceder, G. Li− Fe− P− O2 phase diagram from first principles calculations. *Chem. Mater.* **20**, 1798-1807 (2008).

90 Wang, L., Maxisch, T. & Ceder, G. Oxidation energies of transition metal oxides within the GGA+ U framework. *Phys. Rev. B.* **73**, 195107 (2006).

91 Chase, M. W. *NIST-JANAF thermochemical tables*. (American Chemical Society ; American Institute of Physics for the National Institute of Standards and Technology: Washington, DC, 1998).

92 Hautier, G., Fischer, C., Ehrlacher, V., Jain, A. & Ceder, G. Data mined ionic substitutions for the discovery of new compounds. *lnorg. Chem.* **50**, 656-663 (2010).

93 Burton, B. & Cockayne, E. Prediction of the [Na1/2Bi1/2] TiO3 ground state. *AIP Conf. Proc.* **582**, 82-90 (2001).

94 Levin, I. & Reaney, I. M. Nano ‐ and Mesoscale Structure of Na $ _ {1\ over 2} $ Bi $ _ {1\ over 2} $ TiO3: A TEM Perspective. *Adv. Funct. Mater.* **22**, 3445-3452 (2012).

95 Bousquet, M. *et al.* Optical properties of an epitaxial Na0. 5Bi0. 5TiO3 thin film grown by laser ablation: Experimental approach and density functional theory calculations. *J. Appl. Phys.* **107**, 104107 (2010).

96 Yashima, M., Itoh, M., Inaguma, Y. & Morii, Y. Crystal structure and diffusion path in the fast lithium-ion conductor La0. 62Li0. 16TiO3. *J. Am. Chem. Soc.* **127**, 3491-3495 (2005).

97 Yashima, M. & Tsuji, T. Structural investigation of the cubic perovskite-type doped lanthanum cobaltite La0. 6Sr0. 4CoO3-at 1531 K: possible diffusion path of oxygen ions in an electrode material. *J. Appl. Crystallogr.* **40**, 1166-1168 (2007).

98 Yashima, M. & Kamioka, T. Neutron diffraction study of the perovskite-type lanthanum cobaltite La 0.6 Sr 0.4 Co 0.8 Fe 0.2 O 3− δ at 1260 C and 394 C. *Solid State Ionics* **178**, 1939-1943 (2008).

99 Islam, M. S. Ionic transport in ABO3 perovskite oxides: a computer modelling tour. *J. Mater. Chem.* **10**, 1027-1038 (2000).

100 Mayeshiba, T. & Morgan, D. Strain effects on oxygen migration in perovskites. *Phys. Chem. Chem. Phys.* **17**, 2715-2721, doi:10.1039/c4cp05554c (2015).

101 Aidhy, D. S., Sinnott, S. B., Wachsman, E. D. & Phillpot, S. R. Effect of ionic polarizability on oxygen diffusion in δ-Bi2O3 from atomistic simulation. *Ionics* **16**, 297-303 (2010).

102 Chou, C.-S., Wu, C.-Y., Yang, R.-Y. & Ho, C.-Y. Preparation and characterization of the bismuth sodium titanate (Na0.5Bi0.5TiO3) ceramic doped with ZnO. *Adv. Powder Technol.* **23**, 358-365, doi:10.1016/j.apt.2011.04.015 (2012).

103 Yang, C. H. *et al.* Reduced leakage current, enhanced ferroelectric and dielectric properties in (Ce,Fe)-codoped Na0.5Bi0.5TiO3 film. *Appl. Phys. Lett.* **100**, 022909, doi:10.1063/1.3676663 (2012).

104 Kreisel, J. *et al.* An x-ray diffraction and Raman spectroscopy investigation of A-site substituted perovskite compounds: the (Na1-xKx)0.5Bi0.5TiO3 (0<=x<=1) solid solution. *J. Phys.: Condens. Matter* **12**, 3267-3280 (2000).

105 Elkechai, O., Manier, M. & Mercurio, J. P. Na0.5Bi0.5TiO3-K0.5Bi0.5TiO3 (NBT-KBT) System: A Structural and Electrical Study. *Phys. Status Solidi* **157**, 499-506 (1996).

106 Zhao, S., Li, G., Ding, A., Wang, T. & Yin, Q. Ferroelectric and piezoelectric properties of (Na, K)0.5Bi0.5TiO3 lead free ceramics. *J. Phys. D: Appl. Phys.* **39**, 2277-2281, doi:10.1088/0022-3727/39/10/042 (2006).

107 Norby, T. Fast oxygen ion conductors—from doped to ordered systems. *J. Mater. Chem.* **11**, 11-18, doi:10.1039/b003463k (2001).

108 Van Hove, L. Correlations in space and time and born approximation scattering in systems of interacting particles. *Phys. Rev.* **95**, 249 (1954).

109 Compaan, K. & Haven, Y. Correlation factors for diffusion in solids. *Trans. Faraday Society* **52**, 786–801 (1956).

110 *Inorganic Crystal Structure Database*, <http://icsd.fiz-karlsruhe.de/icsd> (FIZ Karlsruhe, 2016).

111 Mo, Y., Ong, S. P. & Ceder, G. First Principles study of the Li10GeP2S12 lithium super ionic conductor material. *Chem. Mater.* **24**, 15–17 (2012).

112 Dumon, A., Huang, M., Shen, Y. & Nan, C.-W. High Li ion conductivity in strontium doped Li7La3Zr2O12 garnet. *Solid State Ionics* **243**, 36–41 (2013).

113 Arbi, K. *et al.* Lithium mobility in Li1.2Ti1.8T0.2(PO4)3 compounds (R=Al, Ga, Sc, In) as followed by NMR and impedance spectroscopy. *Chem. Mater.* **16**, 255–262 (2004).

114 Donati, C. *et al.* Stringlike cooperative motion in a supercooled liquid. *Phys. Rev. Lett.* **80**, 2338–2341 (1998).

115 Keys, A. S., Hedges, L. O., Garrahan, J. P., Glotzer, S. C. & Chandler, D. Excitations are localized and relaxation is hierarchical in glass-forming liquids. *Phys. Rev. X* **1**, 021013 (2011).

116 Emly, A., Kioupakis, E. & Van der Ven, A. Phase stability and transport mechanisms in antiperovskite Li3OCl and Li3OBr superionic conductors. *Chem. Mater.* **25**, 4663–4670 (2013).

117 Du, Y. A. & Holzwarth, N. Li ion diffusion mechanisms in the crystalline electrolyte γ-Li3PO4. *J. Electrochem. Soc.* **154**, A999–A1004 (2007).

118 Morgan, B. J. & Madden, P. A. Relationships between atomic diffusion mechanisms and ensemble transport coefficients in crystalline polymorphs. *Phys. Rev. Lett.* **112**, 145901 (2014).

119 Kendrick, E., Kendrick, J., Knight, K. S., Islam, M. S. & Slater, P. R. Cooperative mechanisms of fast-ion conduction in gallium-based oxides with tetrahedral moieties. *Nat Mater* **6**, 871–875 (2007).

120 Nose, S. Constant temperature molecular dynamics methods. *Prog. Theor. Phys. Suppl.* **103**, 1–46 (1991).

121 He, X., Zhu, Y., Epstein, A. & Mo, Y. Statistical variances of diffusional properties from ab initio molecular dynamics simulations. *npj Computational Materials* **4**, doi:10.1038/s41524-018-0074-y (2018).

122 Willems, T. F., Rycroft, C. H., Kazi, M., Meza, J. C. & Haranczyk, M. Algorithms and tools for high-throughput geometry-based analysis of crystalline porous materials. *Microporous Mesoporous Mater.* **149**, 134-141, doi:10.1016/j.micromeso.2011.08.020 (2012).

123 Martin, R. L., Smit, B. & Haranczyk, M. Addressing challenges of identifying geometrically diverse sets of crystalline porous materials. *J. Chem. Inf. Model.* **52**, 308-318, doi:10.1021/ci200386x (2012).

124 Shannon, R. D. Revised effective ionic radii and systematic studies of interatomic distances in halides and chalcogenides. *Acta crystallographica section A: crystal physics, diffraction, theoretical and general crystallography* **32**, 751-767 (1976).

125 Zhu, Z., Chu, I.-H. & Ong, S. P. Li3Y(PS4)2 and Li5PS4Cl2: New Lithium Superionic Conductors Predicted from Silver Thiophosphates using Efficiently Tiered Ab Initio Molecular Dynamics Simulations. *Chem. Mater.* **29**, 2474-2484, doi:10.1021/acs.chemmater.6b04049 (2017).

126 Monchak, M. *et al.* Lithium Diffusion Pathway in Li1.3Al0.3Ti1.7(PO4)3 (LATP) Superionic Conductor. *lnorg. Chem.* **55**, 2941-2945, doi:10.1021/acs.inorgchem.5b02821 (2016).

127 Kuhn, A., Kohler, J. & Lotsch, B. V. Single-crystal X-ray structure analysis of the superionic conductor Li10GeP2S12. *Phys. Chem. Chem. Phys.* **15**, 11620-11622, doi:10.1039/c3cp51985f (2013).

128 Weber, D. A. *et al.* Structural Insights and 3D Diffusion Pathways within the Lithium Superionic Conductor Li10GeP2S12. *Chem. Mater.* **28**, 5905-5915, doi:10.1021/acs.chemmater.6b02424 (2016).

129 Suzuki, T. *et al.* Structure refinement of lithium ion conductors Li3Sc2 (PO4) 3 and Li3− 2x (Sc1− xMx) 2 (PO4) 3 (M= Ti, Zr) with x= 0.10 by neutron diffraction. *Solid State Ionics* **113**, 89-96 (1998).